DEVELOPMENT OF A SPECTRUM ANALYZER USING A SPIN TORQUE NANO-OSCILLATOR

DISSERTATION FOR THE DEGREE OF
DOCTOR OF PHILOSOPHY IN ELECTRICAL AND COMPUTER ENGINEERING

STEVEN LOUIS

OAKLAND UNIVERSITY

2020

DEVELOPMENT OF A SPECTRUM ANALYZER USING A SPIN TORQUE NANO-OSCILLATOR

by

STEVEN LOUIS

A dissertation submitted in partial fulfillment of the requirements for the degree of

DOCTOR OF PHILOSOPHY IN ELECTRICAL AND COMPUTER ENGINEERING

2020

Oakland University
Rochester, Michigan

Doctoral Advisory Committee:

Jia Li, Ph.D., Chair
Vasyl Tyberkevych, Ph.D.
Daniel Aloi, Ph.D.
Xia Wang, Ph.D.

© by Steven Louis, 2020
All rights reserved

To Raymond and Yan,

No words could properly convey my appreciation for the love, care, inspiration, and motivation you have given me.

ACKNOWLEDGMENTS

The author wishes to express his appreciation for extensive mentorship provided by Vasyl Tyberkevych, Andrei Slavin, Jia Li, and Thomas Meitzler. Thanks are also due to committee members Daniel Aloi, and Xia Wang for their contributions to this dissertation. Likewise, acknowledgment should be extended to the numerous post-docs, graduate students, and others who have engaged in discussions, dining, diversion, and discourse that have made this work possible.

A special note of acknowledgment should be extended to Artem Litvinenko and the research group of Ursula Ebels at CEA-SPINTEC, who showed experimentally that STNO spectrum analysis is a viable technology, and to Alex Jenkins and Ricardo Ferreira from International Iberian Nanotechnology Laboratory who fabricated the STNOs for this experiment.

This work was generously supported by funding from the Oakland University Research Office, by the National Science Foundation, and by the China Science and Technology Exchange Center.

Steven Louis

ABSTRACT

DEVELOPMENT OF A SPECTRUM ANALYZER USING A SPIN TORQUE NANO-OSCILLATOR

by

Steven Louis

Adviser: Jia Li, Ph.D.

Spectrum analyzers are critically important tools with applications in engineering, science, and medicine. Despite substantial technological improvements, current real time spectrum analyzers for demanding applications, such as pulsed radar signal analysis, cognitive radio, and analysis of frequency hopping signals, are exceedingly complex and/or computationally expensive. This dissertation proposes to overcome these challenges by using a rapidly tuned spin torque nano-oscillator (STNO) to perform fast, broadband spectrum analysis.

STNOs are suitable for spectrum analysis for several reasons. They are nano-sized low power auto-oscillators whose microwave frequency can be easily tuned by a bias DC current. They have a small time constant due to a small intrinsic capacitance and a small intrinsic inductance, and thus can be tuned very rapidly. STNOs have typical cross sectional area between 100 and 800 nm^2, can have a tunable bandwidth as high as 10 GHz, an operation frequency from about 100 MHz to above 65 GHz, and a linear scan rate that can be over 2 GHz/ns [1, 2, 3, 4, 5]. Taken together, the characteristics of small size, high tuning speed, and high frequency, STNO based spectrum analyzers have the potential to transform spectrum analyzer technology.

By using an STNO, spectrum analysis can be performed with scanning rates and scanning bandwidths that are on par with the current state of the art, all while remaining

sensitive to signals with power levels as low as the Johnson-Nyquist thermal noise floor. Specifically, this dissertation aims to show that with an STNO, spectrum analysis can be performed with a bandwidth as high as 10 GHz, a scan rate fast as 5 GHz/ns, and a maximum frequency that can exceed 65 GHz.

Additionally, this dissertation aims to shows that it is possible to perform spectrum analysis on signals with frequencies between 100 GHz and 2 THz with a spintronic device called an antiferromagnetic tunnel junction (ATJ), with a scan rate faster than 10^5 GHz/ns. As ATJs are also nano-sized, low power, and easily tunable elements, they have the potential to revolutionize electronics in the THz gap.

This work is primarily theoretical, showing by theory and numerical simulation, that STNOs and ATJs can perform spectrum analysis quickly on low power signals with both high fidelity and high frequency resolution. Additionally, the validity of this work has been confirmed in collaboration with experimental scientists. Results of these experiments are presented in this dissertation.

We believe that a STNO based wide-band fast spectrum analyzer will find numerous applications in microwave signal processing, telecommunications, and novel logic devices. In particular, we suggest that it can be useful for several specific applications, including cognitive radio, analysis of frequency hopping signals, and determination of pulsed radar frequencies.

TABLE OF CONTENTS

LIST OF TABLES

LIST OF FIGURES

LIST OF ABBREVIATIONS

ADC	Analog to digital converter
ATJ	Antiferromagnetic tunnel junction
CMOS	Complementary metal-oxide-semiconductor
DR	Dynamic range
FFT	Fast Fourier transform
FWHM	Full width at half maximum
GMR	Giant magnetoresistance
JN	Johnson-Nyquist
LLGS	Landau-Lifshitz-Gilbert-Slonczewski
MDS	Minimum detectable signal
MTJ	Magnetic tunnel junction
RBW	Resolution bandwidth
SNR	Signal-to-noise ratio
STNO	Spin torque nano-oscillator
STT	Spin transfer torque
TF	Terahertz frequency
TMR	Tunneling magnetoresistance
VBW	Video bandwidth

CHAPTER ONE

INTRODUCTION

1.1 Motivation

Issac Newton published his seminal work, *Optiks*, in 1704[6]. His work analyzed the fundamental nature of light. Of the many experiments included in his tome, one illustrates the concept of spectrum analysis quite well. A diagram of the experiment, reprinted here, and is shown in Figure 1.1(a). In this experiment, white sunlight is passed through a prism, which separates sunlight into its component colors. The component colors, similar to a rainbow, can then be seen on a sheet of paper. The sheet of paper showed the spectrum of visible light present in sunlight. Together, the prism and sheet of paper in Newton's experiment can be viewed as a rudimentary spectrum analyzer.

Modern spectrum analyzers, that are significantly more complex than a sheet of paper, have allowed light to be analyzed with more precision. In a few words, the purpose of spectrum analysis is to determine what frequencies are present in a signal, and at what power. For example, the spectrum of visible sunlight on a clear day at sea level is shown in Figure 1.1(b) [7]. In this figure, the frequency of light is shown on the x axis, and the normalized spectral power of the sunlight is shown on y axis. In this figure, three colors have been labeled: red, green, and violet. Each color is associated with a particular set of frequencies. Red, for example, is associated with frequencies that range from 430 to 480 THz. Likewise, green is associated with the frequencies from 540 to 580 THz. The power of each color can be compared; it is evident that for sunlight, violet has a power that is lower than green or red.

In principle, spectrum analysis can be performed on any signal, whether transmitted by light, sound, electricity, or something else. Broadly speaking, spectrum

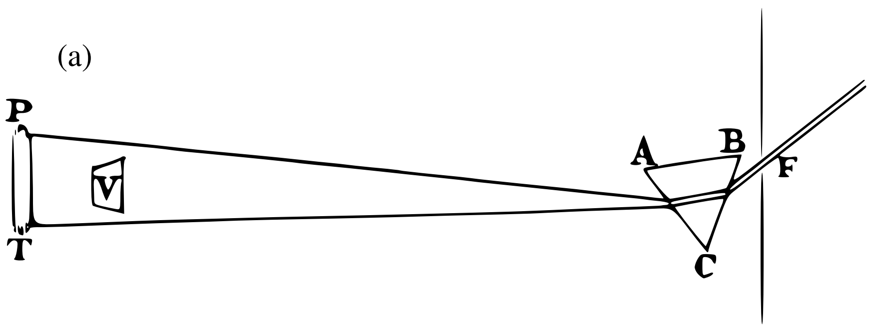

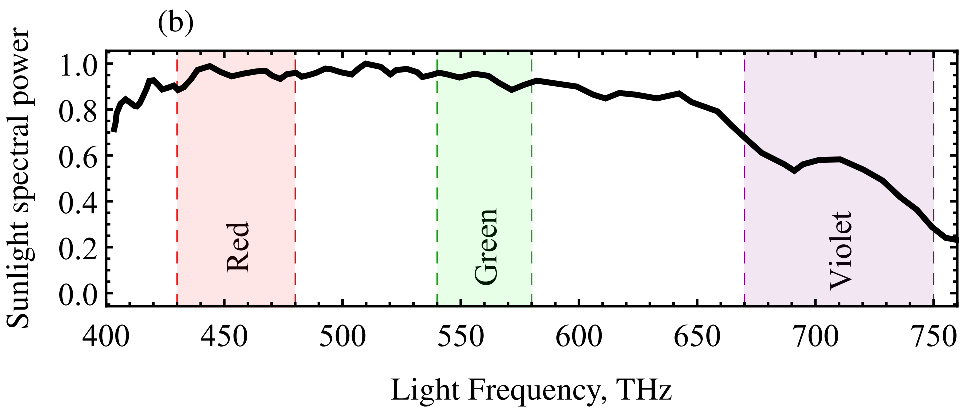

Figure 1.1: Newton and the spectrum of sunlight. (a) A figure from Newton's *Optiks*[6]. In this figure, sunlight enters through a small round hole F, then passes through a prism ABC onto a wall PT. A white piece of paper V was held to intercept a part of the spectrum. Newton viewed the spectrum of sunlight on this paper. (b) The spectrum of direct sunlight at sea level [7]. Red, green, and violet are present in the frequency bands as labeled. The spectral power of each frequency can be determined from the y axis.

analysis measures the magnitude of different frequency components present in a signal. A major challenge is to perform spectrum analysis quickly with high precision over a wide bandwidth. For example, it is common for pulsed radar to transmit signals with pulses that are 50 ns in duration or less. Analyzing a signal with a 50 ns duration over a wide bandwidth with high precision, at present, possible only with bulky, technically complex, and expensive equipment. There are other applications, including facilitating cognitive radio and adaptive frequency hopping protocols, that would benefit from a miniaturized, low cost spectrum analyzer. One aim of this dissertation is to develop theory that will facilitate the development of new technology that will overcome this shortcoming.

A critical measure of the speed of spectrum analysis depends on the spectrum analyzer *scan rate*. This is a measure of how quickly a frequency bandwidth can be analyzed. A spectrum analyzer with a fast scan rate requires a signal generator that can be tuned quickly through a specified frequency bandwidth. Current signal generator technologies cannot be tuned over a wide bandwidth with a scan rate fast enough to enable nanosecond timescale spectrum analysis.

Thus, there is a need for a new technology that is not only capable of analyzing signals with a nanosecond timescale, but also one that is compact, simple, and affordable. It will be shown in this dissertation that by using a Spin Torque Nano Oscillator (STNO) and an appropriate algorithm, that it is possible to create a technically simple, nanoscale system with performance characteristics approaching theoretical limits. This dissertation presents theory of a spectrum analyzer based on an STNO.

The primary findings of the dissertation are as follows. We have found, both theoretically and experimentally, that STNOs are capable of faithfully performing spectrum analysis on a complicated, multi-tone signal. Two spectrum analysis regimes were investigated, an *injection locking* regime and a *mixing* regime. The injection locking regime, which uses a novel spectrum analysis algorithm, can perform spectrum analysis with a scan rate that is limited only by the speed at which the STNO can injection lock to the external signal. The mixing regime can perform spectrum analysis that is substantially faster than the injection locking regime, with a frequency resolution that is near the theoretical limit, while remaining sensitive to signal powers below the Johnson-Nyquist thermal noise floor. Experiments performed by collaborators have confirmed the utility of using an STNO for spectrum analysis. We also provide a theory for performing spectrum analysis at frequencies between 0.1 and 2 THz with a spintronic device called an Antiferromagnetic Tunnel Junction (ATJ).

Much of the work in this dissertation has already been presented in three peer reviewed journal articles[8, 9, 10] and at several conferences[5, 11, 12, 13, 14, 15, 16, 17]. In addition, there is one manuscript that has recently been submitted for review[18].

1.2 Potential applications for fast spectrum analysis

It is worthwhile to introduce several possible applications for a fast spectrum analyzer based on a STNO. Here we present brief outlines of three topics (cognitive radio, frequency hopping, and pulsed radar frequency determination) where fast spectrum analysis may be beneficial. Of course, there are many applications that can benefit from a nanoscale, fast wide-band spectrum analyzer, including applications that cannot at present be envisioned.

1.2.1 Cognitive radio

Radio transmissions are a familiar part of modern life. Several examples include listening to FM radio, watching broadcast television, or using a mobile phone. To facilitate communication and prevent interference, governmental organizations strictly regulate radio signal transmissions. For example, in the United States, the Federal Communications Commission (FCC) sells licenses for different portions of the radio spectrum. At a recent auction, the FCC raised ∼\$19.8 billion from licensing parts of the electromagnetic spectrum[19]. In a few words, radio spectrum is a precious resource that is expensive. Likewise, because it is useful, possessing the license to use a part of the spectrum can be quite profitable.

In many applications, a portion of the spectrum allocated by the FCC can go unused at any given time. For example, a channel in a cellular network may go unused during off-peak hours. For applications that only use allocated spectrum at certain times, it is possible to generate revenue by subleasing the spectrum to other users. These secondary parties can use a relatively new technology called cognitive radio[20]. Cognitive radio uses dynamic spectrum management to allow secondary users to transmit at times when spectrum is unused by primary users, and remain idle when spectrum is in use by primary users. One proposed method for dynamic spectrum management is to use fast spectrum analysis to monitor the spectrum, and respond to detected usage[20].

With this method of dynamic spectrum management, the spectrum in question must be analyzed rapidly to determine bandwidth availability. Ideally, a spectrum analyzer for dynamic spectrum management would be fast enough to determine bandwidth availability and respond to changes in usage, while being integrated with other electronics, and operate with a low power consumption and a wide scanning bandwidth. One step in achieving this may be to integrate a miniaturized STNO based spectrum analyzer with cognitive radio circuitry.

1.2.2 Frequency hopping

Bluetooth is a well-known example of a technology that uses a *frequency hopping* transmission protocol. A frequency hopping protocol is a radio transmission protocol where the carrier frequency of the signal changes with time. Two prominent advantages to frequency hopping protocols include resistance to narrowband interference and improved transmission security. Bluetooth operates between 2.4 GHz and 2.8835 GHz, and hops between 79 different channels, with a hop every 625 μs[21]. Another recently developed protocol operates even faster, with a hop every 1 μs[22]. There is a prospect to develop even faster frequency hopping algorithms.

Fast spectrum analysis, if readily available, would greatly aid in the design of new frequency hopping protocols. It could also be used to decode signals encrypted with frequency hopping. Even more, in principle fast spectrum analysis could be integrated with adaptive frequency hopping protocols, which transmit with only unused channels to prevent interference.

1.2.3 Pulsed radar analysis

Another application of fast spectrum analysis is the analysis of short pulse length radar signals. Radar operates by transmitting an electromagnetic pulse that travels to a target of interest, bounces off a target and returns to the radar. The amount of time between transmission and reception is then measured, which allows the distance between the radar and the target to be calculated. Speed and trajectory can also be determined by radar.

When pulsed radar systems use shorter pulses, they can provide more accurate information about target range and velocity information[23, 24]. They also allow for improved discrimination between two closely spaced targets[23]. Why shorter pulses allow for improved discrimination over longer pulses can be understood as follows. Consider two pulses; one that has a duration of 500 ns and another with a duration of 50 ns. A pulse that is 500 ns in duration will transmit a radio signal that has a physical length of 150 m. In contrast, at pulse that is 50 ns in duration will have a physical length of 15 m. The shorter pulse duration leads to a physically shorter radio signal, which can vastly improve radar resolution. This then allows more precise range, velocity, and object discrimination.

Radar systems are complex, and many factors impact their performance. However, it can be said that shorter pulses improve the quality of information that can be gathered by radar. The literature cites a 50 ns pulse as fairly common for marine pulsed radar systems[23]. One can assume that classified systems will have pulse lengths that are even shorter in duration.

For military applications, it could be critical to quickly detect and characterize a pulsed radar signal. A nano-scale fast spectrum analyzer with low power requirements would allow a pulse to be detected and analyzed quickly enough to activate jamming systems and associated anti-radar weapon systems. Considering that shorter pulses contain less power and hence are used for short range applications, short pulse length radar signals can indicate the close proximity of hostile forces. This means that the speed of detection and analysis is absolutely critical. We feel that STNOs, since they are small, radiation hard, and are relatively impervious to electronic warfare measures, are well suited for field deployment in military applications.

1.3 Organization of chapters

Chapter 2 provides a general background for topics relevant to this thesis. It begins with an introduction to spectrum analyzers and defines performance metrics relevant to spectrum analysis. After this, it provides a brief background about STNOs.

Chapter 3 is the methods chapter. It provides details about how STNO simulations and signal processing were performed in this dissertation.

Chapter 4 presents the theory of STNO injection locking spectrum analysis. It begins by presenting a theoretical description of STNO dynamic tuning. Then, it shows that an STNO spectrum analyzer can function with a novel algorithm that operates by injection locking to external microwave signals.

Chapter 5 presents STNO mixing spectrum analysis, theory and experiment. This method uses a rapidly tuned spin torque nano-oscillator (STNO), and does not require injection locking. It treats an STNO as an element with an oscillating *resistance*. It is found analytically and by numerical simulation that the proposed spectrum analyzer has a frequency resolution at the theoretical limit for frequency resolution, with a wide scanning bandwidth and fast scanning rate, all while remaining sensitive to signal power at the Johnson-Nyquist thermal noise floor. Chapter 5 also presents experimental results.

Chapter 6 presents the theory of THz mixing spectrum analysis with an Antiferromagnetic Tunnel Junction. It proposes to perform spectrum analysis on low power signals between 0.1 and 2 THz. This method of THz spectrum analysis, if realized in experiment, will allow miniaturized electronics to rapidly analyze low power THz signals with a simple algorithm.

CHAPTER TWO

BACKGROUND

This chapter provides the background information for spectrum analysis and STNOs. This dissertation is an interdisciplinary study, with elements of electrical engineering and applied condensed matter physics. Thus, it is prudent to introduce the internal functioning of spectrum analyzer equipment for physicists, and the basic operation of an STNOs for engineers. This chapter begins with an introduction to spectrum analyzers.

2.1 Spectrum analysis introduction

The purpose of this section is to introduce the basic idea of spectrum analysis, and to introduce performance metrics that will allow for evaluation of the proposed spectrum analyzer. Consider the photographic image of a commercially available spectrum analyzer screen shown in Figure 2.1. The inset shows a color photo of a spectrum analyzer, while the main figure shows the spectrum analysis screen. In this figure, the horizontal axis is scaled with frequency, and the vertical axis is scaled with the spectral power of the analyzed signal. Running from left to right is a curve which represents an analyzed external signal. This signal has two prominent peaks with a relative magnitude of ~ -50 dB, and a strong dip at the point labeled (d). At other frequencies, it has a relative magnitude of around -80 dB.

Also labeled in Figure 2.1 are several important metrics by which the quality of a STNO spectrum analyzer will be evaluated. They are as follows: scanning bandwidth, scan rate, frequency accuracy, resolution bandwidth, responsivity, minimum detectable signal, maximum input power, and dynamic range. These metrics will be covered in detail in this section, and they are summarized in Table 2.1.

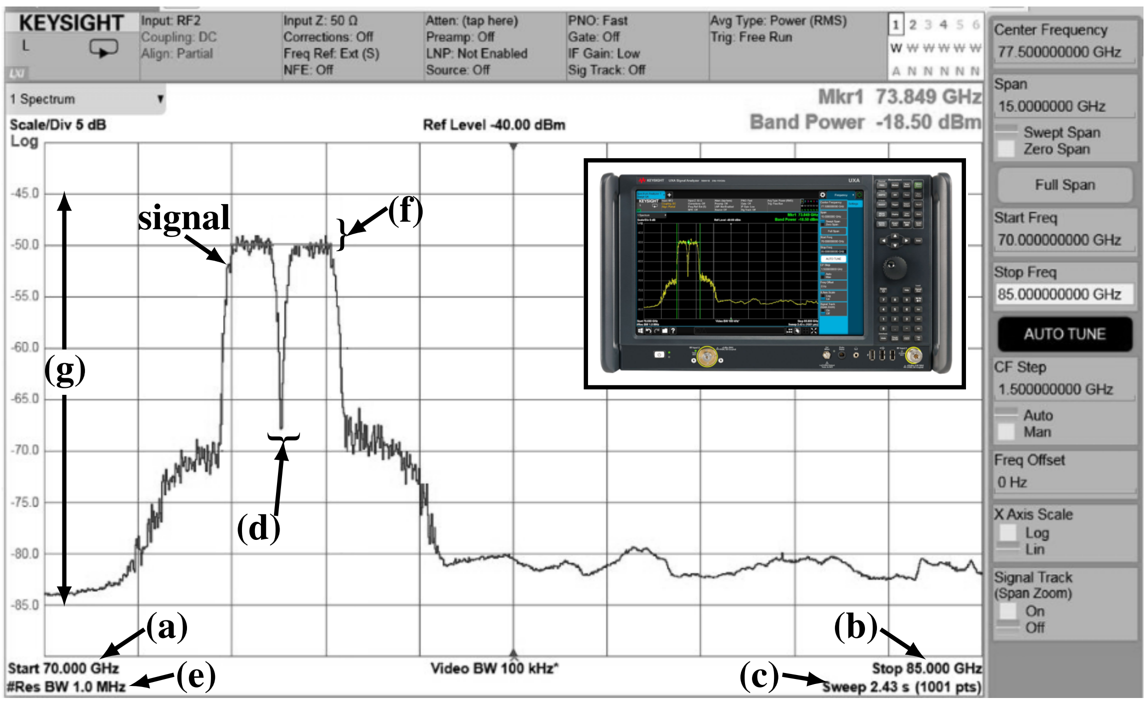

Figure 2.1: Image of a commercial spectrum analyzer. Inset shows the front panel of a Keysight Technologies UXA N9041B Signal Analyzer. Main figure shows inverted grayscale for clarity. (a),(b) scanning bandwidth, (c) sweep time (scan rate), (d) frequency accuracy, (e) resolution bandwidth, (f) responsivity, and (g) dynamic range. Image courtesy Keysight Technologies.

Scanning bandwidth

The total bandwidth over which spectrum analysis is performed is called the scanning bandwidth, which is represented by Δf_{ch}. For example, Figure 2.1(a) shows the scanning range beginning at 70 GHz and Figure 2.1(b) shows the scanning bandwidth ending at 85 GHz. Thus the total scanning bandwidth is given by $\Delta f_{\text{ch}} = 15$ GHz. Scanning bandwidth is measured with units of Hz.

Scan rate

The scan rate, denoted by ρ, is the rate at which spectrum analysis is performed. This can be defined as follows. As shown in Figure 2.1(c), this spectrum was acquired with a sweep time of $T = 2.43$ s. The scan rate is given by:

$$\rho = \frac{\Delta f_{\text{ch}}}{T}\,. \tag{2.1}$$

The scanning bandwidth was found, above, to be $\Delta f_{\text{ch}} = 15$ GHz. Thus for the spectrum analysis performed in Figure 2.1, the scan rate is $\rho \approx 6.2$ Hz/ns. Scan rate in this dissertation is measured in units of Hz/s.

Frequency accuracy

Frequency accuracy is a measure of how faithfully the spectrum analyzer detects the frequency of an external signal. This is shown by Figure 2.1(d). Frequency accuracy will be computed with the relative error, given by:

$$\text{Frequency accuracy} = 1 - \frac{|f_{\text{actual}} - f_{\text{detected}}|}{f_{\text{actual}}}\,, \tag{2.2}$$

where f_{detected} is the frequency identified by the spectrum analyzer, and f_{actual} is the actual input frequency. A signal with perfect fidelity would have an accuracy of 100%. Frequency accuracy in this dissertation is measured in as a percentage.

Table 2.1: Performance metrics for spectrum analysis

Performance Metric	**Symbol**	**Base Units**	**Brief Description**
Frequency accuracy		Hz	Accuracy with which the input signal frequency is identified.
Scanning bandwidth	Δf_{ch}	Hz	Total bandwidth to be analyzed.
Scan rate	ρ	Hz/s	The rate at which spectrum analysis is performed.
Resolution bandwidth	RBW	Hz	Total bandwidth to be is performed.
Responsivity	G	dB	Gain; output/input ratio.
Minimum detectable signal	P_{mds}	W	Power of smallest signal that can be detected.
Maxmium input power	P_{max}	W	Power of largest signal that can be detected.
Dynamic range	DR	dB	Range of inputs to which the spectrum analyzer is sensitive.

Resolution bandwidth

In a practical spectrum analyzer, the peaks of an identified signal will occupy a finite bandwidth. When two neighboring peaks are in close proximity, they will merge into a single peak. Resolution bandwidth (RBW), which is shown in shown in Figure 2.1(e), is the measure of the minimum separation required to distinguish two neighboring frequencies, with a low RBW preferred. RBW can also be called frequency resolution, and can be defined as equal to the bandwidth of each spike. There is more than one way to define RBW; the most intuitive definition is the full width at half maximum (FWHM) which is shown in Figure 2.6. RBW has units of Hz.

Responsivity

Responsivity, which is also known as sensitivity, is the gain of the system. It can be expressed as a ratio of output amplitude over input amplitude. It is denoted here by the symbol G, and is shown in Figure 2.1(f). The units of responsivity is the ratio the units used to express input and output, and in this dissertation will be V/A.

Minimum detectable signal

The smallest power an external signal can have, and still be detectable by the spectrum analyzer, is called the minimum detectable signal (MDS). Here it will be given by P_{mds}. MDS is not shown on the figure. The units of P_{mds} are Watts.

Maximum input power

The maximum input power, given by P_{max}, is the maximum power that can be accepted while allowing accurate signal frequency identification. Maximum input power is not shown on the figure. The units of P_{max} are given in Watts.

Dynamic range

Here, we define dynamic range (DR) as

$$\mathrm{DR} = \frac{P_{\mathrm{max}}}{P_{\mathrm{mds}}}. \tag{2.3}$$

DR is not shown in the figure, but it would represent the maximum possible extent of Figure 2.1(g), which shows a span from -40 dBm to -90 dBm, a span of 50 dB. DR in this thesis will be measured in dB.

2.2 Spectrum analyzer operation

In simple terms, the operation of a modern swept-tuned spectrum analyzer is as follows. A block diagram of a basic swept-tuned spectrum analyzer system is shown in Figure 2.2. Here, spectrum analysis occurs in two stages. In the figure, stage 1 is signal mixing and filtering, while stage 2 contains the application of a spectrum analysis algorithm and spectrum display. In this section, these two stages will be introduced in detail, along with signal and mathematical notation. This section will introduce the topic in sufficient detail to allow evaluation of STNO viability for spectrum analysis. For a more comprehensive and high quality overview of spectrum analyzer signal processing and operation, please see [25].

This discussion will be limited to swept-tuned spectrum analyzers, which predominate for wide bandwidth applications. In this section, the process of signal mixing and filtering is discussed first. After this, three basic spectrum analysis algorithms will be presented: envelope detection, pulse compression, and fast Fourier transform. Together, this will provide enough introduction to spectrum analysis to allow evaluation of the utility of STNOs for spectrum analysis.

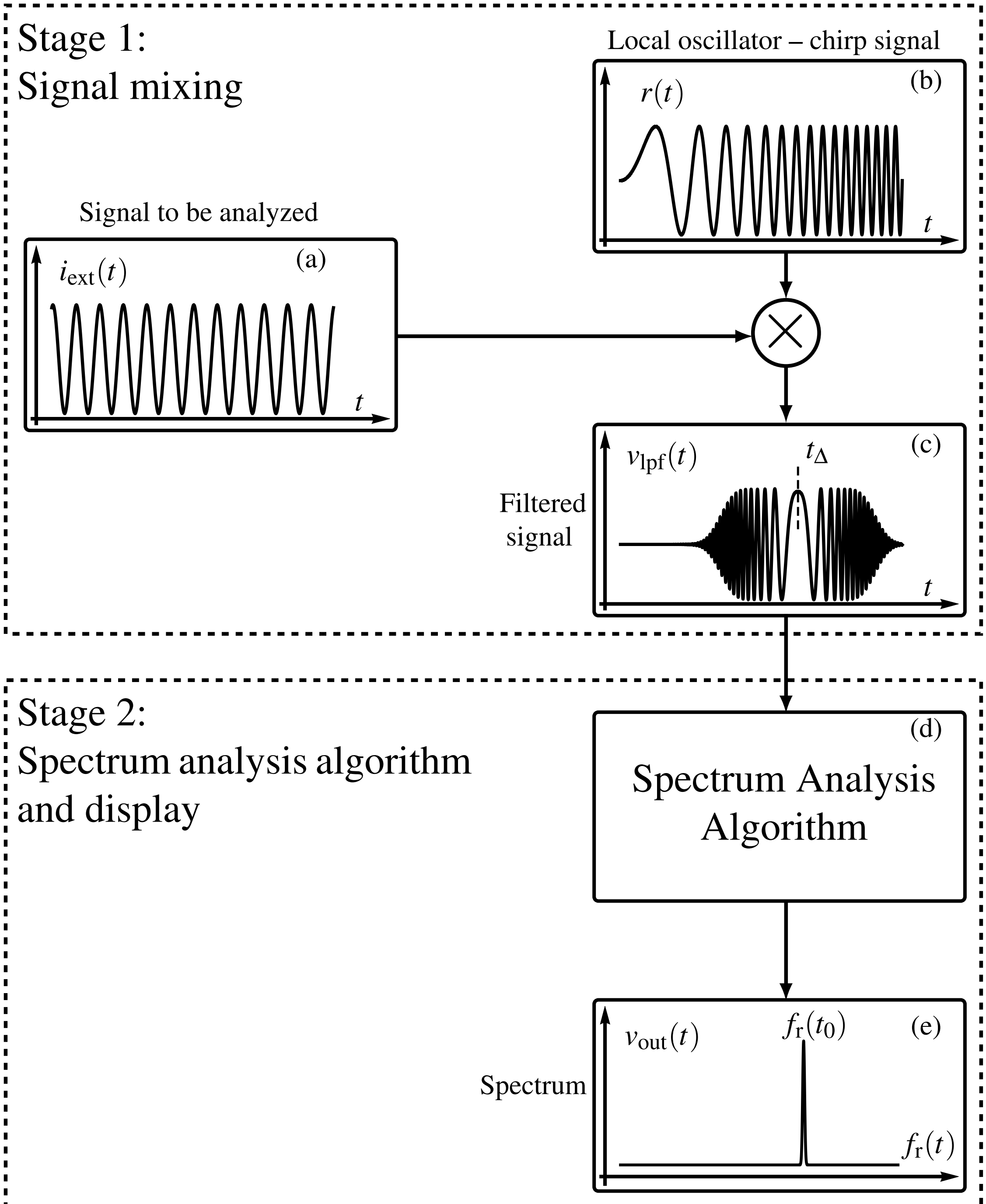

Figure 2.2: Spectrum analyzer block diagram. Spectrum analysis occurs in two stages, stage 1 is signal mixing, and stage 2 is the spectrum analysis algorithm and display of the spectrum. In detail, (a) $i_{\mathrm{ext}}(t)$, the external signal, which is to be analyzed, is mixed via multiplication with (b) $r(t)$ the locally generated swept-tuned signal. (c) $v_{\mathrm{lpf}}(t) = i_{\mathrm{ext}}(t)r(t)$ is the filtered signal. (d) The mixed signal is then processed with a spectrum analysis algorithm. (e) The spectrum $v_{\mathrm{out}}(t)$ is displayed as a function of frequency.

2.2.1 Signal mixing

Here we discuss a swept-tuned mixing protocol, which is shown by the block diagram in Figure 2.2. The method presented here is a simplified mixing arrangement. In actual commercial implementations, a more sophisticated method is used to increase scanning bandwidth. For more information, see the last page of [25].

External signal

An external signal to be analyzed, which here is a sinusoid with a single frequency, is depicted in Figure 2.2(a). The goal of spectrum analysis is to determine the magnitude of the frequencies present in this signal. For much of this dissertation, the spectrum of single tone signals will be analyzed. An external signal with a single tone can be expressed as:

$$i_{\text{ext}}(t) = A_{\text{ext}} \sin(\omega_{\text{ext}} t + \psi_{\text{ext}}) \,, \tag{2.4}$$

where $i_{\text{ext}}(t)$ is the external signal that is carried by an electric current, A_{ext} is the external signal amplitude, ω_{ext} is the angular frequency of the external signal, t is time, and ψ_{ext} is the initial phase of the external signal. Additionally, the linear frequency of the external signal is defined as $f_{\text{ext}} = \omega_{\text{ext}}/2\pi$.

Swept-tuned chirp signals

In most modern wide-band spectrum analyzers, spectrum analysis begins by mixing an external signal, which is the signal to be analyzed, with a signal generated by a local oscillator. This local oscillator generates a signal with frequency that is "swept-tuned", which means the signal frequency changes with time. A swept tuned signal is shown in Figure 2.2(b). In the diagram, the local oscillator starts with a low frequency, then increases to a high frequency at a rate that is linear with time. A swept-tuned signal, or a signal that changes frequency with time, is often called a chirp. A signal whose frequency changes linearly with time defined here as a *linear chirp*. The frequency of a linear chirp is given by:

$$f_{\mathrm{r}}(t) = \rho t + f_0 \,, \tag{2.5}$$

where ρ is the scan rate, and f_0 is the frequency at $t = 0$. Note that for $\rho > 0$, the frequency of the chirp is increasing, and for $\rho < 0$, the frequency of the chirp is decreasing. For simplicity, in this thesis ρ will always be positive. Also note that $\omega_{\mathrm{r}}(t) = 2\pi f_{\mathrm{r}}(t)$ and $\omega_0 = 2\pi f_0$.

Recalling that instantaneous frequency is the time derivative of phase, the phase of a linear chirp signal is found by integrating Equation (2.5) as:

$$\theta_r(t) = \int \omega_{\mathrm{r}}(t)dt = \pi\rho t^2 + \omega_0 t + \psi_{\mathrm{r}} \,, \tag{2.6}$$

where ψ_{r}, the constant of integration, and represents the initial phase of the chirped signal. This chirp signal can now be defined as:

$$r(t) = \begin{cases} A_{\mathrm{r}} \cos\left(\pi\rho t^2 + \omega_0 t + \psi_{\mathrm{r}}\right) & -\frac{T}{2} \le t \le \frac{T}{2} \\ 0 & \text{otherwise} \end{cases} \,, \tag{2.7}$$

where T is the period of the chirp. This is written as a piecewise function because the chirp will only sweep through a finite scanning bandwidth

$$\Delta f_{\mathrm{ch}} = \left| f_{\mathrm{r}}\left(-\tfrac{T}{2}\right) - f_{\mathrm{r}}\left(\tfrac{T}{2}\right) \right| = \rho T \,. \tag{2.8}$$

Swept-tuned chirp signals in this dissertation will be generated by spin torque nano-oscillators, which will be introduced in section 2.3. STNO generated signals are physically manifested as a time-varying resistance.

Signal multiplication and filtering

The next step in signal mixing is to multiply the swept tuned signal $r(t)$ by the signal to be analyzed $i_{\text{ext}}(t)$. When two cosine functions are multiplied together, they follow the identity

$$2\cos A\cos B = \cos(A-B) + \cos(A+B)\,. \tag{2.9}$$

Therefore, when the external signal and the locally generated chirp signal are mixed, the resultant signal will be:

$$i_{\text{ext}}(t)r(t) = \begin{cases} A\cos\Big(\pi\rho t^2 + (\omega_0 - \omega_{\text{ext}})t + \psi_{\text{r}} - \psi_{\text{ext}}\Big) & -\frac{T}{2} \leq t \leq \frac{T}{2} \\ +A\cos\Big(\pi\rho t^2 + (\omega_0 + \omega_{\text{ext}})t + \psi_{\text{r}} + \psi_{\text{ext}}\Big) & \\ & \\ 0 & \text{otherwise} \end{cases}, \tag{2.10}$$

where $A = A_{\text{r}}A_{\text{ext}}/2$. It is notable that because Equation (2.4) represents a current, and Equation (2.7) represents a resistance, that Equation (2.10) represents a voltage.

The first term in Equation (2.10) is the “frequency difference” signal, which has a low frequency. The second term is the “frequency sum” signal, which has a high frequency. A filter can be used to attenuate the entire frequency sum signal, while retaining the frequency difference signal. Filters are electronic elements that retain frequencies within a pass bandwidth, while attenuating frequencies outside the pass bandwidth [26]. Here we will use a low pass filter, called $h_{\text{lpf}}(t)$, which will retain all frequencies below a cutoff frequency of f_{c}. The filtered signal can be represented symbolically as

$$v_{\text{lpf}}(t) = [i_{\text{ext}}(t)r(t)] * h_{\text{lpf}}(t)\,, \tag{2.11}$$

where $*$ is the symbol for convolution. Substituting Equation (2.10) into Equation (2.11), and choosing an f_c such that the frequency sum signal is attenuated, yields

$$v_{\text{lpf}}(t) = \begin{cases} A\cos(\phi(\omega_{\text{ext}},t)+\psi) & -\frac{T}{2} \leq t \leq \frac{T}{2} \\ 0 & \text{otherwise} \end{cases} \tag{2.12}$$

with a time dependent phase that is given by

$$\phi(\omega_{\text{ext}},t) = \pi\rho t^2 - (\omega_{\text{ext}} - \omega_0)t\,. \tag{2.13}$$

In these equations, $\psi = \psi_{\text{r}} - \psi_{\text{ext}}$. The mixed and filtered signal is shown in Figure 2.2(c).

The frequency of v_{lpf} has a minimum at a certain time t_Δ, as shown in Figure 2.2(c). It is this low frequency interval that indicates the presence of an external signal. This occurs at a time when the frequency of the external signal and the linear chirp coincide, specifically, when $f_{\text{r}}(t_\Delta) = f_{\text{ext}}$. This time is given by

$$t_\Delta = \frac{f_{\text{ext}} - f_0}{\rho}\,. \tag{2.14}$$

Accurately determining t_Δ with high precision is the purpose of the spectrum analysis algorithm, which will be covered in the next section.

Please note that Equation (2.14) can be rewritten as $(\omega_{\text{ext}} - \omega_0) = 2\pi\rho t_\Delta$. With Equation (2.5), Equation (2.12) to be rewritten as:

$$v_{\text{lpf}}(t) = \begin{cases} A\cos\left(\pi\rho(t-t_\Delta)^2 + \psi_\Delta\right) & -\frac{T}{2} \leq t \leq \frac{T}{2} \\ 0 & \text{otherwise} \end{cases}\,, \tag{2.15}$$

where $\psi_\Delta = \psi - \pi\rho t_\Delta^2$. Thus, multiplying an external signal by a chirp results in a time-shifted chirp.

2.2.2 Spectrum analysis algorithms

The previous section reviewed Figure 2.2, stage 1. In this section, stage 2 will be covered. Here will will review important spectrum analysis algorithms, namely envelope detection, matched filtering, and fast Fourier transform.

Envelope detection

A simple, and commonly used, spectrum analysis algorithm is called envelope detection[25]. This is shown in Figure 2.3, which begins with example curve for $v_{\text{lpf}}(t)$, where $h_{\text{lpf}}(t)$ is a Gaussian filter, as depicted in Figure 2.3(a).

This spectrum analysis algorithm functions as follows. First, the absolute value of the signal, $\left|v_{\text{lpf}}(t)\right|$, is found. Then, the envelope of $\left|v_{\text{lpf}}(t)\right|$ is found an envelope detector. This is depicted in Figure 2.3(b). In this figure, $\left|v_{\text{lpf}}(t)\right|$ is represented by a thin black line, while its envelope is shown by a thick black line. The envelope, which we can call $v_{\text{out}}(t)$, is a function of time.

This function has a peak at time t_Δ. The time at which the envelope peaks corresponds with the presence of a signal at a particular frequency. To display the frequency, the time can be mapped to frequency by using Equation (2.5). This is depicted in Figure 2.3(c). In this case, for a peak that occurs at time t_Δ, the spectrum analyzer will indicate the presence of a frequency $f_{\text{r}}(t_\Delta)$.

Matched filter and pulse compression

A more sophisticated spectrum analysis algorithm is to use a matched filter to perform pulse compression. This is the primary algorithm that is used in this thesis. It functions by application of a matched filter to $v_{\text{lpf}}(t)$. This method was first reported in 1959, and it has since then been much considered [27, 28, 29, 30, 31, 32]. The algorithm

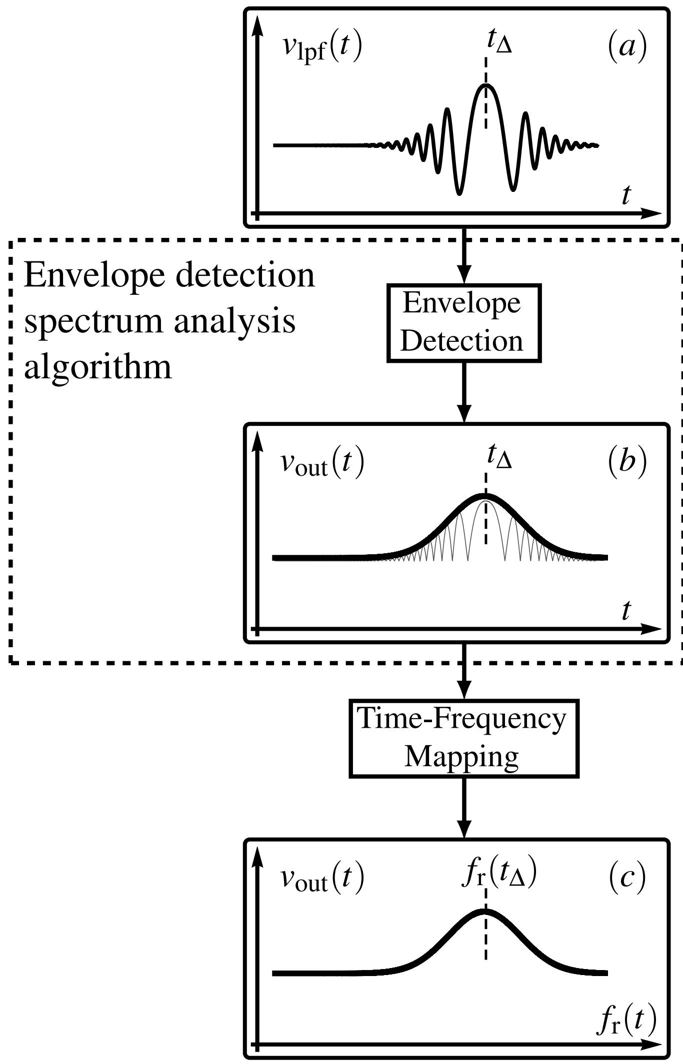

Figure 2.3: Spectrum analysis with envelope detection. (a) The mixed and filtered signal, $v_{\mathrm{lpf}}(t)$, is filtered with a Gaussian low pass filter. (b) The envelope of $\left|v_{\mathrm{lpf}}(t)\right|$ is detected, as shown by a solid black line. (c) The time axis is mapped to frequency, resulting in a frequency vs. magnitude plot.

to perform spectrum analysis with a matched filter is shown in Figure 2.4, which begins with example curve for $v_{\mathrm{lpf}}(t)$, where $h_{\mathrm{lpf}}(t)$ has a flat passband, as depicted in Figure 2.4(a).

The signal is then processed with a matched filter, $h_{\mathrm{match}}(t)$, as:

$$v_{\mathrm{out}}(t) = |v_{\mathrm{lpf}}(t) * h_{\mathrm{match}}(t)|^2 . \tag{2.16}$$

The matched filter performs a process known as pulse compression, where a very sharp peak at time t_Δ is formed as a result of the matched filter. This is shown in Figure 2.4(b)

In order to determine the frequency of the external signal, the time axis can be mapped to frequency by using Equation (2.5), as described in the previous subsection.

Because this is the primary algorithm used in this thesis, the mathematics of pulse compression should be considered in detail. The matched filter will have the form $h_{\mathrm{match}}(t) \rightarrow h_{\mathrm{match}}(\omega_{\mathrm{m}}, t)$, where $f_{\mathrm{m}} = \omega_{\mathrm{m}}/2\pi$ is an arbitrary frequency in Δf_{ch}. It is written as:

$$h_{\mathrm{match}}(\omega_{\mathrm{m}}, t) = e^{-j\phi(\omega_{\mathrm{m}}, t)} , \tag{2.17}$$

where $\phi(\omega_{\mathrm{m}}, t)$ was defined in Equation (2.13), and $j = \sqrt{-1}$. Performing the convolution from Equation (2.16) in appendix A, the square of the spectrum signal is given by:

$$v_{\mathrm{out}}(t) = \mathrm{sinc}^2\Big(\pi \Delta f_{\mathrm{ch}}(t - t_\Delta)\Big) + \varepsilon(\psi)\frac{\sqrt{2\rho}}{2\Delta f_{\mathrm{ch}}}\mathrm{sinc}\Big(\pi \Delta f_{\mathrm{ch}}(t - t_\Delta)\Big) + \frac{\rho}{2\Delta f_{\mathrm{ch}}^2} , \tag{2.18}$$

where sinc(x) is defined as $\sin(x)/x$, and $\varepsilon(\psi) = \cos\Big(2\pi\rho(t + t_\Delta)^2 - 2\psi - (\pi/4)\Big)$ is the phase dependent processing error .

There are several things to notice about Equation (2.18). Firstly, on the right hand side of equation the first term produces a peak at time $t = t_\Delta$. This is the term that is useful for spectrum analysis. When this term is larger than the other terms, a good signal to noise ratio is possible.

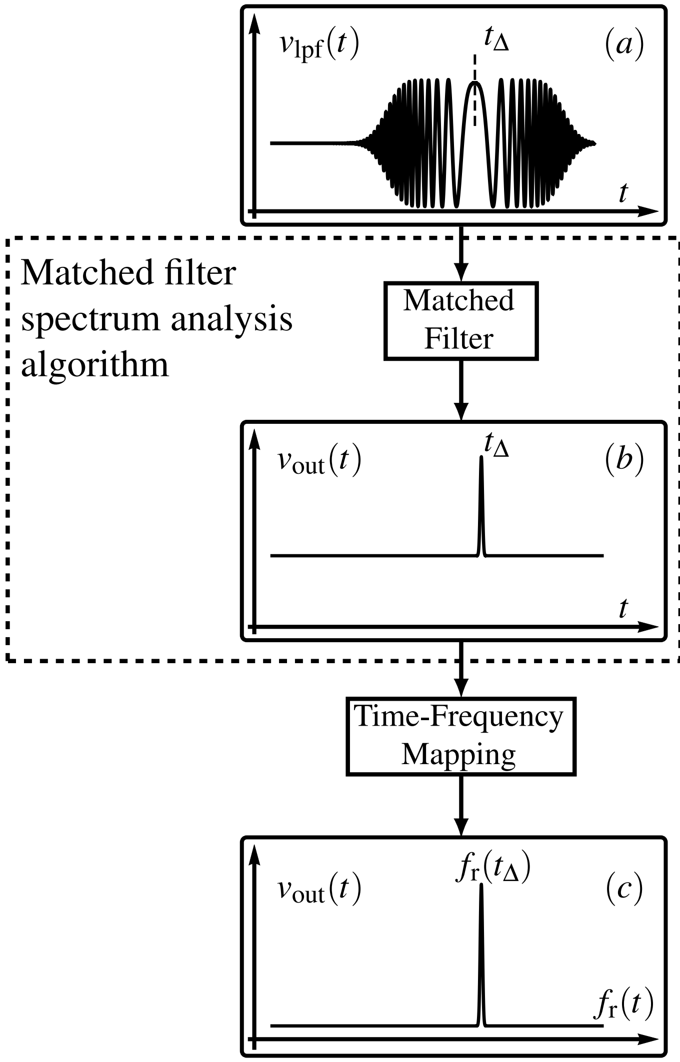

Figure 2.4: Spectrum analysis with matched filter. (a) The mixed and filtered signal, $v_{\text{lpf}}(t)$, where $h_{\text{lpf}}(t)$ had a flat pass band. (b) A matched filter is applied to the signal, resulting in the spectrum is shown by $v_{\text{out}}(t)$ as a function of time. (c) The time axis is mapped to frequency, resulting in a frequency vs magnitude plot.

The other two terms on the right hand side represent processing noise. The last term represents a dc offset that increases with scan rate ρ or decreases with increasing scanning bandwidth Δf_{ch}. This term can be easily removed by post signal processing.

The middle term on the right hand side of Equation (2.18) represents processing noise that is localized at time $t = t_{\Delta}$. Because it is located at the same time as the signal term, it directly influences the reading of the signal amplitude. This term is difficult to remove by signal processing. The impact of this term can be decreased by increasing Δf_{ch}, or by decreasing scan rate ρ.

The middle term on the right hand side of Equation (2.18) is also influenced by the phase difference ψ between $i_{\mathrm{ext}}(t)$ and $r(t)$. The error in responsivity can be calculated analytically by restating Equation (2.18) at time $t = t_{\Delta}$ and neglecting the last term,

$$v_{\mathrm{out}}(t = t_{\Delta}) = 1 + \varepsilon(\psi)\frac{\sqrt{2\rho}}{2\Delta f_{\mathrm{ch}}}\,. \tag{2.19}$$

Of course, $\varepsilon(\psi)$ is a cosine function and thus can vary from a maximum of 1 to a minimum of -1, or $|\varepsilon(\psi)| \leq 1$. Thus, to adequately detect the amplitude of a single tone external signal, this algorithm requires that $2\rho \ll \Delta f_{\mathrm{ch}}^2$. Likewise, the uncertainty in amplitude is $\propto \sqrt{2\rho}/2\Delta f_{\mathrm{ch}}$ in the detectable signal.

Fast Fourier transform

Another spectrum analysis algorithm involves digitization and performing spectrum analysis in the digital domain. This is shown in Figure 2.5[25]. This algorithm begins with example curve for $v_{\mathrm{lpf}}(t)$, where $h_{\mathrm{lpf}}(t)$ has a flat passband, as depicted in Figure 2.4(a). Then, the signal is digitized with an analog to digital converter (ADC). Once the signal is in the digital domain, a fast Fourier transform (FFT) is performed on the signal.

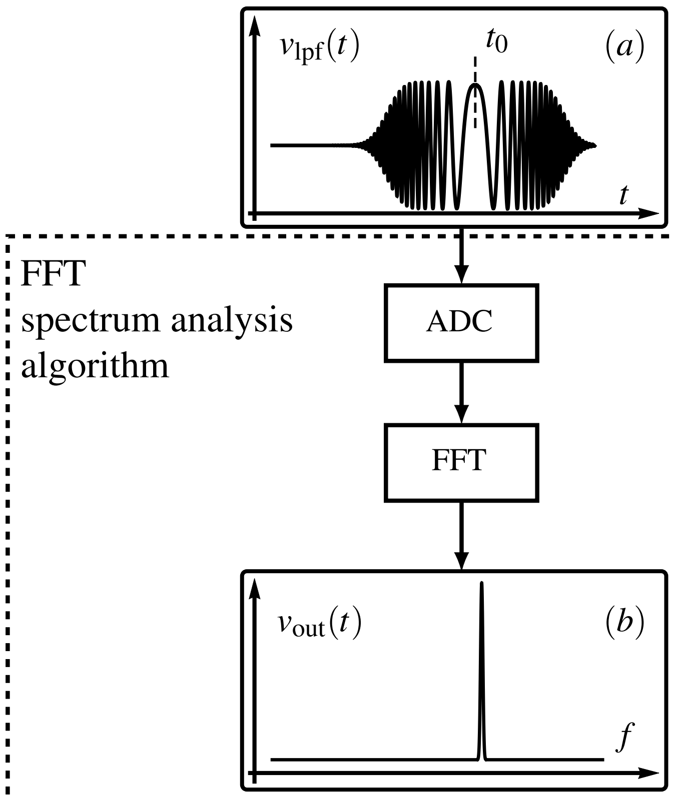

Figure 2.5: Spectrum analysis with fast Fourier transform. (a) The mixed and filtered signal, $v_{\rm lpf}(t)$, where $h_{\rm lpf}(t)$ has a flat pass band. (b) The signal is digitized with an analog to digital converter, and a FFT is performed, resulting in a frequency vs magnitude plot.

This method of spectrum analysis has many benefits. For example, phase information is retained during spectrum analysis. However, there are drawbacks to this method. Firstly, to avoid quantization errors, the ADC must operate with high resolution. Generally, to operated at high resolution, an ADC spectrum analyzer can only operate over a limited scanning bandwidth[25]. Second, this method does not perform well with pulsed signals [25]. As mentioned in subsection 1.2.3, one possible application of a STNO based spectrum analyzer is to perform fast spectrum analysis on pulsed radar signals over a wide bandwidth. Thus, this FFT spectrum analysis algorithm is not a good fit for fast spectrum analysis.

These drawbacks can be overcome by using numerous ADCs, each with a limited bandwidth, to cumulatively cover a wide spectrum with high resolution. This is called “real time” spectrum analysis. While effective, these systems are bulky, technically complex, and expensive. In contrast, as will be shown in this dissertation, by using STNOs and an appropriate algorithm, it is possible to create a technically simple nanoscale system with performance characteristics suitable for performing real time spectrum analysis.

2.2.3 Theoretical limit for resolution bandwidth

This subsection presents the theoretical limits for resolution bandwidth. It is perhaps easiest to begin with the fairly well known Heisenberg uncertainty principle, which was formulated in 1927. If x represents the position of an electron, and p represents the momentum of an electron, the Heisenberg uncertainty is given by a simple formula:

$$\Delta x \Delta p \geq h, \tag{2.20}$$

where Δx is the uncertainty in the position of an electron, and Δp is the uncertainty in the momentum of the electron, and h is the Planck constant. This formula states is that if the position of an electron is measured with great certainty, the momentum cannot be

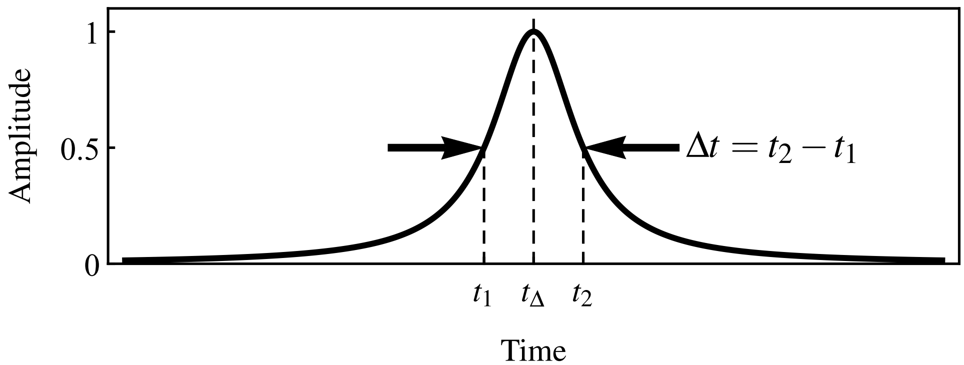

Figure 2.6: Resolution bandwidth and FWHM. The spectrum analysis detection peak, which has a full width at half maximum (FWHM) time-span of $\Delta t = t_2 - t_1$. In this case, the RBW is approximately $f_\mathrm{r}(t_2) - f_\mathrm{r}(t_1) = \rho \Delta t$.

measured with great certainty. Likewise, if the momentum of an electron is measured with great certainty, the precise position of the electron cannot be known with great certainty.

The theoretical limit for RBW can be computed from a similar formula, which is called the bandwidth theorem. The significance of the bandwidth theorem was first reported by Gabor in 1946 [33]. The bandwidth theorem is commonly written as [34]

$$\Delta f \Delta t \geq 1\,. \tag{2.21}$$

As it relates to spectrum analysis, in this equation $\Delta f = f_\mathrm{c}$, the pass bandwidth of the lowpass filter in Equation (2.11) (For cases where $f_\mathrm{c} > \Delta f_\mathrm{ch}$, $\Delta f = \Delta f_\mathrm{ch}$). The time span of the detection peak, Δt, can be explained as follows. Consider the detection curve shown in Figure 2.6, with a peak at t_Δ. This peak, at time t_Δ, indicates that the external signal has a frequency given by $f_\mathrm{r}(t_\Delta)$. The peak has a finite width, as was depicted in Figure 2.3(c) and Figure 2.4(c). The peak at half maximum (amplitude = 0.5) has a time span of $\Delta t = t_2 - t_1$.

With Equation (2.5), the resolution bandwidth RBW $= f_\mathrm{r}(t_2) - f_\mathrm{r}(t_1) = \rho \Delta t$. Note that $f_\mathrm{r}(t_2) - f_\mathrm{r}(t_1)$ is also known as the linewidth. Thus, a small time span Δt corresponds with a good RBW. From Equation (2.21), it is evident that $\Delta t = 1/f_c$ corresponds with the theoretical best RBW, which can be given as

$$\mathrm{RBW}_0 = \frac{\rho}{f_c}. \tag{2.22}$$

Which is the absolute best RBW possible for a given scan rate ρ. Note that when $f_c > \Delta f_{ch}$, this expression will be $\mathrm{RBW}_0 = \rho/\Delta f_{ch}$.

2.3 Spin torque nano oscillators

The primary focus of this dissertation is to evaluate the viability of using STNOs in a fast spectrum analysis system. We are proposing to use an STNO to generate a chirp according to Equation (2.7), with a chirp sweep time of T, a scanning bandwidth Δf_{ch}, and a scan rate ρ. The advantages of STNOs relate to size, tuning speed, and scanning bandwidth. This section seeks to familiarize readers with the basics of STNOs.

As these spintronic nanoscale oscillators have been studied extensively in the past few decades, this section is not comprehensive; it is merely an overview of relevant characteristics of STNOs. For further information, several review articles are fairly comprehensive [1, 35, 36, 37].

2.3.1 Magnetic tunnel junctions

As mentioned earlier, STNOs can be based on magnetic tunnel junctions (MTJs) or spin valves. For the last decade, MTJs have served as hard drive read heads. Prior to that, spin valves were the critical technology for hard drive read heads. How MTJs and spin valves function provides a convenient introduction to how STNOs function.

Both MTJs and spin valves operate on a similar principle. They are constructed with 3 layers, as shown in Figure 2.7(a). Essentially, there are two layers that are composed of ferromagnetic materials that are separated by a non-magnetic material.

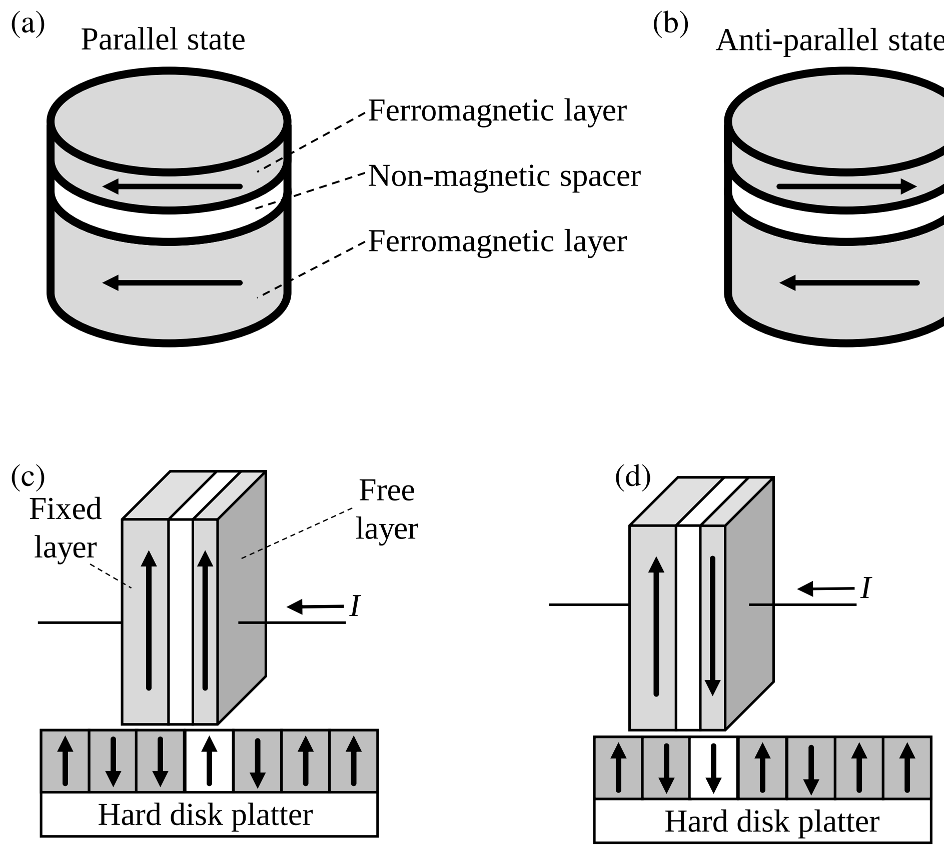

Figure 2.7: MTJ as a hard drive read head. (a) A basic MTJ consists of 3 layers, two ferromagnetic layers separated by a non-magnetic spacer. This MTJ is defined as being in a "parallel state" because the FM layers have magnetizations that are oriented in the same direction. (b) This MTJ is defined as being in an "anti-parallel state" because the FM layers have magnetizations that are oriented in the opposite direction. The anti-parallel state has a higher resistance than the parallel state. (c) An MTJ near a hard disk, acting as a hard drive read head. The free layer is aligned with the nearest magnetic element, forcing the MTJ into the parallel state, with a logic "low" resistance. (d) The free layer is aligned with the magnetic element, forcing the MTJ into the anti-parallel state, with a logic "high" resistance.

Ferromagnetic magnetic materials are materials that have an intrinsic magnetization; they are tiny permanent magnets. The direction of the magnetization for all ferromagnetic materials in Figure 2.7 are shown with arrows. In hard drive read heads, it is common for the magnetization of each magnetic layer to be oriented in a direction that is “in-plane”. In the Figure 2.7(a), the magnetization of the layers are both in-plane and in parallel, while in Figure 2.7(b), the magnetizations of the layers are anti-parallel. The parallel and anti-parallel states consitute the lowest energy states of the MTJ. The MTJ has a higher resistance while in the anti-parallel state than while in the parallel state.

The non-magnetic material, which is called a spacer, in spin valves is composed of a metal (for example, copper) and in MTJs of a dielectric material (for example, Magnesium Oxide). The resistance observed in spin valves is called Giant magnetoresistance (GMR). This effect was first observed in 1988 by Peter Grunberg and Albert Fert. It is notable that in 2007, they received the Nobel Prize in Physics for their efforts. The resistance observed in MTJs is called tunneling magnetoresistance (TMR). Because MTJs have a dielectric spacer layer, they tend to have a higher resistance, and thus have improved performance over spin valves.

Typically, the ferromagnetic layers of both spin valves and MTJs have one layer that is called the fixed layer. It is called a fixed layer because the direction of magnetization is relatively fixed, with a single orientation. There are many ways to fix the magnetization in a single direction; one of which is to make the fixed layer relatively thick.

Both spin valves and MTJs will have one ferromagnetic layer that is called the free layer. It is called the free layer because the direction of magnetization is free to move and rotate to match the orientation of an external magnetic field.

Thus, hard drive read heads work as follows, as shown in Figure 2.7(c) and (d). In this figure, the read head is near a hard drive disk that stores single bits as a magnetic domain. Each magnetic domain, which is a tiny permanent magnet, radiates a magnetic field. This magnetic field is strong enough to change the orientation of the magnetization in the free layer, but not the fixed layer. This results in a change of resistance of the read head. When a current is passed through the read head, a change in the memory state can be detected by a change in resistance. This is shown in Figure 2.7(c), where the stored bit to be read is oriented in an upwards direction. The free layer magnetization is oriented in the same oriented direction, and the two layers of the head are aligned in parallel. This results in a lower GMR or TMR, and hence when a current passes through the junction, a lower voltage results. In Figure 2.7(d), the read head moves left to the next bit, which is oriented in a downward direction. The free layer magnetization is reoriented to match the magnetization of the stored bit, and the two layers of the head are now anti-parallel. This results in a higher GMR or TMR, which is detected when the current passes through the junction and a higher voltage results.

Thus, it is useful that the resistance of these structures changes based on the orientation of the fixed and free layer magnetization. It is important to understand *why* the resistance changes when the free layer magnetism is reoriented. This can be understood as follows. An electric current passing through a spin valve or MTJ is, of course, composed of electrons. Every electron has an intrinsic spin, and thus an intrinsic magnetic alignment. This intrinsic magnetic alignment can be called the "direction of electron spin". When an electron is passing through a ferromagnet, it can pass through a ferromagnet with less resistance if its direction of electron spin aligns with the magnetization of the ferromagnet.

Additionally, when a conducting electron flows through a ferromagnetic material, the direction of spin of the conducting electron can change to match the magnetization of the ferromagnet. An electron that is aligned with the local magnetization is called *spin polarized*[1]. When a current of electrons aligns with the local magnetization, it is called spin polarized current, which is an electric current where the direction of electron spins of the conduction electrons are oriented on the same direction.

Hence, magnetic tunnel junctions and spin valves acting as read heads function as follows:

1. Before electrons enter the fixed layer, electron spins are randomly oriented.
2. On passing through the fixed layer, some of the electrons become spin polarized.
3. The electrons retain their spin polarization on passing through the thin spacer layer.
4. Then they enter the free layer.
5. If the magnetization of the free layer is anti-parallel with the fixed layer, the free layer magnetization will also be anti-parallel with the spin polarized electrons. In this situation, the MTJ will be in a "high" resistance state.
6. If the magnetization of the free layer is parallel with the fixed layer, the free layer magnetization will also be parallel with the spin polarized electrons. In this situation, the MTJ will be in a "low" resistance state.
7. A current is passed through the MTJ. The resulting voltage drop accross the MTJ will result in a change in voltage that depends on the state of the MTJ. Thus, the two resistance states can thus be assigned logic high and low values.

Thus, data stored on a hard drive platter can be read with an MTJ.

Interestingly, under certain conditions, the spin polarized electrons disturb the direction of the free layer magnetization and induce a torque called the spin transfer torque. This is the topic of the next subsection.

2.3.2 Spin transfer torque and magnetic tunnel junctions

Consider an MTJ placed in a strong external magnetic field, as shown in Figure 2.8(a). The external magnetic field, $\mathbf{B}_{\mathrm{ext}}$, is oriented in the $\hat{\mathbf{z}}$ direction. In the presence of a strong magnetic field, the free layer magnetization $\mathbf{m}$ is aligned with $\mathbf{B}_{\text{ext}}$. The fixed layer magnetization is denoted by a unit vector $\mathbf{p}$. In the absence of the external magnetic field, $\mathbf{p}$ would be oriented in the $\hat{\mathbf{y}}$ direction. In the presence of $\mathbf{B}_{\text{ext}}$, the fixed layer magnetization is canted by an angle β, and thus has the direction $\mathbf{p} = \cos(\beta)\hat{\mathbf{y}} + \sin(\beta)\hat{\mathbf{z}}$.

When a dc current, called the bias current I_{bias}, flows from the top layer down, the conducting electrons will flow up from the bottom layer. As they traverse the fixed layer, some percentage of the conducting electrons will become spin polarized and align their spins with $\mathbf{p}$. The proportion of electrons that are directed along $\mathbf{p}$ is called the spin polarization efficiency. Spin polarization efficiency is denoted by η_0.

In an MTJ with an appropriately thin spacer layer, the conducting electrons leave the fixed layer and pass through the spacer layer and enter the free layer while retaining their spin polarization. The spin polarized conducting electrons directed along $\mathbf{p}$ have a magnetization direction that is different from the free layer magnetization direction $\mathbf{m}$. The different magnetization directions cause the conduction electrons to induce a torque on the localized free layer electrons. This torque is called the spin transfer torque (STT), and is denoted by T_{stt} [1, 35, 38, 39]. T_{stt} is given by

$$T_{stt}(I_{\text{bias}}) = \alpha_{\text{J}} I_{\text{bias}} \mathbf{m} \times [\mathbf{m} \times \mathbf{p}] \,. \tag{2.23}$$

In this equation, $\mathbf{m}$ is the normalized unit-length magnetization of the free layer, while $\mathbf{p}$ is the normalized unit-length magnetization of the fixed layer. and α_{J} is the spin-torque coefficient, which is given by $\alpha_{\text{J}} = |\gamma|\hbar\eta_0/(2\mu_0 M_s eV)$. Here γ is the gyromagnetic ratio, $\hbar$ is the reduced Planck constant, μ_0 is the free space permeability, M_s is the free layer saturation magnetization, e is the fundamental electric charge, and V is the volume of the free layer[1]. Please note that the notation used here is adapted from [1, 40].

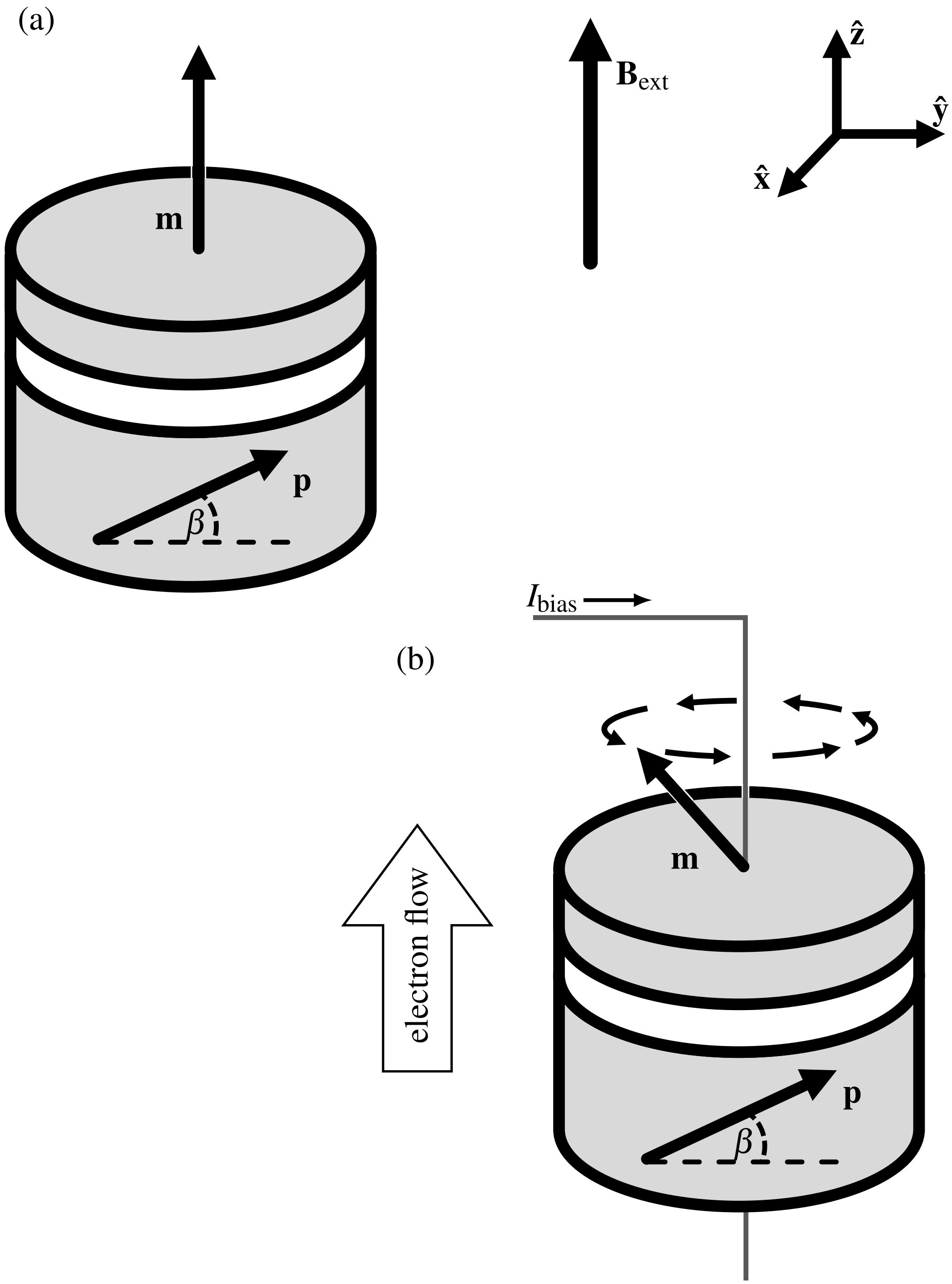

Figure 2.8: Diagram of an STNO based on a magnetic tunnel junction. (a) The MTJ in a strong static magnetic field $\mathbf{B}_{\text{ext}}$ that is directed normal to the cross section of the MTJ. In this field, $\mathbf{m}$ is aligned with $\mathbf{B}_{\text{ext}}$, and $\mathbf{p}$ is canted by an angle β. (b) The same MTJ with a strong bias current I_{bias}. This current can cause the precession of $\mathbf{m}$ about $\mathbf{B}_{\text{ext}}$.

It is evident from the presence of η_0 in Equation (2.23) that the strength of this torque dependend on the quantity of spin polarized electrons. This means that a stronger I_{bias} will result in more spin polarized electrons and hence a stronger STT. Thus, a stronger bias current I_{bias} will induce a stronger STT, which increases the angle between $\mathbf{m}$ and $\mathbf{B}_{\text{ext}}$.

2.3.3 STNO mathematical model

In addition to STT, the behavior of $\mathbf{m}$ is influenced by a variety of factors. Interestingly, when I_{bias} is greater than a certain threshold current I_{th}, this can lead to self-sustained magnetization precession in the free layer[1]. The origins of this precession will be explained in this section. Precession of the free layer magnetization is depicted in Figure 2.8(b), which shows $\mathbf{m}$ precessing about $\mathbf{B}_{\text{ext}}$. The magnetization precession has a frequency that, for the geometry depicted in Figure 2.8(b), increases with the increase in angle between $\mathbf{m}$ and its equilibrium direction. Thus, a stronger bias current I_{bias} will induce a stronger STT, which increases the angle between $\mathbf{m}$ and $\mathbf{B}_{\text{ext}}$, which increases the precession frequency. This can be thought of as precession frequency being directly related to I_{bias}.

As described in subsection 2.3.1, the tunneling magnetoresistance of this MTJ depends on the relative orientation of $\mathbf{p}$ and $\mathbf{m}$. Hence, the precession of $\mathbf{m}$ will manifest macroscopically as an oscillating TMR. The fact that these oscillations are induced by spin transfer torque leads to the name spin torque nano-oscillator.

The magnetization dynamics in the MTJ free layer under the action of a dc current can be modeled using the Landau-Lifshitz-Gilbert-Slonczewski (LLGS) equation:

$$\frac{\mathrm{d}\mathbf{m}}{\mathrm{d}t} - |\gamma|\mathbf{B}_{\text{eff}} \times \mathbf{m} = \alpha_{\mathrm{G}}\mathbf{m} \times \frac{\mathrm{d}\mathbf{m}}{\mathrm{d}t} + \alpha_{\mathrm{J}} I_{\text{bias}} \mathbf{m} \times [\mathbf{m} \times \mathbf{p}]\,. \tag{2.24}$$

In this equation, $\mathbf{B}_{\text{eff}} = \mathbf{B}_{\text{ext}} - \mu_0 M_{\text{s}}(\mathbf{m} \cdot \hat{\mathbf{z}})\hat{\mathbf{z}}$ is the effective field on the free layer, and α_{G} is the Gilbert damping constant. Other variables were defined with Equation (2.23). The notation used here is adapted from [1, 40].

As stated earlier, the free layer magnetization direction $\mathbf{m}$ can change depending on its local environment. Equation (2.24) describes how $\mathbf{m}$ can precess about $\mathbf{B}_{\text{ext}}$ in response to a set of conditions that will now be described.

The first term on the right hand side of Equation (2.24) models a damping torque. When the free layer magnetization departs from equilibrium alignment with $\mathbf{B}_{\text{ext}}$, this term models the torque that returns $\mathbf{m}$ to its equilibrium direction. This term can be referred to as the Gilbert damping torque, and is directed towards $\mathbf{B}_{\text{ext}}$.

The second term on the right hand side of Equation (2.24) is the spin transfer torque, which was described in Equation (2.23). This term is commonly referred to as the Slonczewski torque or the anti-damping torque. The STT depends on $\mathbf{p}$ and I_{bias}. When $\mathbf{p}$ and $\mathbf{m}$ are not aligned, the triple cross product in the anti-damping term is nonzero. For a properly oriented $\mathbf{p}$, this vector will oppose the Gilbert damping torque, and thus be directed away from $\mathbf{B}_{\text{ext}}$ and act as an anti-damping torque. The magnitude of this anti-damping torque is linearly dependent on the magnitude of I_{bias}. Note that the current must flow in the correct direction to properly oppose the Gilbert damping torque.

When there is a non-zero Slonczewski torque, $\mathbf{m}$ will be pulled away from alignment with $\mathbf{B}_{\text{ext}}$, and begin to precess as shown in Figure 2.8(b). The system will enter a stationary state when the Gilbert and Slonczewski terms are equal in magnitude with opposite directions. This condition reduces the Landau-Lifshitz equation to:

$$\frac{\mathrm{d}\mathbf{m}}{\mathrm{d}t} = |\gamma|\mathbf{B}_{\text{eff}} \times \mathbf{m}. \tag{2.25}$$

This describes the precession of $\mathbf{m}$ in three dimensions. The phase of precession is given by [1]

$$\theta_{\mathrm{stno}}(I_{\mathrm{bias}},t) = \cos^{-1}(\mathbf{m}\cdot\mathbf{p})\,. \tag{2.26}$$

The angular frequency of precession is given by the derivative of phase,

$$\omega_{\mathrm{stno}}(I_{\mathrm{bias}},t) = \frac{\mathrm{d}\theta_{\mathrm{stno}}(I_{\mathrm{bias}},t)}{\mathrm{d}t}\,. \tag{2.27}$$

Likewise, $\mathbf{m}$ has a precession frequency of $f_{\mathrm{stno}}(I_{\mathrm{bias}},t) = \omega_{\mathrm{stno}}(I_{\mathrm{bias}},t)/2\pi$. In this thesis, $f_{\mathrm{stno}}(I_{\mathrm{bias}},t)$ is called the STNO frequency.

Note that $\theta_{\mathrm{stno}}(I_{\mathrm{bias}},t)$ and $\omega_{\mathrm{stno}}(I_{\mathrm{bias}},t)$ are explicit functions of I_{bias}. This is because the strength of the STT, as modeled by the Slonczewski term in Equation (2.24), is dependent on I_{bias}. A change in STT changes the angle that $\mathbf{m}$ has with $\mathbf{B}_{\mathrm{ext}}$, thus changing the oscillation frequency through the dynamics in Equation (2.24).

Once again, the relative orientations of $\mathbf{m}$ and $\mathbf{p}$ in spin valves and MTJs change the device resistance. The TMR for an MTJ based STNO can be modeled as:

$$R(I_{\mathrm{bias}},t) = R_0 - \Delta R_{\mathrm{stno}}\cos(\ \theta_{\mathrm{stno}}(I_{\mathrm{bias}},t)\ )\,. \tag{2.28}$$

In this equation, R_0 is the average resistance of the MTJ, and ΔR_{stno} is the amplitude of TMR oscillations. Note that the frequency of precession, $\omega_{\mathrm{stno}}(I_{\mathrm{bias}},t)$ is the same for both $\mathbf{m}$ and TMR. The magnetization precession thus manifests macroscopically as a TMR, and from an applications perspective, can be seen as a simple "oscillating resistance". It is convenient to denote the oscillating resistance as

$$r_{\mathrm{stno}}(I_{\mathrm{bias}},t) = -\Delta R_{\mathrm{stno}}\cos(\ \theta_{\mathrm{stno}}(I_{\mathrm{bias}},t)\ )\,. \tag{2.29}$$

This section has described one example how an STNO can be constructed. There are many other physical configurations[1, 2, 3, 36, 41, 42]. The core point of this subsection is that by using nanoscale fabrication and the properties of ferromagnetic

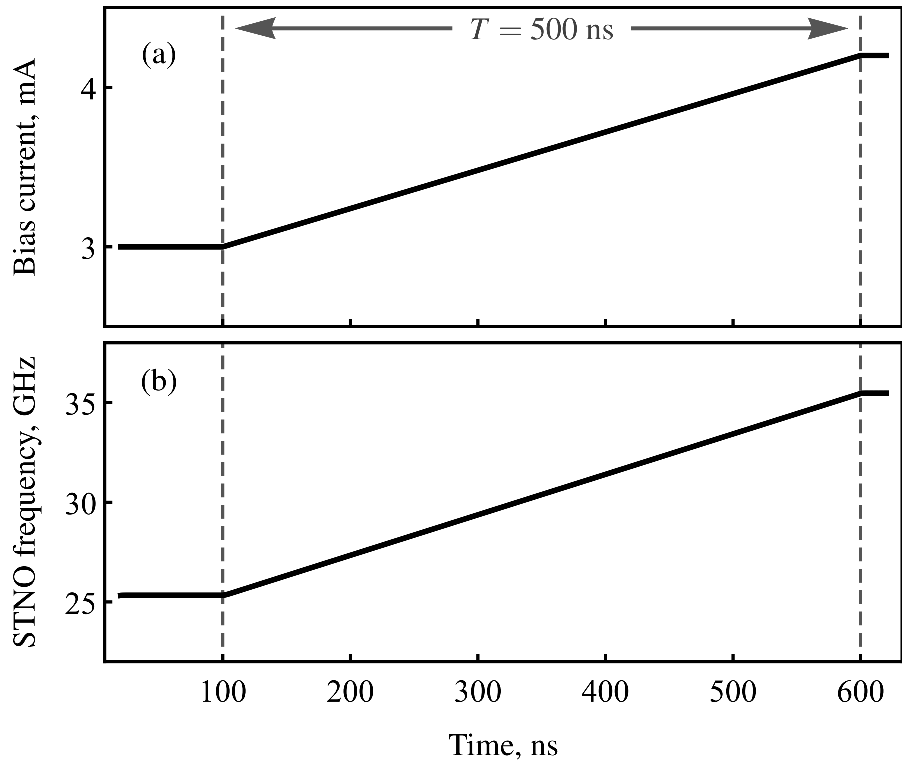

Figure 2.9: STNO as an oscillating resistor. (a) The bias current that will tune the STNO resistance oscillation frequency. The current is 3 mA for the first 100 ns, then increases linearly to 4.2 mA over 500 ns. After this, the current is constant at 4.2 mA. (b) In response to the bias current, the STNO resistance oscillates at 25 GHz until 100 ns. Then, as the bias current increases, the STNO resistance oscillation frequency increases linearly to 35 GHz over a 500 ns interval. After this the STNO is steady at 35 GHz.

materials, an oscillating resistance can arise from an STNO whose frequency of oscillation depends on the magnitude of bias current.

2.3.4 STNO as an oscillating resistor

When viewed from a macroscopic perspective, STNOs are oscillating resistors. The resistance oscillations have a frequency that can be easily tuned with a dc current. The relationship between current and the frequency of STNO resistance oscillations is shown in Figure 2.9. First, the current used to tune the frequency of resistance oscillations is shown in Figure 2.9(a). For the first 100 ns, the current is held constant at 3 mA. Then, it increases linearly to 4.2 mA over a 500 ns period. After this, the dc current is held constant at 4.2 mA.

Figure 2.9(b) shows the simulated response of the STNO to this dc current. For the first 100 ns, the resistance of the STNO oscillates at $\sim$25 GHz. Then, when the current increases in a linear manner, the frequency of STNO resistance oscillations increases linearly to $\sim$35 GHz. After this, when the dc current is held constant, the frequency of resistance oscillations remain constant at $\sim$35 GHz. This demonstrates that SNTOs are tunable microwave frequency signal sources.

2.3.5 Key features of STNOs

STNOs have a number of characteristics that make them favorable for implementation as the local oscillator in a spectrum analyzer. These features are covered briefly in this subsection, which is summarized in Table 2.2

Size

The physical realization of STNOs have taken many forms. For example, spin valves and MTJs, both of which are nano-sized devices, have served as hard drive read heads for nearly two decades and thus have been extensively manufactured. Under certain conditions, these devices can act as STNOs. There are also implementations of STNOs that are neither spin-valve nor MTJ[41, 42]. Thus, the absolute size and geometry of an STNOs can vary.

As a general rule, the cross sectional area of an STNO based on an MTJ will be between 100 and 800 nm^2 [1]. Note that a 100 nm^2 circular structure would would have a radius of $\sim$6 nm. STNOs based on an MTJs are constructed with a stack of various materials, with thicknesses that generally range from 10 to 100 nm. The STNOs simulated in this dissertation will be based on MTJs.

Table 2.2: Key features of STNOs

STNO feature	Amount	Brief Description
Size	100 - 800 nm^2	Typical STNO size.
Generation frequency	> 65 GHz	Frequencies that can be generated by an STNO.
Tunable bandwidth	> 10 GHz	The bandwidth that a single STNO can be tuned by changing the bias current.
Dynamic tuning	> 2 GHz/ns	Speed that STNO frequency can be tuned. Maximum scan rate.
CMOS compatibility	< 20 nm	Can be included with popular silicon based integrated circuits.
Radiation hard	> 10 Mrad	Ability to function in the presence of radiation.

Generation frequency

STNOs can generate microwave frequency signals. It is often cited that the STNO frequency can "have a maximum expected operating frequency beyond 65 GHz"[4]. Recent experimental results have observed an STNO frequency as high as 70 GHz [43]. In that experiment, the authors estimated that the STNO oscillated with frequencies as high as 150 GHz, which could not be observed due to test equipment limitations.

For low frequency performance, STNOs can generate signals in the sub-GHz range. One experimental publication, for example, observed a generation frequency of 200 MHz [44].

Tunable bandwidth

Tunable bandwidth, which describes the bandwidth over which the STNO can be tuned, varies greatly between different STNOs. In one experiment, the linear tuning of an STNO frequency by a dc bias current had a bandwidth of 13 GHz [2]. This is shown in Figure 2.10.

In addition to varying the bias current, it is possible tune the STNO frequency by changing the magnitude of an external magnetic field while holding the bias current constant. When holding the bias current constant and changing an external magnetic field, STNOs were observed to have a tunable bandwidth as wide as 35 GHz[3]. This is shown in Figure 2.10(d).

Dynamic tuning

Dynamic tuning refers to how quickly the STNO frequency can be tuned. This characteristic is different from tunable bandwidth; it is instead more concerned with the *speed* of tuning. It is important to note that because STNOs are small, they have a small intrinsic capacitance and a small intrinsic inductance. This means that STNOs have a small time constant, and thus can be rapidly tuned.

There are several notable published experimental studies that demonstrate that STNOs are capable of being rapidly tuned[45, 46, 47]. Two of these papers are primarily concerned with the modulation of STNO precession frequencies[45, 46]. One specifically investigates how quickly STNOs can be tuned [47]. That paper found, essentially, that STNOs can be tuned "between two frequencies differing by 25% in less than ten periods."

While these studies demonstrated that STNOs are capable of being rapidly tuned, they do not directly address the ability of STNOs to be tuned in a linear manner. For spectrum analysis, we are interested in tuning an STNO in a linear fashion. Specifically, the generated frequency should be tuned as a linear chirp according to Equation (2.5). As no published studies address the ability of STNOs to generate linear chirps, this will be addressed by theory in section 4.1. There, it will be shown that STNOs are capable of linear tuning faster than 2 GHz/ns.

Compatibility with CMOS

Integrated circuits based on complementary metal-oxide-semiconductor (CMOS) technology are a widely used technology in most modern electronics. STNOs based on MTJs can be embedded in CMOS [48, 49, 50]. For example, an Arizona company named Everspin is manufacturing magnetic memory for commercial use. The memory uses MTJs as memory elements, and is called "embedded magnetoresistive random-access memory (eMRAM)". Their products can be fully integrated with CMOS. Quoting from their website:

> Everspin has significant experience in enabling silicon suppliers with eMRAM. In fact, roughly half of Everspin's total unit volume is embedded, and the applications range from consumer to aerospace. Our MRAM technology and proprietary IP enables us to provide non-volatile, fast-write embedded memory blocks that are

> compatible with CMOS Logic designs, targeted for 180 nm and 130 nm CMOS processes (for field-switched eMRAM), as well as 40 nm and 28 nm CMOS processes (for perpendicular-MTJ Spin Torque eMRAM).[49]

Thus, circuits with MTJs are regularly included with standard integrated circuits. It is notable that the eMRAM deployed in 28 nm integrated circuits use spin transfer torque to change memory states.

Radiation hard

Electronic elements are termed *radiation hard* when they can function in the presence of radiation. Radiation hard electronics are important for military and space applications. Because STNOs are constructed primarily of metals, they are far more tolerant of radiation than semiconductor electronics. According to one study, MTJ performance was unaffected by 10 Mrad radiation doses, and were insensitive to epithermal neutron fluence of $2.9 \times 10^{15}\,\mathrm{cm}^{-2}$ [51]. The gives spintronics in general, and a spectrum analyzer based on an STNO in particular, a host of potential space and military applications.

2.3.6 Brief literature review of STNOs

Experimental results showing the relationship between bias current and STNO frequency are shown in Figure 2.10. Figure 2.10(a) and (b) show experimental results obtained for a spin valve that was fabricated with a nano-contact geometry[2]. The nano-contact geometry, which is different from the MTJ presented in the previous section, uses a stack of thin films topped by an insulator. The diagram in Figure 2.10(a) shows cross section of the fabricated spin valve. The constituent layers are as follows, from bottom to top: the bottom is base electrode film, then a 20 nm fixed layer composed of $Co_{81}Fe_{19}$, then a 6 nm Cu spacer, then a 4.5 nm free layer composed of $Ni_{80}Fe_{20}$, then a cap layer composed 2 nm Cu and 3.5 nm Pd. Above this, there is an insulator composed of either poly(methymethacrylate) or SiO_2. After this stack was fabricated, a contact was

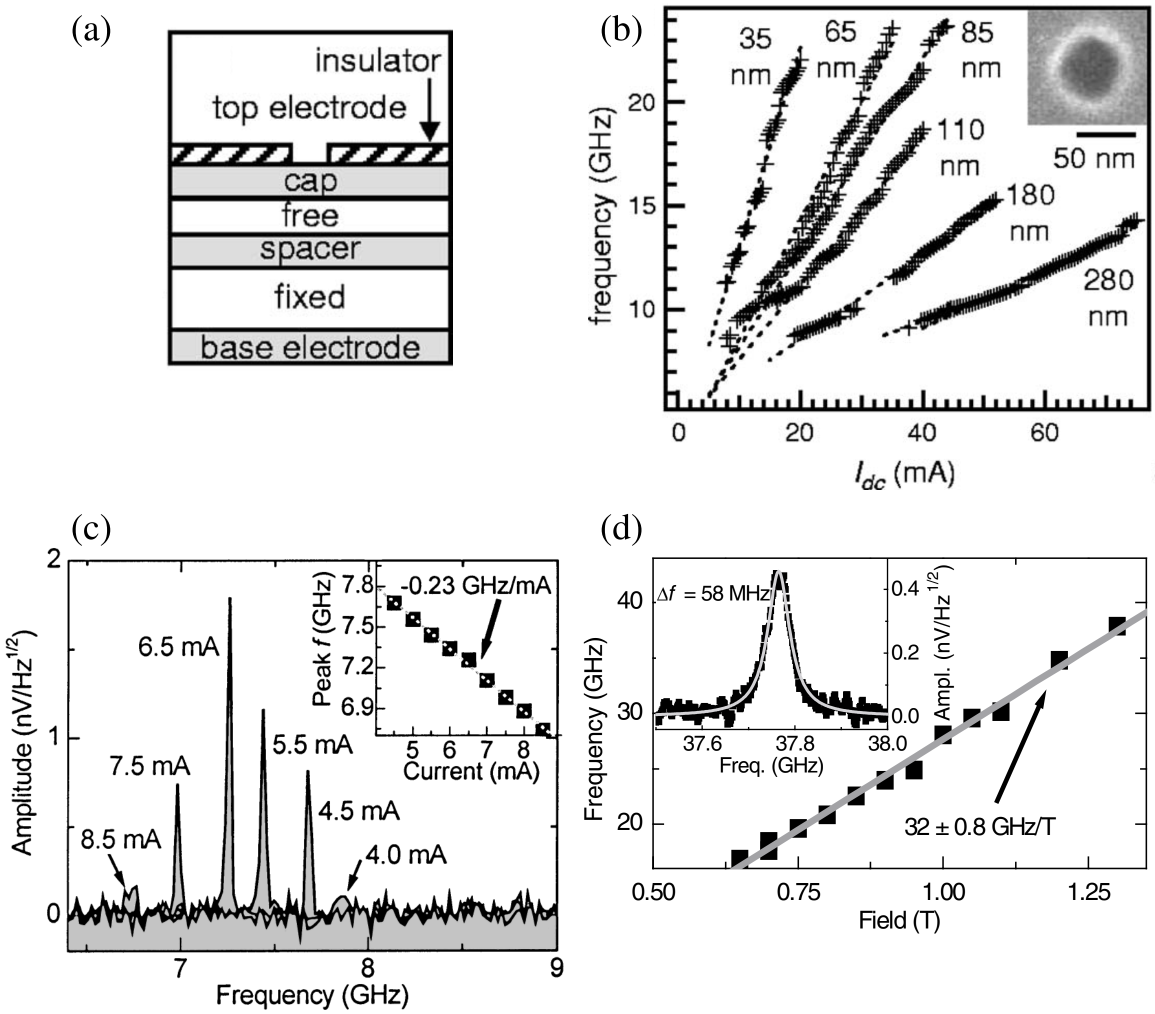

Figure 2.10: Experimental demonstration of STNO frequency vs. bias current. (a) Schematic of fabricated nano-contact spin valve [2]. Electron flow is from the fixed layer through the free layer, then through a contact whose size was varied from 35 nm to 280 nm. (b) Inset: Scanning electron microscopy image of a 60 nm diameter contact. (b) Frequency vs. bias current for STNOs with contact sizes that vary from 35 nm to 280 nm, as labeled. Crosses indicate measured points, and line of best fit shown with dashed lines. (c) Spectra of oscillations generated by an STNO in a 0.1 T in-plane bias field for currents ranging from 4.0 to 8.5 mA. (c) Inset: Relationship between bias current and peak generated frequency for the same conditions. (d) Variation of STNO generated frequency for a changing bias field amplitude. Top images were reprinted from [2] with permission of AIP Publishing. Bottom images were reprinted from [3] with permission of American Physical Society.

etched in the insulator, and then a top electrode was added to the stack. Current traverses the structure through this contact. An image of the structure is shown in the inset of Figure 2.10(b). It was obtained by scanning electron microscopy for a contact with a 60 nm diameter.

The relationship between the STNO generated frequency and the bias current I_{bias} for six different contact sizes in is shown in Figure 2.10(b). The measurements were taken at room temperature with an applied magnetic field $\mathbf{B}_{\text{ext}} = 10$ Oe, which was applied in the direction normal to the film. The sizes ranged from a diameter of 35 nm to 280 nm, and I_{bias} ranged from about 5 mA to 80 mA. Frequency measurements are shown by crosses, and dotted lines show linear fits. It is evident that these STNOs have a tunable bandwidth that can exceed 10 GHz. For example, in this figure the contact with an 85 nm diameter was able to oscillate with frequencies ranging from 11 GHz to 24 GHz. This corresponds to a tunable bandwidth of $\sim$ 13 GHz. This figure is shown here to emphasize that an STNO can be tuned linearly by I_{bias} with a tunable bandwidth greater than 10 GHz.

Figure 2.10(c) and (d) shows experimental results that were obtained with a spin valve that was fabricated with a nano-contact geometry, with a contact diameter of 40 nm[3]. Figure 2.10(c) shows the spectra taken for several values of current, from 4.0 mA to 8.5 mA with a 0.1 T bias field that is oriented in-plane. In these, the FWHM $\sim$20 MHz. The inset of Figure 2.10(c) shows the frequency of oscillation for this STNO, which varies linearly as a function of bias current.

In addition, when the magnetic field is varied, the frequency of oscillation is also tuned linearly. As shown in Figure 2.10(d), the frequency increased linearly from below 17 GHz to near 40 GHz as the field increased from 0.5 T to 1.5 T. This corresponds to a tunable bandwidth of $\sim$ 23 GHz. This figure is shown here to emphasize that an STNOs can be tuned over a scanning bandwidth that is greater than 20 GHz when it is tuned by an external magnetic field.

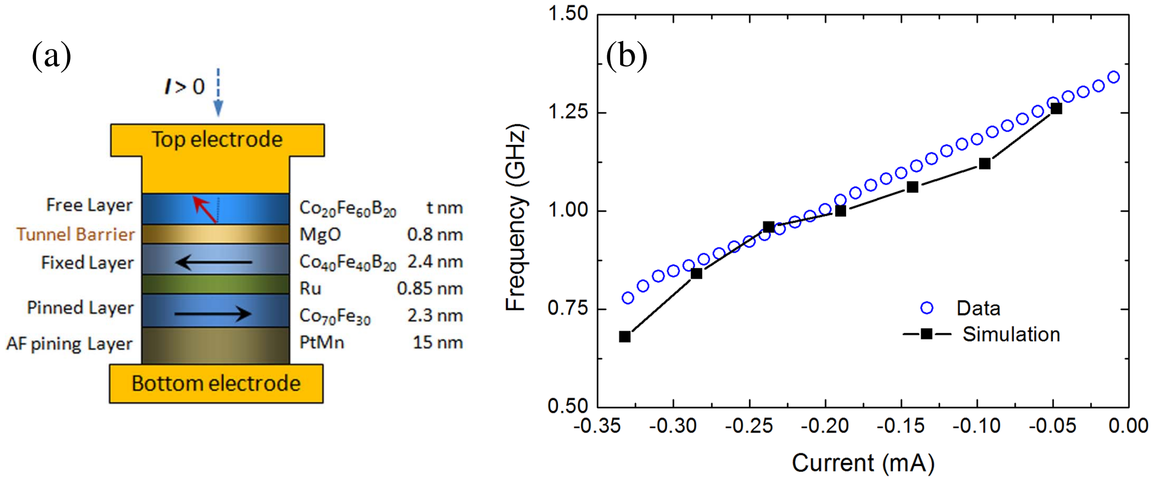

Figure 2.11: Zero bias field STNO. (a) Schematic of the MTJ as fabricated. Note the free layer has a canted magnetization, allowing this MTJ to act as a zero field STNO. (b) STNO operation without a bias magnetic field, frequency as a function of bias current. Reprinted from [52] under the Creative Commons CC-BY-NC-ND license.

A figure from a third published experimental result is shown in Figure 2.11 [52]. This experiment showed that an STNO can operate without an external bias field; specifically, for this STNO, $\mathbf{B}_{\text{ext}} = 0$. This was achieved by using an 150 nm $\times$ 70 nm elliptically shaped pillar with perpendicular magnetic anisotropy [53]. Figure 2.11(b) shows how frequency tuning relates to bias current for this device. In this case, when I_{bias} increases from -0.35 mA to -0.05 mA, the frequency increased from 0.7 to 1.25 GHz.

Thus, three different published STNO experiments have been reviewed. Since 2003, there have been hundreds of different experimental results. The purpose of this section was to emphasize that STNOs are indeed nanometer sized elements whose frequency of microwave signal generation can be easily, and quickly, tuned with a DC bias current. This thesis will show that these properties will allow STNOs to be useful for spectrum analysis.

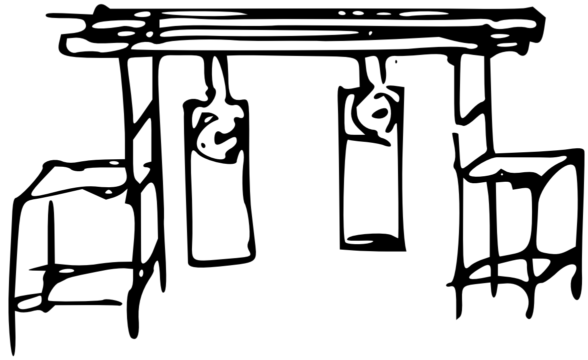

Figure 2.12: Phase locking of two pendulum clocks. This was drawn in 1665 by dutch scientist Christian Huygens. It shows two pendulum clocks hanging from a beam that is supported by two chairs. Reproduced from [54] with permission of Cambridge University Press.

2.3.7 Injection locking

Synchronization is a familiar phenomenon. For example, a small group of people are able to clap their hands in unison. Soldiers can march lock-step, and cardiac cells can coordinate to make a healthy heart beat correctly.

When two oscillators, with similar frequencies and phases, are by some means connected, their frequencies can synchronize by a physical process called *phase locking*. This was first written about in a 1665 letter by Christian Huygens, a Dutch astronomer, inventor, physicist, and mathematician. In his work developing accurate clocks, he discovered phase locking. His sketch of the experiment is reproduced in Figure 2.12. In this experiment, two pendulum clocks are hung from a beam that is suspended between two chairs. He described phase locking in a letter to his father:

> ... when we suspended two clocks so constructed from two hooks embedded in the same wooden beam, the motions of each pendulum in opposite swings were so much in agreement that they never receded the least bit from each other and the sound of each was always heard simultaneously. Further, if this agreement was disturbed by some interference, it reestablished itself in a short time [54]

Thus, Huygens observed that two pendulum clocks hanging from the same beam will, after a transition period, tick in unison. Huygens established that the clocks transmitted energy through the beam, allowing the two pendulums to become phase locked.

The frequency of an STNO can phase lock to a weak external microwave signal. The idea is that when a weak external signal, with frequency similar to the STNO oscillation frequency, is injected along with I_{bias} into the STNO, the STNO oscillation frequency will change to be exactly the same as the frequency of the weak external signal. When an STNO is phase locked to a weak external signal, it is said to be *injected locked* or *entrained*.

This is experimentally demonstrated in Figure 2.13(a) in [55]. In this figure, the frequency of the “free running” STNO is shown by black squares. This curve is called free running because the STNO is not influenced by an external signal. In essence, it describes how the SNTO behaves in the absence of an external microwave signal. Without the injection of an external signal, the free running frequency of oscillation increases linearly from 10.35 to 10.65 GHz.

When an external microwave signal, with amplitude of 29 mV, was injected into the STNO along with the bias current, the frequency of oscillation phase locks to the external signal and as a result the STNO has a plateau near 10.48 GHz. This is shown by blue triangles in Figure 2.13(a). Thus this shows experimentally that STNOs can be injection locked to an external signal.

An important characteristic of phase locking is the *phase locking bandwidth*. Phase locking bandwidth, denoted by Δf_{lock}, can be defined as the frequency bandwidth over which auto-oscillators can phase lock to another oscillator. This is demonstrated with a theoretical curve in Figure 2.13(b). In this figure, the thick black line shows the STNO oscillation frequency plotted as a function of free running frequency when an external microwave signal with a magnitude of 29 mV injected along with the bias current. This is

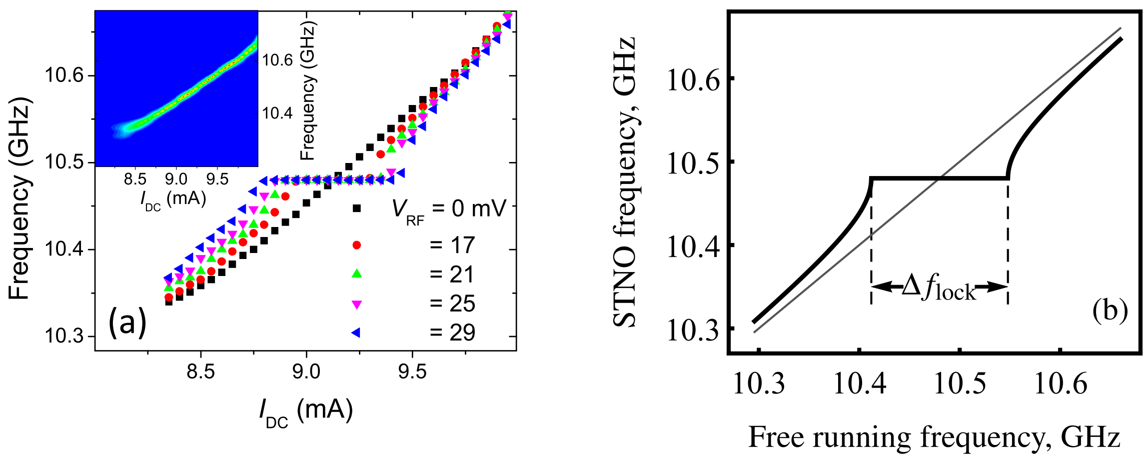

Figure 2.13: Experimental demonstration of STNO injection locking. (a) Inset: free running current frequency relation for a STNO. Colors show spectral output with logarithmic scale, where dark is 1 μW and light is 6 μW (a) Current frequency relation for an STNO whose bias current is modulated by a microwave signal. Black squares show a linear frequency relation for a free running oscillator. Blue blue triangles show the frequency relation when the bias current is modulated by a 29 mV microwave signal, where the STNO injection locks to the external signal at a frequency of ≈ 10.48 GHz. Modulation by other signal amplitudes are shown as labeled. (b) Theoretical curve showing the phase locking bandwidth Δf_{lock}. Figure on left is reprinted from [55] with the permission of AIP Publishing.

in contrast with the thin black line, which shows the free running frequency of the STNO. As is labeled on the figure, in this circumstance the STNO has a phase locking bandwidth $\Delta f_{\mathrm{lock}} = 0.15$ GHz. Due to their nonlinear properties, STNOs have an unusually wide phase locking bandwidth[1]. It is important to note that, as shown for different values of I_{ext} in Figure 2.13(a), the magnitude of the phase locking bandwidth depends on the magnitude of I_{ext}. This property will allow the use of injection locking to perform spectrum analysis, as will be shown in Chapter 4.

2.4 Antiferromagnetic tunnel junction

STNOs, as previously mentioned, can operate at frequencies above 65 GHz, with an estimated maximum frequency of 150 GHz[43]. There is much interest, from an applications perspective, in developing miniaturized electronics capable of performing spectrum analysis at even higher frequencies, in the bandwidth between 0.1 THz and 2 THz. There are currently no existing compact technologies that are capable of rapidly performing spectrum analysis on a signal with a frequency in the bandwidth between 0.1 and 10 THz. This bandwidth has been dubbed the "THz gap" because at these frequencies, traditional silicon electronics and traditional photonics hardware do not function effectively and thus are not capable of generating, detecting, or otherwise processing these signals [56, 57, 58, 59]. In contrast, antiferromagnetic (AFM) materials show an intrinsic resonant characteristics within the THz gap, and have been identified as building blocks for a new class of devices that will function at THz frequencies, as shown in many recent experimental and theoretical works [60, 61, 62, 63, 64, 65, 66, 67, 68, 69, 70, 71, 72, 73, 74, 75, 76, 77]. Thus far, there have been proposals for miniaturized THz frequency (TF) detectors [71, 72], sources [73, 74, 75], and spiking neurons for neuromorphic applications [76, 77].

Chapter 6 will describe how an antiferromagnetic tunnel junction (ATJ) composed of AFM materials can be used to produce a compact, simple spectrum analyzer that is functional in the THz gap. Recently, it has been proposed that an ATJ can serve as a tunable terahertz frequency signal source with a frequency of signal generation as high as 10 THz[75]. This structure is similar to an STNO, with a major difference: it features an antiferromagnetic material instead of a ferromagnetic material. Ferromagnetic materials, as mentioned above, have a single magnetization which allows them have a macroscopic magnetic dipole and thus become a permanent magnet. In contrast, antiferromagnetic materials have two or more sublattices, each with their own magnetization. Often, the magnetization in these two sublattices will be of equal magnitude yet anti-aligned, with a resultant magnetization of zero. Thus from a macroscopic perspective, AFM materials exhibit no magnetic properties. Many recent studies have suggested applications for AFM materials [71, 72, 73, 74, 75, 76, 77]. In chapter 6, it will be shown that, in principle, an ATJ can also be used to perform spectrum analysis.

A schematic of the physical structure of the theoretical ATJ is shown in Figure 2.14 [75]. It consists of a four-layer structure with a lower platinum (Pt) layer, a conducting AFM layer, a Magnesium Oxide (MgO) layer that serves as a tunneling barrier, and an upper platinum layer.

Oscillations arise in the following manner. First, the driving dc current I_{drive} flows through the bottom Pt layer, generating a transverse spin current due to the spin Hall effect [68]. This spin current penetrates the AFM/Pt interface and excites terahertz frequency (TF) rotation of the AFM sublattices and the AFM Neel vector[74]. The frequency of the TF oscillations is directly dependent on the magnitude of I_{drive}. This means that the operating frequency of the ATJ can be dynamically tuned by simply changing the DC bias I_{drive}.

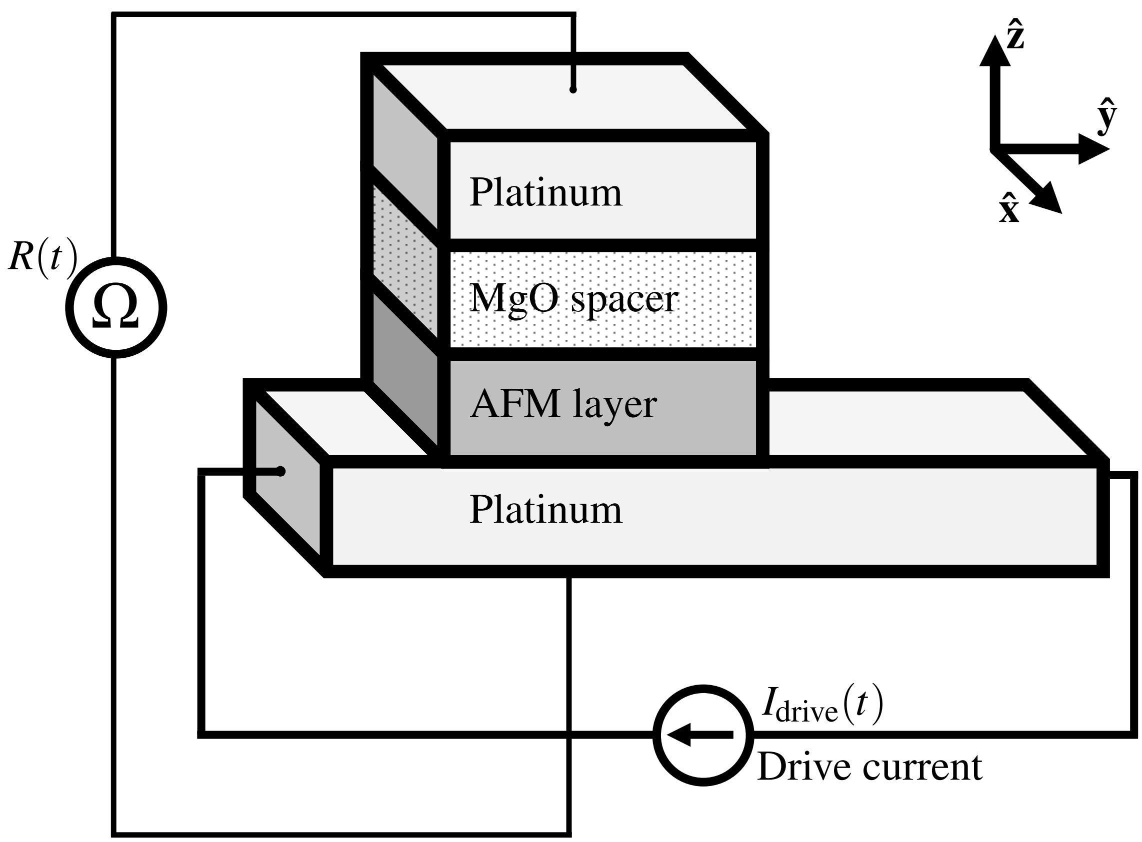

Figure 2.14: Schematic of antiferromagnetic tunnel junction. Driving current I_{drive} flowing in the bottom Pt layer of an ATJ generates the transverse spin current. The transverse spin current flows into the AFM layer and excites the THz frequency rotation of the magnetization of the AFM sublattices. The rotating AFM layer changes the junction resistance $R(t)$.

The oscillations can be extracted from the AFM layer by tunneling anisotropic magnetoresistance (TAMR) [69]. TAMR will be present when the inverse spin current in the AFM layer tunnels through the dielectric MgO layer barrier to the upper Pt layer [75]. Experimentally, TAMR electrical switching in an ATJ was observed to be dependent on the orientation of the AFM Neel vector [69, 70, 78]. Thus, when the AFM Neel vector rotates with a TF, the TAMR also oscillates with the same frequency. In this thesis, we will treat the TAMR as a macroscopic oscillating resistance, which we call $R(t)$, which has the same form as Equation (2.28). This resistance is

$$R(t) = R_{\text{atj}} - \Delta R_{\text{atj}} \cos\left(\rho t^2 + \omega_0 t + \psi_{\text{r}}\right), \tag{2.30}$$

where R_{atj} is the equilibrium resistance of the ATJ, and ΔR_{atj} is the magnitude of the variation of the junction ac resistance.

It must be noted that while an ATJ as described in [75] has not yet been fabricated, when developed it may have a transformative impact on modern electronics. Thus, it is worthwhile to consider the potential to perform spectrum analysis at THz frequencies with such a device.

CHAPTER THREE

METHODS

This chapter introduces the key numerical methods used to perform the research presented in this dissertation. All of the methods presented here involve numerical simulation. The numerical simulations were used in conjunction with analytical calculations, an example of which can be seen in appendix A. This chapter begins with physics simulations; specifically, simulation of magnetization precession in STNOs and ATJs. It then covers signal processing methods, including instantaneous frequency determination and the application of low pass and matched filters.

3.1 Simulation of STNO free layer magnetization

As discussed in section 2.3, when an STNO is driven by a bias current exceeding I_{th}, the magnetization $\mathbf{m}$ begins a stable precession about $\mathbf{B}_{\mathrm{eff}}$. This precession can lead to the sustained oscillations of the STNO resistance $r_{\mathrm{stno}}(I_{\mathrm{bias}},t)$. The frequency of precession $f_{\mathrm{stno}}(I_{\mathrm{bias}},t)$ depends on a number of factors, including the magnitude of the bias current. The nature of the relationship between I_{bias} and f_{stno} can be determined by simulating the magnetization dynamics of the MTJ free layer.

As stated in Equation (2.24), the magnetization dynamics in the MTJ free layer under the action of a DC current can be modeled using the LLGS equation. This is restated here for convenience:

$$\frac{\mathrm{d}\mathbf{m}}{\mathrm{d}t} - |\gamma|\mathbf{m}\times\mathbf{B}_{\mathrm{eff}} = \alpha_{\mathrm{G}}\mathbf{m}\times\frac{\mathrm{d}\mathbf{m}}{\mathrm{d}t} + \alpha_{\mathrm{J}} I_{\mathrm{bias}}\mathbf{m}\times[\mathbf{m}\times\mathbf{p}]. \tag{3.1}$$

In this equation, $\mathbf{m}$ is the normalized unit-length magnetization of the free layer in the macrospin approximation. The macrospin approximation assumes that the free layer has a spatially uniform distribution of magnetization, and thus can be reduced to a single vector. This approximation is reasonable for STNO free layers that are small enough to consist of

Table 3.1: STNO simulation parameters

Parameter	**Amount**	**Brief Description**
$\lvert\mathbf{B}_{\text{ext}}\rvert$	$1.5\,\text{T}$	External field magnitude
$\mu_0 M_s$	$0.8\,\text{T}$	Free layer saturation magnetization
γ	$-2\pi 28\,\text{GHz}/\text{T}$	Gyromagnetic ratio
α_{G}	0.01	Gilbert damping constant
$\hbar$	1.054571×10^{-34} Js	Reduced Planck constant
η_0	0.35	Spin polarization efficiency
μ_0	$4\pi \times 10^{-7}$ H/m	Free space permeability
e	1.602176×10^{-19} C	Fundamental electric charge
V	3×10^4 nm^3	Volume of the free layer
ΔR_{stno}	1 kΩ	Average STNO resistance
R_0	$1.5\,\text{k}\Omega$	Average resistance of the MTJ

a single magnetic domain. All simulations of STNOs in this dissertation use the macrospin approximation.

Below we will describe the parameters used to perform the simulation. Equation (3.1) uses the coordinate axis shown in Figure 2.8, with the cross section of the free layer in the $(\hat{\mathbf{x}}, \hat{\mathbf{y}})$ plane, and $\hat{\mathbf{z}}$ is orthogonal to the plane. The effective field is given by

$$\mathbf{B}_{\text{eff}} = \mathbf{B}_{\text{ext}}\hat{\mathbf{z}} - \mu_0 M_{\text{s}}(\mathbf{m} \cdot \hat{\mathbf{z}})\hat{\mathbf{z}}, \tag{3.2}$$

where $|\mathbf{B}_{\text{ext}}| = 1.5$ T is the magnitude of the external field that is applied perpendicular to the free layer plane, in the $\hat{\mathbf{z}}$ direction, and the free layer saturation magnetization is $\mu_0 M_s = 0.8$ T. The direction of the spin current polarization with $\beta = 30^\circ$ was chosen as $\mathbf{p} = \cos(\beta)\hat{\mathbf{x}} + \sin(\beta)\hat{\mathbf{z}}$.

Also in Equation (3.1), the Gilbert damping constant is $\alpha_{\text{G}} = 0.01$. The spin-torque coefficient α_{J} is defined as:

$$\alpha_{\text{J}} = \frac{|\gamma|\hbar\eta_0}{2\mu_0 M_{\text{s}} eV}. \tag{3.3}$$

Here $\gamma = -2\pi 28$ GHz/T is the gyromagnetic ratio, $\hbar = 1.054571 \times 10^{-34}$ Js is the reduced Planck constant, $\eta_0 = 0.35$ is the spin polarization efficiency, $\mu_0 = 4\pi \times 10^{-7}$ H/m is the free space permeability, $e = 1.602176 \times 10^{-19}$ C is the

```
Beff[t_] := bext - {0, 0, muoMs*(m[t].zhat)}; (* Effective field *)
tGilb[t_]:= alphaG*Cross[m[t], m'[t]]; (* Gilbert damping torque *)
tSlon[t_]:= gamma*alphaJ*biasCurrent[t]*Cross[m[t], Cross[m[t], p]]; (*Slonczewski torque*)
LLGS={m'[t]== -gamma*Cross[m[t], Beff[t]]+tGilb[t]+tSlon[t], m[0] == mag};(*LLGS*)
sol1 = NDSolve[LLGS, {m}, {t, 0, runTime}, MaxSteps -> Infinity];
```

Figure 3.1: Mathematica code used to simulate a STNO with LLGS using Equation (3.1). Approximations to decrease computation time can be found in [1].

fundamental electric charge, and $V = 3 \times 10^4$ nm^3 is the volume of the free layer. All parameters used for simulation are summarized in Table 3.1.

In this configuration, the threshold current of microwave signal generation in the STNO is $I_{\text{th}} = 2.32$ mA. The STNO magnetization can be found by solving Equation (3.1) numerically, allowing the computation of TMR resistance $r_{\text{stno}}(I_{\text{bias}}, t) = -\Delta R_{\text{stno}}(\mathbf{m} \cdot \mathbf{p})$, where $\Delta R_{\text{stno}} = 1$ kΩ is the amplitude of TMR oscillation. Thus, by simulating Equation (3.1) to find $\mathbf{m}$, the TMR resistance oscillation frequency can be determined.

All simulations were performed using Mathematica software[79]. Mathematica was chosen for two reasons. First of all, Mathematica runs effectively on a standard PC and produces results that are easy to manipulate. Secondly, Mathematica allows symbolic operations, thus easing code generation and troubleshooting. A sample of code used to simulate an STNO in the macrospin approximation can be found in Figure 3.1.

Simulation of an STNO occurs in two steps. First, Mathematica can solve Equation (3.1) numerically for $\mathbf{m}$ resulting in an interpolating function. This interpolating function can be sampled to create a list of discrete data for $\mathbf{m}$, which has data in 3 dimensions, $\hat{\mathbf{x}}$, $\hat{\mathbf{y}}$, and $\hat{\mathbf{z}}$. A scalar product $\mathbf{m} \cdot \mathbf{p}$ is then performed, and the results is multiplied by ΔR_{stno} to generate a one dimensional list for the TMR resistance $r_{\text{stno}}(I_{\text{bias}}, t)$. This list contains, in time, all the physical changes of the TMR in the MTJ, including oscillation frequency. Extracting this frequency as a function of time from a discrete list is not trivial, and is the subject of section 3.3.

3.2 Simulation of antiferromagnetic dynamics

The basics of an ATJ were introduced in section 2.4. There, it was stated that I_{drive} can excite a THz frequency rotation of the AFM sublattices, and that this rotation can be extracted from the ATJ with tunneling anisotropic magnetoresistance. The TAMR can thus be treated as a macroscopic oscillating resistance, which is denoted $R(t)$ with a frequency $f_{\mathrm{r}}(I_{\mathrm{bias}}, t)$. Thus an ATJ will be used as a tunable THz frequency signal generator.

Unfortunately, the ATJ described in literature has not yet been realized experimentally[75]. Therefore, to test the suitability of ATJ for spectrum analyzer applications, simulations can be performed that will relate I_{drive} and $R(t)$. This can be done by simulating the dynamics of the AFM layer. Specifically, it will assumed that the AFM material has two magnetic sublattices, with magnetizations $\mathbf{m}_1$ and $\mathbf{m}_2$. The dynamics of the $\mathbf{m}_1$ and $\mathbf{m}_2$ in an AFM material with two magnetic sublattices can be modeled with a pair of coupled Landau-Lifshitz-Gilbert-Slonczewski equations[74]

$$\frac{d\mathbf{m}_1}{dt} = \gamma \mathbf{B}_1 \times \mathbf{m}_1 + \alpha_{\mathrm{eff}} \left[\mathbf{m}_1 \times \frac{d\mathbf{m}_1}{dt} \right] + J\sigma [\mathbf{m}_1 \times [\mathbf{m}_1 \times \mathbf{p}]], \tag{3.4)a}$$

$$\frac{d\mathbf{m}_2}{dt} = \gamma \mathbf{B}_2 \times \mathbf{m}_2 + \alpha_{\mathrm{eff}} \left[\mathbf{m}_2 \times \frac{d\mathbf{m}_2}{dt} \right] + J\sigma [\mathbf{m}_2 \times [\mathbf{m}_2 \times \mathbf{p}]]. \tag{3.4)b}$$

Here $\mathbf{m}_1$ and $\mathbf{m}_2$ are the normalized unit-length magnetizations for the two sublattices in the AFM material in the macrospin approximation. The macrospin approximation was chosen for the same reason as described in section 3.1. In these equations, $\mathbf{B}_1$ and $\mathbf{B}_2$ are the effective magnetic fields acting on the sublattices $\mathbf{m}_1$ and $\mathbf{m}_2$.

$$\mathbf{B}_1 = -\tfrac{1}{2} B_{ex} \mathbf{m}_2 - B_h \mathbf{n}_h (\mathbf{n}_h \cdot \mathbf{m}_1) + B_e \mathbf{n}_e (\mathbf{n}_e \cdot \mathbf{m}_1), \tag{3.5)a}$$

$$\mathbf{B}_2 = -\tfrac{1}{2} B_{ex} \mathbf{m}_1 - B_h \mathbf{n}_h (\mathbf{n}_h \cdot \mathbf{m}_2) + B_e \mathbf{n}_e (\mathbf{n}_e \cdot \mathbf{m}_2). \tag{3.5)b}$$

As this study is focused on the qualitative behavior of AFM materials, we have adapted the simulation parameters used in [74] for an easy plane conducting AFM material. When performing simulations according to Equations (3.4) and (3.5), we chose physical parameters as follows. The gyromagnetic ratio is $\gamma = -2\pi 28$ GHz/T, α_{eff} =0.01 is the effective Gilbert damping parameter, and J is the electric current density in units of A/cm^2. The unit vector along the spin current polarization $\mathbf{p}$ is directed along $\hat{\mathbf{x}}$ according

Table 3.2: ATJ simulation parameters

Parameter	**Amount**	**Brief Description**
γ	$-2\pi \cdot 28$ GHz/T	Gyromagnetic ratio
α_{eff}	0.01	Effective Gilbert damping parameter
e	1.602×10^{-19} C	Fundamental electric charge
θ_{sh}	0.1	Spin hall angle of Pt
λ	7.3 nm	Spin diffusion length in Pt
ρ_0	$4.8 \times 10^{-7}\ \Omega\,\text{m}$	Electrical resistivity of Pt
d_{Pt}	20 nm	Thickness of the Pt layer
g_r	$7.0 \times 10^{18}\text{m}^{-2}$	Spin-mixing conductance at the Pt-AFM interface
M_s	$350\,\text{kA/m}$	Magnetic saturation of one AFM sublattice
d_{AFM}	1 nm	Thickness of the AFM layer
γB_{ex}	$2\pi 60$ THz	Exchange frequency
B_h	1 T	Hard-axis anisotropy field
B_e	3.6 mT	Easy axis anisotropy field

to the axes shown in Figure 2.14. The spin torque coefficient is given by

$$\sigma = \gamma e \frac{\theta_{sh} \lambda \rho_0 g_r}{M_s d_{\mathrm{AFM}}} \tanh \frac{d_{\mathrm{Pt}}}{2\lambda}\,, \tag{3.6}$$

where $e = 1.602 \times 10^{-19}$ C is the fundamental electric charge. For the lower Pt layer, $\theta_{sh} = 0.1$ is the spin Hall angle, $\lambda = 7.3$ nm is the spin diffusion length in Pt, and $\rho_0 = 4.8 \times 10^{-7}\ \Omega \cdot \mathrm{m}$ is the electrical resistivity[80]. The thickness of the Pt layer is assumed to be $d_{\mathrm{Pt}} = 20$ nm. The parameter $g_r = 7.0 \times 10^{18} \mathrm{m}^{-2}$ is used for the spin-mixing conductance at the Pt-AFM interface[81], $M_s = 350$ kA/m is the magnetic saturation of one AFM sublattice, $d_{\mathrm{AFM}} = 1$ nm is the thickness of the AFM layer. The exchange frequency is chosen to be $\omega_{ex} = \gamma H_{ex} = 2\pi \cdot 60$ THz, H_h is the hard-axis anisotropy field such that $\omega_h = \gamma H_h = 2\pi \cdot 30$ GHz, and H_e is the easy axis anisotropy field such that $\omega_e = \gamma H_e = 2\pi \cdot 0.1$ GHz.

All ATJ simulations were performed in mathematica for the same reasons described in section 3.1. Mathematica can solve Equations (3.4) and (3.5) numerically for $\mathbf{m}_1$ and $\mathbf{m}_2$ resulting in an interpolating function. This interpolating function can be sampled to create a list of discrete data for $\mathbf{m}_1$ and $\mathbf{m}_2$, both of which have data in 3 dimensions, $\hat{\mathbf{x}}$, $\hat{\mathbf{y}}$, and $\hat{\mathbf{z}}$. The frequency can be extracted from any component of $\mathbf{m}_1$ or $\mathbf{m}_2$. For example, $R(t) \propto \mathbf{m}_1 \cdot \hat{\mathbf{z}}$ was used in chapter 6 of this dissertation. This produces a discrete list of data that contains the frequency of TAMR oscillations of the ATJ. Thus, a method to determine the dynamics of TAMR oscillations as a function of time and I_{drive} has been described.

3.3 Instantaneous frequency

To understand the frequency behavior of STNOs and ATJs with a simulation, it is important to know the frequency of magnetization oscillations at any given time. As explained in the two previous sections, the simulation of an MTJ or ATJ results in a

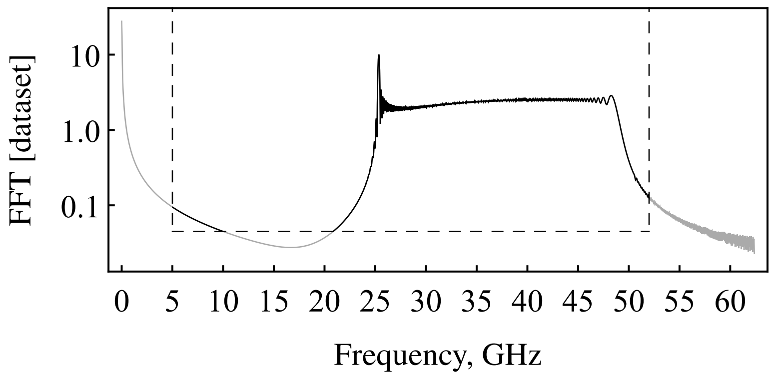

Figure 3.2: Thresholds for instantaneous frequency. This plot shows step 3 from section 3.3. The gray lines shows $X(\omega)$, the FFT of the input function. The dashed box shows the areas where the data of the FFT is retained; all areas outside this box are set to zero. The black curve shows $Y(\omega)$, the function that will be processed by an inverse FFT.

discrete lists of data containing the behavior of the magnetization precession. This magnetization behavior was then converted to lists of discrete data containing the TMR and TAMR information.

Thus, a method to evaluate the instantaneous frequency in simulation from a discrete list of data must be implemented. This was critical for this project, and was used

```
hankLow = samplingTime*hankleFilterLow;
hankHigh = samplingTime*hankleFilterHigh;
temp = Fourier[mmm];
temp[[1 ;; hankLow]] = 0;
temp[[hankHigh ;; Length[mmm] ]] = 0;
temp = temp*Unitize[Chop[Abs[temp], hankelThreshold]];
temp = InverseFourier[temp];

phaseWrpd = -Arg[temp]; (* \ Extract "wrapped" phase. This phase looks like a sawtooth *)
phase = phaseWrpd + Accumulate[ 2*Pi*Unitize[Threshold[Prepend[Differences[phaseWrpd], 0.], 1]]];
angFreq = Differences[phase]/ sampRate; (* Derivative of the phase *)
freq2 = angFreq/(2*Pi);
```

Figure 3.3: Mathematica code to determine the instantaneous frequency from discrete data.

to generate nearly every figure in chapters 4, 5, and 6. For example, Figure 2.9(b) required knowledge of the instantaneous frequency. The method presented here was chosen for its simplicity and speed of computation.

Analytically, the instantaneous phase of a continuous times series, $x(t)$, is given by $\theta = \cos^{-1}(\ x(t)\ )$, and the instantaneous frequency is the derivative of instantaneous phase, as $f = \frac{\mathrm{d}\theta}{\mathrm{d}t}$. Unfortunately, for a discrete time series, $x(n)$, where n is the index of the data in a discrete list, instantaneous frequency cannot be extracted by this simple analytical method. For more information about the distinction between continuous and discrete data, please see [82]. As an alternative, the instantaneous frequency of a discrete list of data can be extracted by using the following algorithm:

1. First, gather the list of discrete data which is under study. Here this discrete list of data is called $x(n)$. For an STNO based on an MTJ, this is simply $x(n) = \mathbf{m} \cdot \mathbf{p}$. For an ATJ, $x(n) = \mathbf{m}_1 \cdot \hat{\mathbf{z}}$ can be used.

2. Take the fast Fourier transform of $x(n)$. Specifically, $X(\omega) = \mathrm{FFT}[x(n)]$.

3. Convert $X(\omega)$ to analytic $Y(\omega)$, as shown in Figure 3.2. The is achieved by setting $X(\omega) = 0$ for all ω greater than an upper threshold, and for all ω lesser than a lower threshold. Also, set to zero all list values with an absolute value below a certain threshold. Thresholds are chosen such that only the frequencies of interest are retained. It is important to retain only a single side of the spectrum.

4. Inverse FFT of $Y(\omega)$, Notationally, this can be said as $y(n) = \mathrm{FFT}^{-1}[Y(\omega)]$.

5. Take the argument of $y(n)$ to get wrapped phase. The wrapped phase has a the appearance of a sawtooth.

6. The wrapped phase should then be unwrapped to get $\theta(n)$. To do this, simply remove the discontinuities with an accumulate function, as seen in line 10 of Figure 3.3.

7. The frequency is then found by taking the derivative of phase, which in a discrete list is simply the difference between each list value. Thus, $f(n) = \frac{\mathrm{d}\theta(n)}{\mathrm{d}n}$.

The code used to perform this algorithm can be seen in Figure 3.3.

3.4 Low pass filter

There are numerous methods to design low pass filters that can be applied to a discrete list of data. Fortunately, Mathematica includes a low pass filter function, “LowpassFilter[]”. This filter performed as well as was required for this dissertation. It is a FIR (finite impulse response) filter that uses, by default, a least squares filter kernal.

3.5 Matched filter

Implementing a matched filter in Mathematica is fairly simple. Firstly, both the signal and the matched filter are discretized data sets in the time domain. It is well known that convolution in the time domain is multiplication in the frequency domain[82]. Thus, to apply a matched filter with discrete data sets, they can be transformed via FFT into the frequency domain, multiplied together, then returned to the time domain via inverse fast Fourier transform. This method is not computationally intensive, and can be performed on a standard PC. Here we will describe the operation to implement Equation (2.16).

What follows below is an algorithm, as used in chapters 5 and 6, that applies a matched filter while limiting processing errors by padding lists with zeros.

1. To remove edge effects, zero padding is applied to $v_{\text{lpf}}(t)$. Lists of zeros of length ℓ should be added before and after the discrete data in $v_{\text{lpf}}(t)$, resulting in a zero padded list of length 3ℓ.

2. Create a discrete data list $h_{\text{match}}(t) = e^{-j\phi(\omega_{\text{m}},t)}$. The frequency ω_{m} should be chosen near the middle of Δf_{ch}. The length of this discrete data list should be 3ℓ. The time t of the list should be chosen such that it is symmetric about zero.

3. Perform FFT on $h_{\text{match}}(t)$ and the zero padded $v_{\text{lpf}}(t)$. Notationally, $H_{\text{match}}(\omega) = \text{FFT}[h_{\text{match}}(t)]$ and $S_{\text{lpf}}(\omega) = \text{FFT}[v_{\text{lpf}}(t)]$.

4. Multiply these two functions in the frequency domain $S_{\text{match}}(\omega) = H_{\text{match}}(\omega)S_{\text{lpf}}(\omega)$.

5. Perform the inverse FFT on $S_{\text{match}}(\omega)$. Notationally, $s_{\text{match}}(t) = \text{FFT}^{-1}[S_{\text{match}}(\omega)]$

6. Take the absolute value this function, as $|s_{\text{match}}(t)|$.

7. Rotate the discrete list $|s_{\text{match}}(t)|$ so that the corresponding peak aligns with t_{Δ}, and remove zero padding to obtain $v_{\text{out}}(t)$.

CHAPTER FOUR

STNO INJECTION LOCKING SPECTRUM ANALYSIS

There are two spectrum analysis regimes considered in this dissertation, an *injection locking* regime and a *mixing* regime. The injection locking regime, which is presented in this chapter, is a novel spectrum analysis algorithm. With this algorithm, spectrum analysis can be performed with a scan rate that is limited by the speed at which the STNO can injection lock to an external signal. The injection locking regime leverages the strong nonlinear injection locking behavior of an STNO. It functions by producing a dc voltage spike when the STNO frequency is injection locked to the external signal. The minimum detectable signal in this regime depends on how quickly the STNO can phase lock to the external signal, which depends inversely on scan rate and external signal amplitude. We found by simulation of a system based on realistic parameters that the minimum detectable signal is 1 pW at a scan rate of 1 MHz/ns. STNO spectrum analysis in the injection locking regime was published in [9], and presented at conferences [5, 11, 12].

A schematic of the proposed STNO spectrum analyzer is shown in Figure 4.1. This diagram follows a scheme that is analogous to Figure 2.2. Shown on the left of this figure are two inputs: a ramped bias current, and an external microwave signal to be analyzed. The bias current, $I_{\text{bias}}(t)$, is an electric dc current that begins at one level, then increases linearly as a "ramp" to another level. This bias current initiates the STNO free layer precession, as described in section 2.3, which can be viewed macroscopically an the oscillating resistance $r_{\text{stno}}(t, I_{\text{bias}})$ according to Equation (2.29). The frequency of this oscillating resistance depends on the amplitude of $I_{\text{bias}}(t)$. When $I_{\text{bias}}(t)$ increases linearly, the STNO frequency is linearly tuned through the scanning bandwidth.

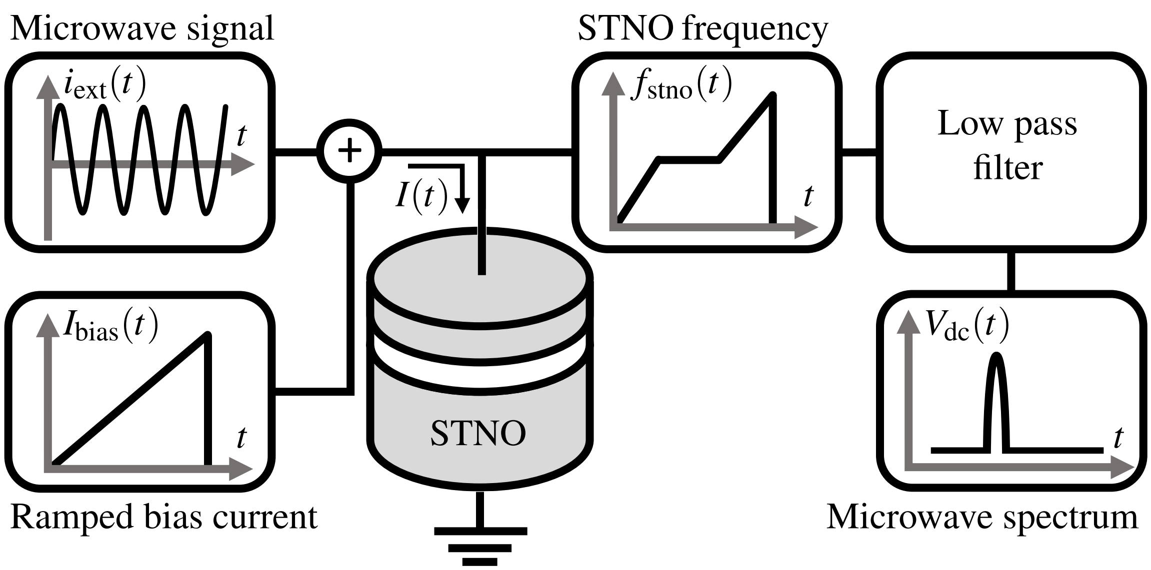

Figure 4.1: Schematic of STNO injection locking spectrum analyzer. The ramped bias current and microwave signal to be analyzed (on the left) are applied to the STNO (in the center). The STNO output (DC component of the STNO voltage) is digitally processed to produce the time-encoded microwave spectrum of the input signal (on the right).

As seen in Figure 4.1, the bias current $I_{\text{bias}}(t)$ is added to $i_{\text{ext}}(t)$, an external microwave signal to be analyzed, as $I(t) = I_{\text{bias}}(t) + i_{\text{ext}}(t)$, before being injected into the STNO. When the STNO frequency matches the frequency of the external signal $i_{\text{ext}}(t)$, the STNO may injection lock to the external signal, and thus have a frequency that is identical to that of the external signal. This external signal combines via Ohm's law with the oscillating resistance to produce a voltage $v_{\text{stno}}(t) = i_{\text{ext}}(t) r_{\text{stno}}(t)$. At times when the two signals have the same frequency, $v_{\text{stno}}(t)$ will have a dc voltage by the spin torque diode effect [83]. The STNO output voltage then undergoes signal processing, and the temporal position of the dc spike indicates the frequency of the external signal. Thus, the frequency spectrum of the input signal is encoded in the temporal profile of the output dc voltage.

It is important to emphasize that STNOs are well suited to this algorithm for three reasons, namely:

1. Fast linear scanning rate.
2. Wide phase locking bandwidth.
3. Wide tuning bandwidth.

Nevertheless, it must be noted that this algorithm is absolutely general and can be used for any tunable auto-oscillator.

This chapter begins by examining chirp generation with an STNO. Then, it will demonstrate by numerical simulation that the STNO frequency can phase lock to an external signal during chirp generation. After this, it is demonstrated numerically that a dc voltage is produced when the STNO is injection locked to the external signal, and this can be used to determine the spectrum of an external signal. Finally, the theoretical limits of this spectrum analysis method are presented with relation to the metrics defined in section 2.1.

4.1 STNO dynamic tuning

The frequency of STNO oscillations, $f_{\mathrm{stno}}(I_{\mathrm{bias}}(t),t)$, can be tuned by $I_{\mathrm{bias}}(t)$. Ideally, $f_{\mathrm{stno}}(I_{\mathrm{bias}}(t),t)$ could be tuned as fast as $I_{\mathrm{bias}}(t)$ can be ramped, approaching an infinitely fast tuning rate. Because STNOs are small, they have a small intrinsic capacitance and a small intrinsic inductance. This means that STNOs have a small time constant, and thus can be rapidly tuned. However, while STNOs can be tuned very quickly, there is a limit to how quickly they can be tuned. This will be investigated here.

The spectrum analysis methods presented here require the generation of a linear chirp according to Equation (2.5). Currently, no published studies address the maximum speed at which an STNO can generate a linear chirp. This section will present theory to describe the circumstances whereby an SNTO is capable of generating a linear chirp.

To demonstrate that the STNO frequency can be tuned in a linear manner, the STNO free layer magnetization $\mathbf{m}$ was simulated in the macrospin approximation with the

LLGS as described in the methods section 3.1. In this simulation, the free layer magnetization precession will be driven by a bias current, without an external microwave current; thus $I(t) = I_{\text{bias}}(t)$. When the amplitude of $I_{\text{bias}}(t)$ is large enough, the current-induced magnetization precession results in an oscillating dependence of the MTJ electrical resistance. The frequency of resistance oscillations can be determined from Equation (2.27).

Results of a simulation are shown in Figure 2.9. The bias current used for this simulation is shown in Figure 2.9(a). For the first 100 ns of simulation, the bias current is $I_{\text{bias}}(t) = 3.0$ mA. During this time, the STNO magnetization $\mathbf{m}$ begins to precess, until it reaches a stable precession frequency of $f_{\text{stno}}(t) \approx 25$ GHz. Then, the bias current increases linearly from 3.0 to 4.2 mA over a scanning period of $T = 500$ ns. This current increases at a rate of $dI_{\text{bias}}(t)/df = 0.0024$ mA/ns. After the scanning period has ended, the bias current is held constant at $I_{\text{bias}} = 4.2$ mA. The oscillation frequency of the simulated STNO free layer magnetization is shown by a solid line in Figure 2.9(b). The instantaneous frequency was extracted from the simulation as described in section 3.3. For this bias current ramp, $\mathbf{m}$ oscillates with a frequency that is a chirp that sweeps from 25 to 35 GHz, a scan rate of $\rho \approx 20$ MHz/ns. It is evident that the STNO free layer magnetization precession oscillation can tune the entire 10 GHz bandwidth in a linear manner.

The response of an STNO to a faster current ramp is shown in Figure 4.2. In this figure, the bias current increases linearly from 3.0 to 4.2 mA over a much shorter period, with $T = 4.0$ ns, as shown in Figure 4.2(a). This current ramps at a rate of $dI_{\text{bias}}(t)/dt = 0.3$ mA/ns. The STNO frequency is shown by a solid black line in Figure 4.2(b). For this bias current ramp, $\mathbf{m}$ oscillates with a frequency that increases in a non-linear manner between time 100 ns and $t_{\text{p}} \sim 101.75$ ns, then generates a linear chirp from t_{p} to 104.5 ns, when it again generates a nonlinear chirp until the generated frequency

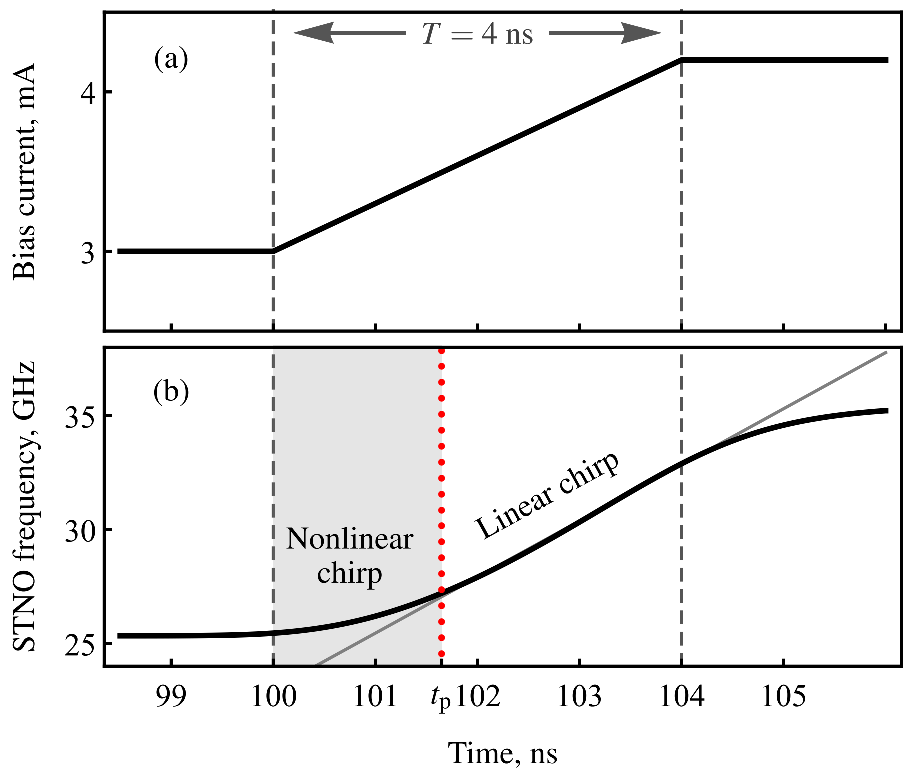

Figure 4.2: STNO frequency response to a 4.0 ns current ramp. (a) The bias current current, $I_{\text{bias}}(t)$. The current is 3 mA for the first 100 ns, then it increases linearly to 4.2 mA over 4 ns. (b) Black line shows the frequency of STNO free layer magnetization oscillations, $f_{\text{stno}}(t)$, in response to $I_{\text{bias}}(t)$. The frequency is stable at ≈ 25 GHz until 100 ns, then it increases to ≈ 35 GHz. The gray solid line is fitted to the portion of the chirp that is linear, with a frequency that increases at a rate $\rho = 2.4$ GHz/ns. The linear chirp begins at about $t_p \approx 1.75$ ns after the current ramp begins, and ends at $t = 104.5$ ns. The linear chirp has a scanning bandwidth of $\Delta f_{\text{ch}} \sim 7$ GHz.

approaches 35 GHz. Here we define t_{p} as the end of the initial transitory interval, or the time when the free layer magnetization precession frequency begins to increase linearly according to Equation (2.5). It is evident that for this simulation, the linear chirp begins at about 27 GHz, and ends at about 34 GHz, a scan rate of ~ 2.4 GHz/ns. The thin gray line shows a linear fit of the linear chirp portion of the STNO frequency curve.

Comparison of Figure 2.9 and Figure 4.2 demonstrates that slower chirps are linear, while faster chirps have both a nonlinear and a linear tuning region. It is important to establish for what scan rates a linear chirp can be generated, and for what scan rates it cannot. This is examined in Figure 4.3, which shows the response of STNO frequency to current ramps that vary from 0.2 to 1.0 mA/ns. In this figure, the STNO frequency response to a 1.0 mA/ns current ramp tunes linearly at a scanning rate of ≈ 10 GHz/ns. Therefore, it can be surmised that the maximum linear scan rate for an STNO as simulated is greater than 10 GHz/ns. It is evident that t_{p} is approximately unchanged with different ramp rates. This means the initial transitory interval is mostly independent of scan rate ρ. For the STNO parameters simulated here, $t_{\mathrm{p}} \approx 1.75$ ns, so the scanning period must be $T > 1.75$ ns. This means that t_{p} indirectly limits the scan rate for an STNO with finite scanning bandwidths.

It has been analytically shown that t_{p} depends on a physical characteristic of the SNTO, specifically $t_{\mathrm{p}} \approx 1/\Gamma_p$ where Γ_p is the damping rate for small power deviations in an STNO [5]. Thus, to improve the scan rate for an STNO for implementations in spectrum analysis, Γ_p should be increased during fabrication.

4.2 Dynamic tuning and injection locking

In the previous section, it was shown that the STNO frequency can be tuned by the bias current $I_{\mathrm{bias}}(t)$ such that it generates a linear chirp with a scan rate above 10 GHz/ns. If we use only the region where $f_{\mathrm{stno}}(t)$ is linear, the STNO free running frequency will be

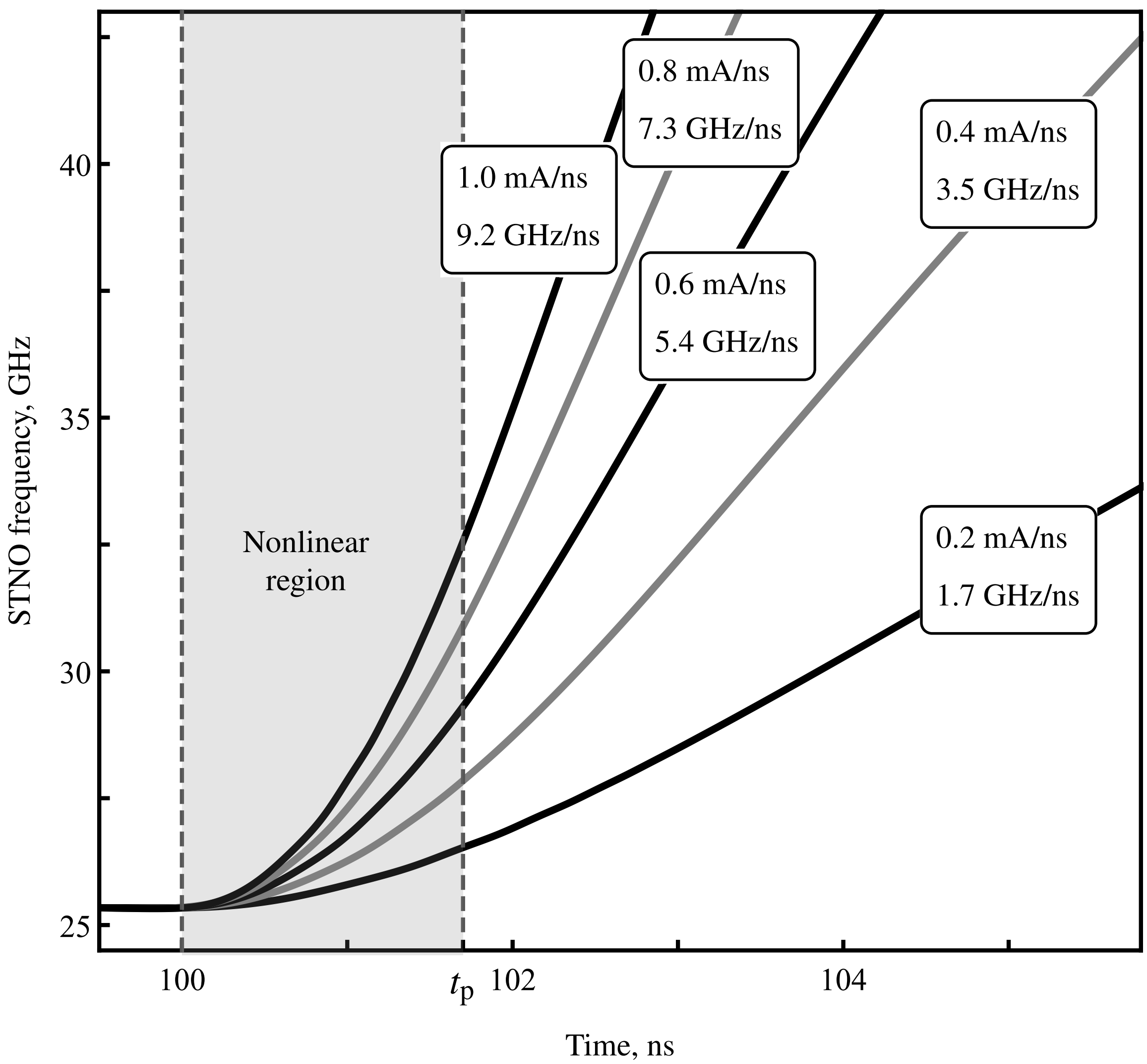

Figure 4.3: Boundary between linear and nonlinear regions for STNO generated chirps. The curves show the simulated response of the STNO to a variety of bias current ramps, with $dI_{\mathrm{bias}}(t)/dt$ varied from $0.2\,\mathrm{mA/ns}$ to $1.0\,\mathrm{mA/ns}$, as labeled on each line. The different curves begin to increase in a linear manner at about the same time, which is labeled with a dashed line at time t_{p}.

$f_{\text{stno}}(t) = f_{\text{r}}(t)$, which was introduced in Equation (2.5). The STNO frequency curves in Figure 2.9(b) and Figure 4.2(b) both represent the "free running" STNO frequency. Thus, when the STNO does not injection lock to an external microwave signal, $f_{\text{stno}}(t)$ and $f_{\text{r}}(t)$ coincide.

Injection locking was introduced in subsection 2.3.7. To demonstrate the injection locking phenomena in a dynamically tuned SNTO, simulations were run with $i_{\text{ext}}(t)$ injected into the STNO along with with $I_{\text{bias}}(t)$. Thus, the current injected into the STNO for this simulation is $I(t) = I_{\text{bias}}(t) + i_{\text{ext}}(t)$. For this simulation, the parameters for external signal in Equation (2.4) were $I_{\text{ext}} = 0.2$ mA and $f_{\text{ext}} = 30$ GHz. Results of the simulation are shown in Figure 4.4. As before, $I_{\text{bias}}(t) = 3.0$ mA for the first 100 ns, then increases to 4.2 mA over a period of $T = 500$ ns. The bias current is shown by a solid black line in Figure 4.4(a). The simulated STNO frequency in response to the bias current, and the external microwave current $i_{\text{ext}}(t)$, is shown by a solid black line in Figure 4.4(b). For the first 100 ns the STNO generates at $f_{\text{stno}}(t) \approx 25$ GHz until the bias ramp begins at 100 ns. Then, $f_{\text{stno}}(t)$ rises linearly with the scanning rate $\rho \approx 20$ MHz/ns until it nears f_{ext}, when the STNO injection locks to the external signal (see plateau in Figure 4.4(b)). As the bias current increases, the STNO exits the injection locking regime and its frequency resumes linear increase. For comparison, the free running STNO frequency is plotted in Figure 4.4(b) by a dashed gray line.

The STNO frequency in the presence of $i_{\text{ext}}(t)$ is different than the free running STNO in Figure 2.9. Specifically, when the STNO frequency is injection locked to $i_{\text{ext}}(t)$, the STNO generates at *exactly* the external frequency f_{ext}. The STNO frequency in the presence of an external signal during a current ramp is approximately:

$$f_{\text{stno}}(t) = \begin{cases} f_{\text{ext}} & \text{when injection locked,} \\ \\ f_{\text{r}}(t) & \text{otherwise.} \end{cases} \tag{4.1}$$

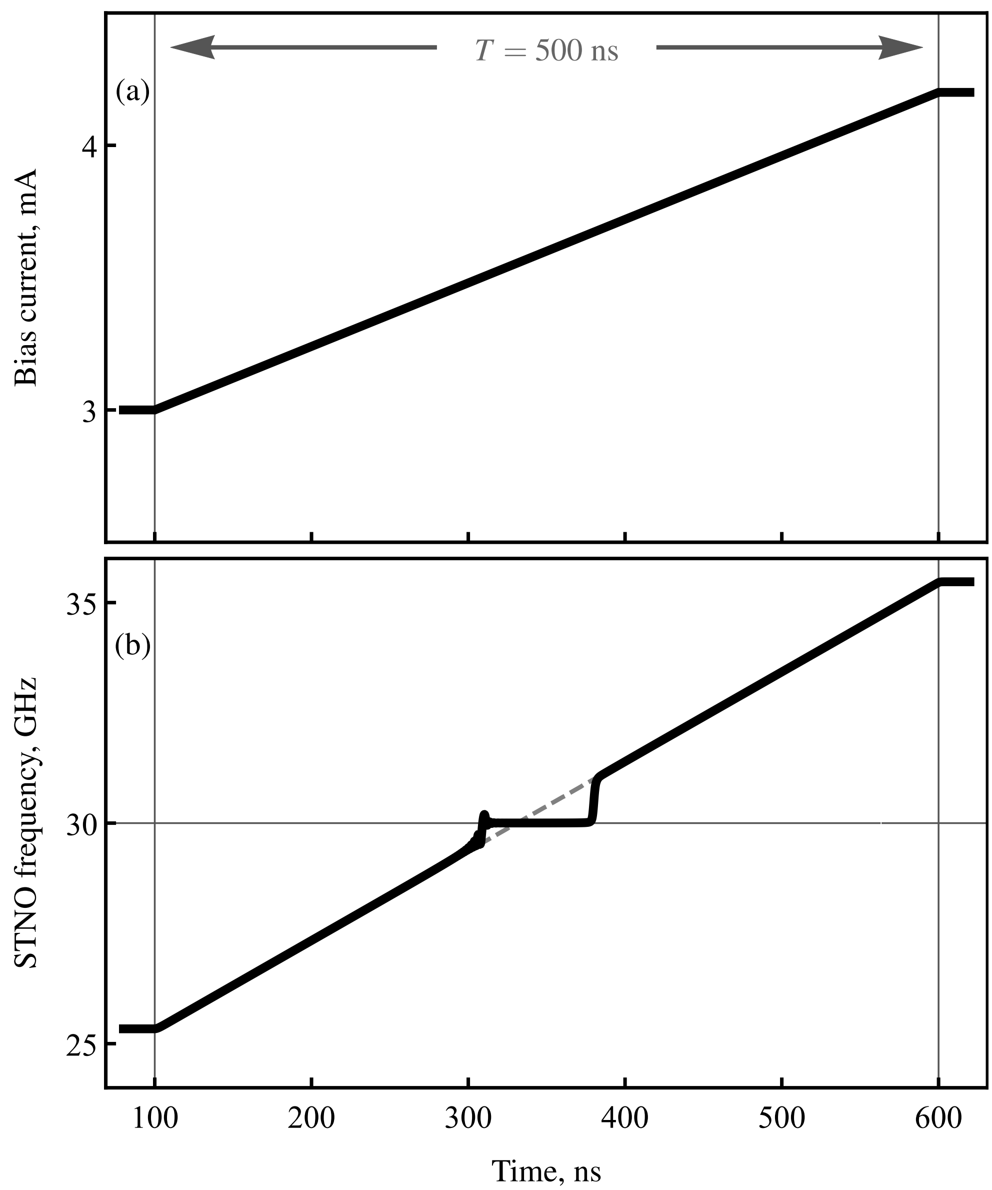

Figure 4.4: STNO injection locking demonstration with the bias current modulated by a microwave signal with $I_{\text{ext}} = 0.2$ mA, $f_{\text{ext}} = 30$ GHz. (a) In this simulations, the bias current $I_{\text{bias}}(t)$ is 3 mA until 100 ns, then it increases linearly to 4.2 mA over 500 ns. (b) The thick black line shows frequency of STNO free layer magnetization oscillations, $f_{\text{stno}}(t)$, in response to a ramped current and external microwave current. The frequency is stable at ≈ 25 GHz until 100 ns, then it increases to ≈ 35 GHz over a $T = 500$ ns period. Between 300 and 400 ns, the STNO frequency is injection locked to the external signal at f_{ext}. The gray dashed line shows the free running frequency of the STNO.

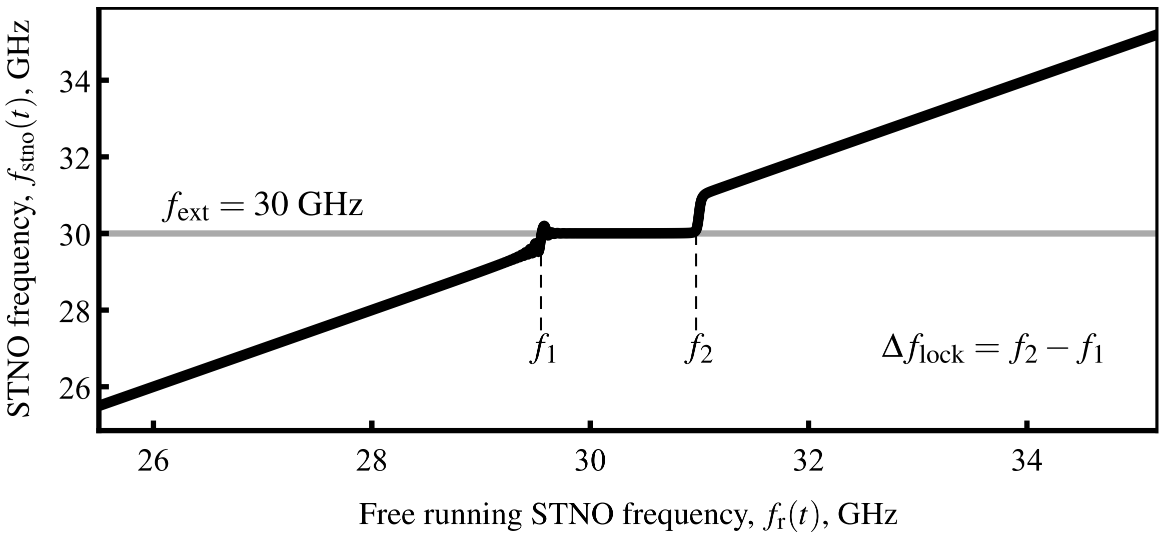

Figure 4.5: Simulated STNO phase locking bandwidth. The black line shows the frequency of forced STNO magnetization oscillations, $f_{\mathrm{stno}}(t)$, in response to the ramped bias current that is modulated by external microwave current with a $I_{\mathrm{ext}} = 0.2$ mA and $f_{\mathrm{ext}} = 30$ GHz. This plot differs from Figure 4.4 in that $f_{\mathrm{stno}}(t)$ is plotted as a function of STNO free running frequency $f_{\mathrm{r}}(t)$. Note that the $f_{\mathrm{stno}}(t)$ increases linearly until the free running frequency is f_1, when it has a plateau where $f_{\mathrm{stno}}(t) = f_{\mathrm{ext}}$ until f_2. After this, $f_{\mathrm{stno}}(t)$ resumes a linear increase. The phase locking bandwidth Δf_{lock} is given by $f_2 - f_1$

It is instructive to re-plot the STNO frequency $f_{\mathrm{stno}}(t)$ from Figure 4.4 as a function of free running frequency $f_{\mathrm{r}}(t)$. This is shown in Figure 4.5. In this plot,the STNO frequency increases linearly until it reaches about $f_1 \approx 29.5$ GHz. Then the STNO frequency jumps to 30 GHz, and remains at this frequency until $f_2 \approx 31$ GHz. After this, the STNO frequency once again increases in a linear manner. In Figure 4.5, the phase locking bandwidth is $\Delta f_{\mathrm{lock}} = f_2 - f_1 \approx 1.5$ GHz.

To study the dependence of phase locking bandwidth on I_{ext}, a series of simulations were performed. In these simulations, the amplitude of I_{ext} was varied while the scan rate was maintained at $\rho \approx 20$ MHz/ns. Results of these simulations are shown in Figure 4.6. In this figure, black dots show the simulated relationship between I_{ext} and Δf_{lock}, and the gray line shows a best fit line. It is evident that the phase locking bandwidth is $\Delta f_{\text{lock}} = \zeta(I_{\text{ext}} - I_{\text{lock}})$, where I_{lock} is an injection locking threshold current, and for this simulation $\zeta \approx 6$ MHz/μA. The physical origin of the injection locking threshold I_{lock} is clear: establishing phase-locking between an STNO and an external signal requires a certain time $\tau_{\text{lock}} = \alpha/I_{\text{ext}}$, where α is a constant that depends on the initial phase conditions of the system [40, 84]. If the STNO frequency is scanned over the locking interval faster than τ_{lock}, phase-locking becomes impossible.

It is important to note the in order for the STNO to injection lock to the external signal, it is necessary that $\tau_{\text{lock}} < \tau_{\text{pass}}$, where $\tau_{\text{pass}} = \Delta f_{\text{lock}}/\rho$ is the time required for the STNO to scan through Δf_{lock}. This implies that for injection locking there is a requirement that $I_{\text{ext}}^2 > (\alpha\rho)/\zeta$. This injection locking threshold current, which depends on ρ, is given by

$$I_{\text{lock}} = \sqrt{\frac{\alpha\rho}{\zeta}}. \tag{4.2}$$

Values for I_{lock} will be determined in the next sections.

4.3 Spectrum analysis with injection locking

When the external microwave current passes through the STNO, by Ohm's law it generates a voltage, $v_{\text{stno}}(t) = i_{\text{ext}}(t) r_{\text{stno}}(t)$. The result of this product will have a sum term $(f_{\text{r}}(t) + f_{\text{ext}})$ and a difference term $(f_{\text{r}}(t) - f_{\text{ext}})$. By filtering as in Equation (2.12), this voltage can be written as:

$$v_{\text{stno}}(t) = \begin{cases} -\frac{1}{2} I_{\text{ext}} \Delta R_{\text{stno}} \cos(\psi_{\text{lock}}) & \text{when injection locked} \quad (4.3)\text{a} \\ -\frac{1}{2} I_{\text{ext}} \Delta R_{\text{stno}} \cos\left(\pi\rho t^2 + \omega_\Delta t + \psi_{\text{lock}}\right) & \text{otherwise} \quad (4.3)\text{b} \end{cases}$$

Note that the injection locking phase shift ψ_{lock} is determined by two parameters, the internal properties of STNO and the frequency mismatch between the free-running STNO frequency and the signal frequency[85, 86, 1].

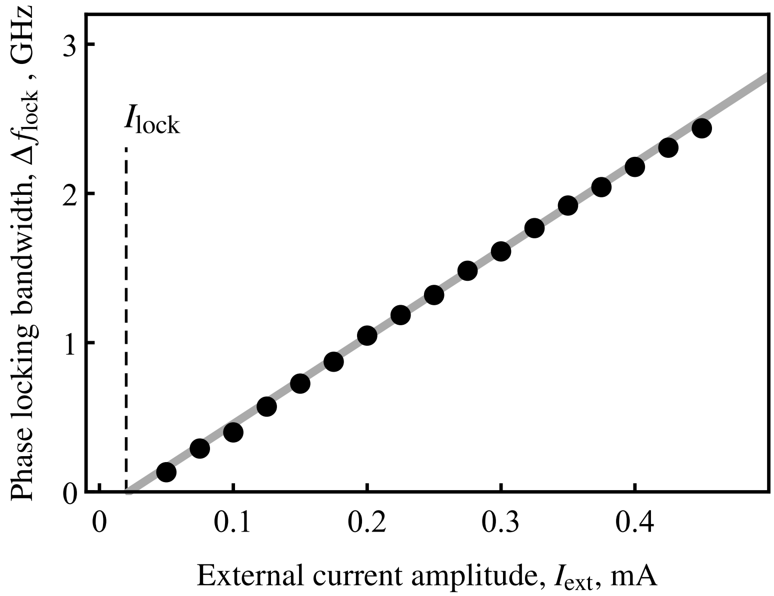

Figure 4.6: Phase locking bandwidth and microwave current amplitude. Black points show results obtained by simulation with $\rho \approx 20$ MHz/ns, and gray line shows a line of best fit.

The voltage in Equation (4.3)a is a dc voltage. The presence of a dc voltage thus indicates phase locking and the presence of an external signal at a particular frequency. If oscillating voltages are removed by a low pass filter and only the dc voltage is retained, Equation (4.3) will be

$$v_{\text{out}}(t) = \begin{cases} -\frac{1}{2} I_{\text{ext}} \Delta R_{\text{stno}} \cos(\psi_{\text{lock}}) & \text{when phase locked,} \quad \text{(4.4)a} \\ 0 & \text{otherwise.} \quad \text{(4.4)b} \end{cases}$$

The output dc voltage Equation (4.4) is generated only when the STNO is phase-locked to the external signal. If the free-running STNO frequency is sufficiently far from the microwave signal frequency, the STNO and external signal oscillations are uncorrelated, and the output voltage vanishes. The output dc voltage appears only at a moment of time when $f_{\text{stno}}(t) = f_{\text{ext}}$.

Note, that, in contrast with the usual "passive" spin-torque diode effect [83], the amplitude of the resistance oscillations ΔR_{stno} in the self-oscillating regime is determined mostly by the bias STNO current $I_{\text{bias}}(t)$ and is practically independent of a weak microwave signal I_{ext}. Therefore, the output dc voltage Equation (4.4) is proportional to the *amplitude* I_{ext} (rather than the power $\propto I_{\text{ext}}^2$) of the input signal. This property distinguishes the active STNO detector from conventional quadratic diode detectors and suggests that the STNO detector may have an increased responsivity to weak signals and lower MDS levels.

The validity of Equation (4.4), and the basic operation of the STNO spectrum analyzer will now be demonstrated by simulation. Figure 4.7(a) shows the $I_{\text{bias}}(t)$, and Figure 4.7(b) shows the STNO frequency $f_{\text{stno}}(t)$ in response to $I(t)$.

Figure 4.7(a) shows the output voltage $v_{\text{out}}(t)$, which was acquired as follows. In the first step, the raw output voltage of the STNO generating in the free-running regime (no input microwave current) is subtracted from the output voltage generated by a STNO in the presence of an external signal. Second, a low pass filter with cutoff frequency $\approx$15 GHz is applied. This filter removes the signals produced by the STNO in the 25 to 35 GHz frequency range without distorting low frequency signals. Finally, a low pass filter with a MHz range cutoff frequency of Δf_{vbw} is applied. As the characteristics of the output peak produced by the STNO detector changes with the scanning rate ρ, the video bandwidth (VBW) required for output also has to be adjusted. The empirically found optimal VBW follows the rule $\Delta f_{\text{vbw}} = \tau_c \rho$, where $\tau_c \approx 2.6$ ns for the chosen STNO parameters. In an experimental setup, the output voltage $v_{\text{out}}(t)$ after filtering will have a low frequency and, thus, can be processed further in the digital domain.

As shown in shown in Figure 4.7(c), the output voltage is non-zero only inside the injection locking interval and has a characteristic sawtooth shape. The specific form of the output dc peak is connected with the variation of the phase shift ψ between the STNO

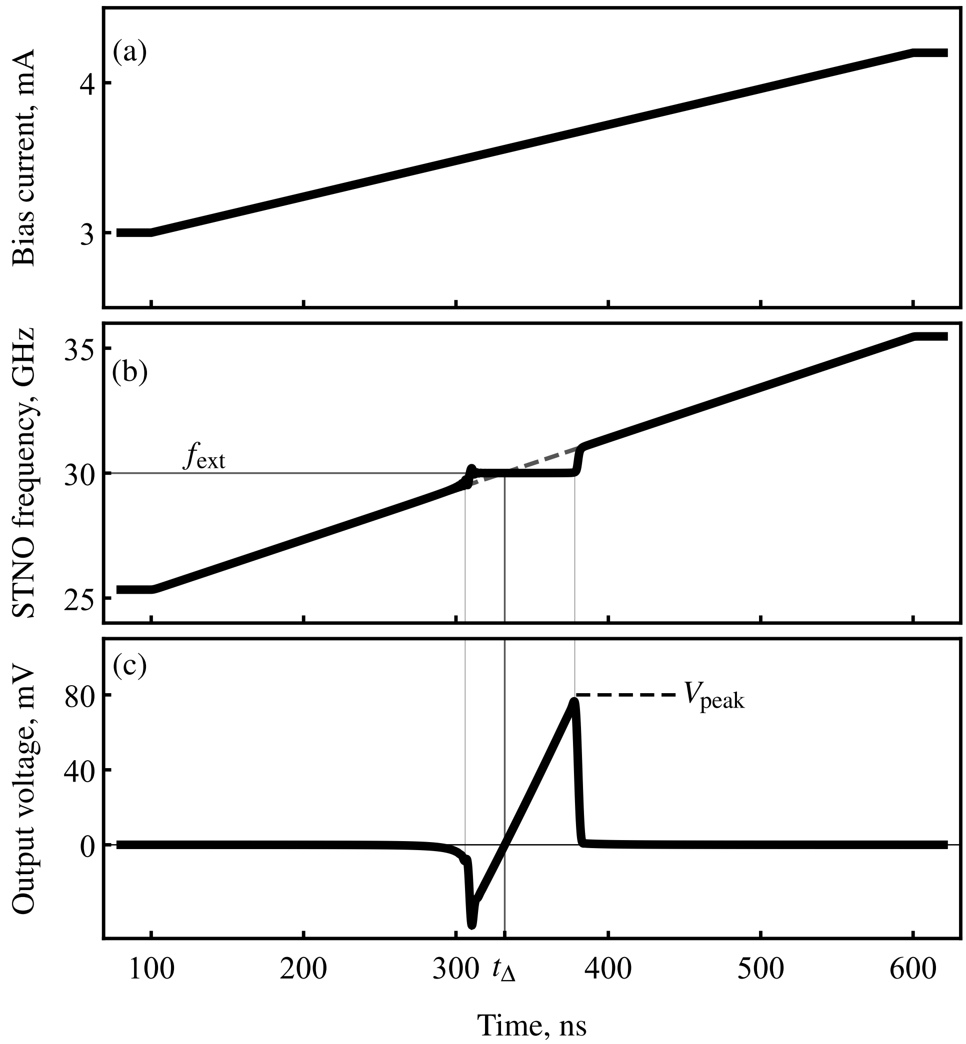

Figure 4.7: Basic operation of STNO injection locking spectrum analyzer. (a) The time profile of the ramped bias current $I_{bias}(t)$, with a 500 ns rise time. (b) The thick black line shows the instantaneous STNO frequency in response to the bias current and an external microwave signal $i_{ext}(t)$ with $f_{ext} = 30$ GHz and $I_{ext} = 0.2$ mA. Note the injection locking to the external signal, and the otherwise linear increase of the STNO frequency. The free-running STNO frequency in the injection locking interval is shown with a gray dashed line. The thin gray horizontal line shows the external signal frequency. The thin gray vertical line indicates the moment of exact resonance $f_{stno} = f_{ext}$. (c) The output dc voltage of the STNO. In the interval where the STNO is injection locked to the external signal, the STNO produces a sawtooth shaped pulse. Note that the pulse crosses the 0 V line at the point of exact resonance.

oscillations and the external signal (see Equation (4.4)). The phase shift ψ linearly increases with the STNO free-running frequency [1] and at exact resonance is equal to $\psi = \psi_0 \approx \pi/2$, the intrinsic phase shift of the STNO [85]. This is due to the strong nonlinearity of the STNO. The output voltage reaches maximum value V_{peak} at the right end of the synchronization interval, where $\psi \approx \pi$. Note, that, due to the large intrinsic phase shift of the STNO, when $\psi_0 \approx \pi/2$, the frequency of the external signal can be precisely determined.When additional simulations were run and the phase of the external signal was varied, we found for the system as simulated with $\rho \approx 20$ MHz/ns, had the frequency error of $\Delta f_{\text{error}} = 5.5$ kHz. With this error, the frequency accuracy is found to be 99.99998%.

If the STNO is modulated by multiple microwave signals, for example a signal with a spectrum as shown in Figure 4.8(a), the STNO will produce spikes of rectified voltage at corresponding frequencies as shown in Figure 4.8(b). In Figure 4.8(a), the external signal has frequencies at integral values between 25 and 35 GHz. Figure 4.8(b) shows output STNO voltage $v_{\text{out}}(t)$ mapped to the frequency domain $f_{\text{r}}(t)$. One can see that the STNO faithfully reproduces the complex input spectrum – the peak voltages V_{peak} are proportional to the amplitudes of the corresponding frequency components of the input signal, while the zero crossing of each sawtooth (indicated by red circles in Figure 4.8(b)) precisely matches each input frequency. There is a slight change in the relative amplitudes of V_{peak} related to the change of the amplitude of TMR oscillations ΔR_{stno} with bias current. This change, however, is rather weak and can be easily compensated during post signal processing.

It is demonstrated further in Figure 4.9 that the peak voltages given by V_{peak} are proportional to the amplitude of the input signal I_{ext}. In this plot, simulation results are shown with black dots, and the line of best fit is shown by a solid line. The slope of this

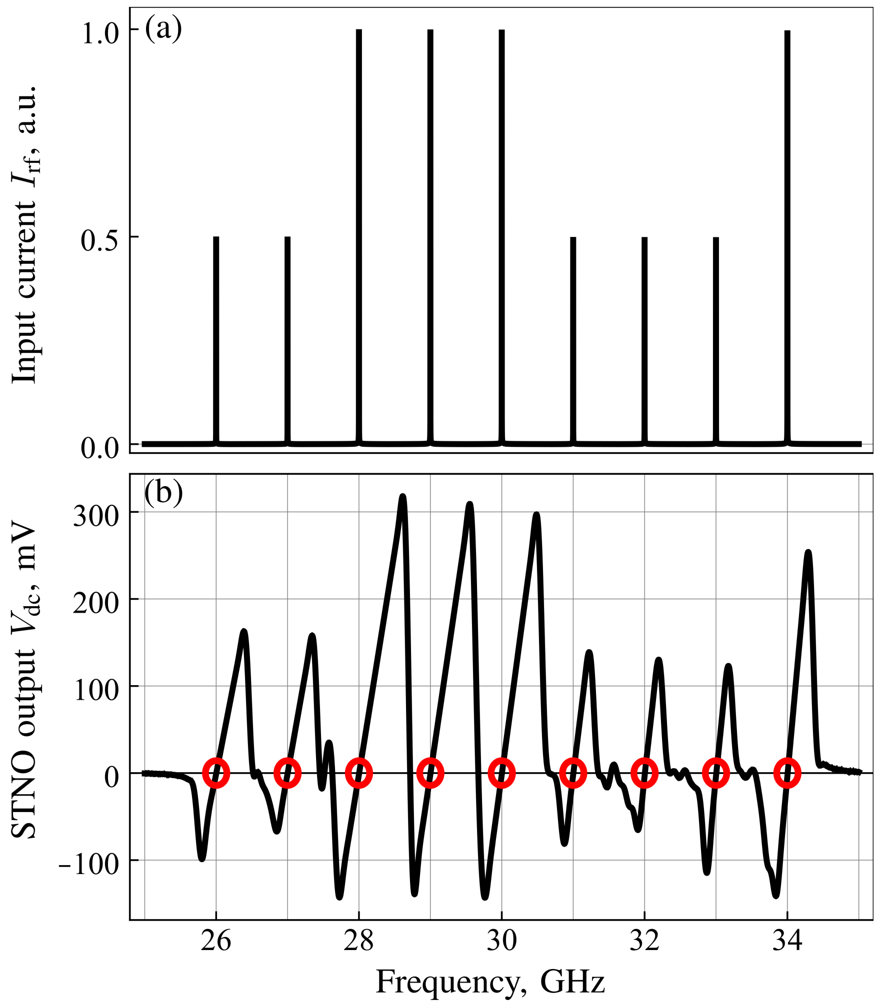

Figure 4.8: Example of injection locking spectrum analysis of an input signal with multiple frequencies. (a) Spectrum of input signal consisting of several monochromatic peaks with frequencies between 25 and 35 GHz. (b) Output dc voltage of the STNO spectrum analyzer. Note that the height of each sawtooth pulse is proportional to the amplitude of the corresponding input peak, while the zero crossings, labeled with red circles, coincide with high precision to the input frequencies.

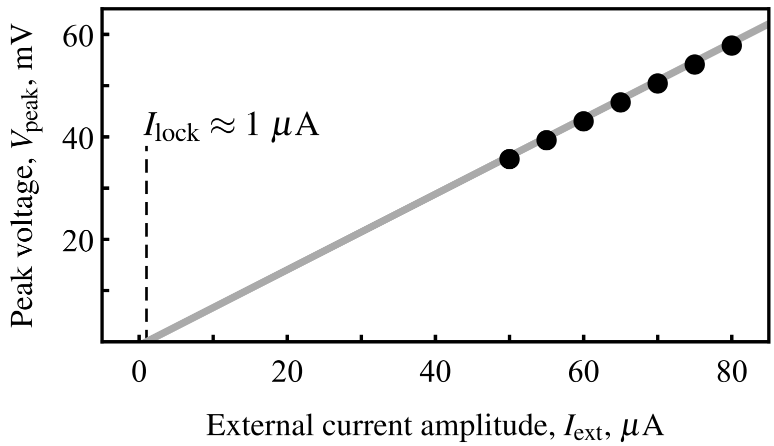

Figure 4.9: Dependence of peak voltage V_{peak} on external signal amplitude I_{ext}. Circles show simulation results, and solid gray line is a best fit. I_{lock} for this scan rate is $\approx 1\ \mu$A. $\rho = 20$ MHz/ns.

line is the responsivity G at this scan rate, and the x-intercept at I_{lock} represents the minimum external signal amplitude I_{ext} required to induce phase locking.

Our simulations have shown that at small values of I_{ext}, noticeable distortions of the output sawtooth-like STNO peak appear. In this regime the generated dc pulse becomes dependent on the initial phase of STNO oscillations and the peak voltage V_{peak} reduces. As stated earlier, reliable detection of microwave signals is impossible if $I_{\text{ext}} < I_{\text{lock}}$, where $I_{\text{lock}} = I_{\text{lock}}(\rho)$ is an injection locking threshold, which depends on the scanning rate ρ. In the region $I_{\text{ext}} > I_{\text{lock}}$ the peak voltage V_{peak} is accurately described by the simple relation

$$V_{\text{peak}} = G(I_{\text{ext}} - I_{\text{lock}}), \tag{4.5}$$

where $G = \mathrm{d}V_{\text{peak}}/\mathrm{d}I_{\text{ext}}$ is the responsivity of the STNO detector. The physical origin of the injection locking threshold I_{lock} is clear: establishing phase-locking between an STNO and an external signal requires a certain time τ_{lock}, which is inversely proportional to the signal amplitude I_{ext} [40, 84] and, if the STNO frequency is scanned over the locking

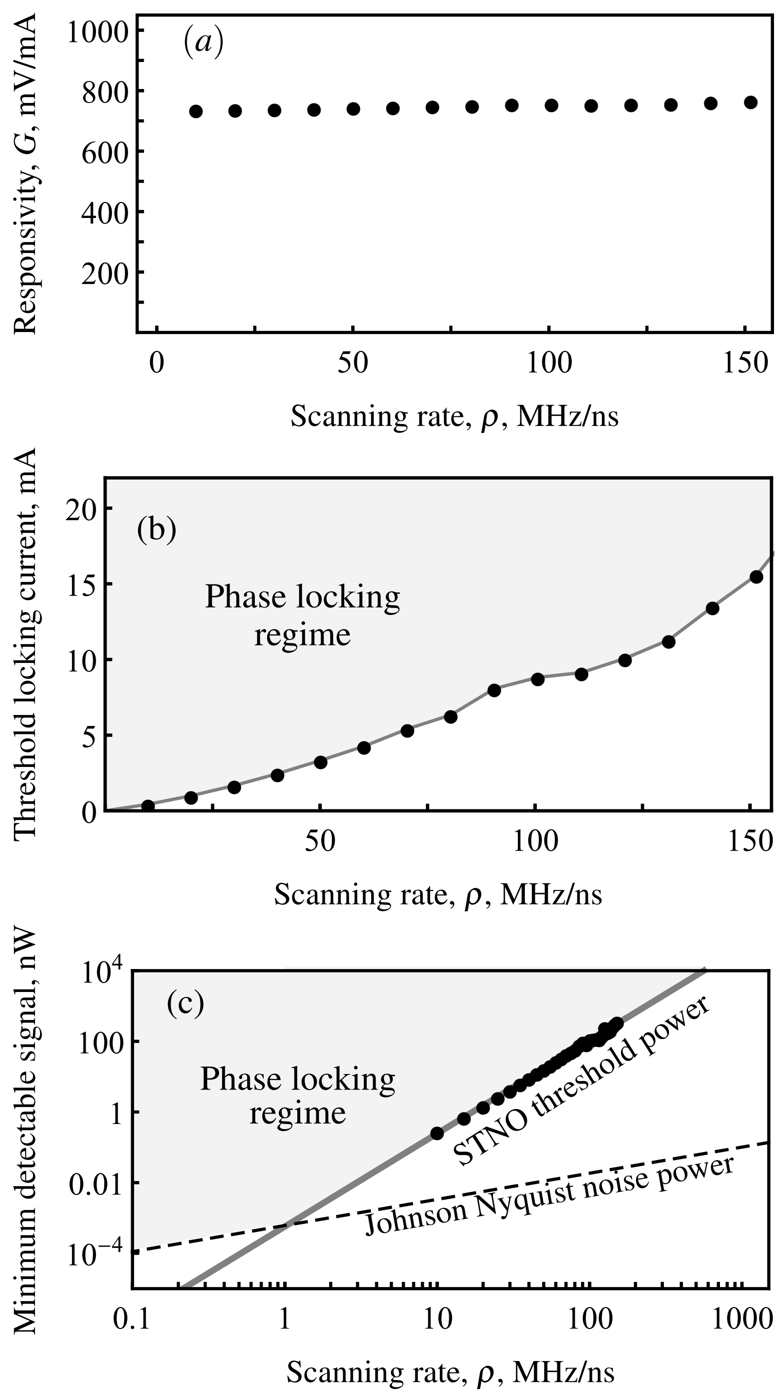

Figure 4.10: Dependence of main characteristics of injection locking STNO spectrum analyzer on scan rate ρ. (a) Responsivity G (b) The threshold phase-locking current I_{lock}. (c) Minimum detectable signal.

interval faster than τ_{lock}, phase-locking becomes impossible. It is interesting to note that the influence of frequency ramp on injection locking of an oscillator, described by Equation (4.5), is analogous to the influence of thermal noise, where the apparent locking threshold has been observed experimentally [87].

Figure 4.10(a) shows the dependence of the responsivity G and the threshold current I_{lock} on the scanning rate ρ for a signal frequency of $f_{\text{ext}} = 30$ GHz. The sensitivity remains practically constant, $G \approx 750$ mV/mA, for a wide range of scanning rates. In contrast, the threshold current I_{lock} increases approximately linearly with ρ, as shown in Figure 4.10(b), and has a value $I_{\text{lock}} \approx 10\ \mu$A at $\rho = 100$ MHz/ns. The increase of I_{lock} is the main factor limiting the practical scanning rate of a STNO spectrum analyzer using the injection locking algorithm.

The MDS, P_{mds}, of the STNO spectrum analyzer can be estimated as the input signal power, for which the output voltage Equation (4.5) becomes equal to the thermal Johnson-Nyquist voltage in the bandwidth of low-pass filter Δf_{vbw}. The dependence of P_{mds} on the scanning rate ρ for $f_{\text{ext}} = 30$ GHz is shown in Figure 4.10(c) by solid circles. In the range of simulated scanning rates, the MDS is dominated by the threshold current I_{lock} and can be estimated simply as $P_{\text{mds}} \approx R_0 I_{\text{lock}}^2/2$. The influence of Johnson-Nyquist (JN) noise (see dashed line in Figure 4.10(c)), however, becomes more important with the reduction of the scanning rate and at $\rho \approx 1$ MHz/ns the two contributions become approximately equal. At these rates the MDS is about 1 pW and, thus, the STNO spectrum analyzer can function to detect low power signals and be used as an ultra-sensitive microwave signal detector. In this theoretical work, we have assumed perfect impedance matching. However, in an implemented experiment, good impedance matching over a 10 GHz bandwidth is difficult, and may cause an increased MDS at unmatched frequencies.

4.4 Performance evaluation

This section will summarize the findings of this chapter by directly discussing the performance metrics introduced in section 2.1. As most of the metrics are interdependent, these metrics will be explained together. In the absence of an analytical model, metrics for one set of numerical results will be stated.

Firstly, the scanning bandwidth Δf_{ch} of this spectrum analyzer is essentially the same as the tunable bandwidth of the STNO. For the STNO as simulated here, this can be as wide as 25 GHz for systems that are tuned by a changing bias current. In practice, fabrication defects and inhomogeneities will lead to smaller scanning bandwidths, with the maximum experimentally observed tunable bandwidth approximately 10 GHz[2]. In our simulations, we assumed a scanning bandwidth of $\Delta f_{\mathrm{ch}} = 10$ GHz, although much wider bandwidths are likely possible.

For the chirp to be linear, the period of the chirp T must be greater than the nonlinear transitory interval, as $T > t_{\mathrm{p}}$. For scan rates where $T \gg t_{\mathrm{p}}$, the nonlinear transitory time span can be neglected and the practical scan rate will by $\rho = \Delta f_{\mathrm{ch}}/T$. In our simulations, $t_{\mathrm{p}} \approx 1.5$ ns, so one can assume that the chirp will be linear for the entire scanning bandwidth when $T > 20$ ns, or $\rho < 0.5$ GHz/ns. In comparison with many technologies, this scan rate is quite fast. However, we showed that STNOs can generate linear chirps even faster. When T is on the order of t_{p}, the scanning bandwidth will decrease, and the timespan during scanning will also vary. For the STNO as simulated here, the maximum scan rate is effectively $\rho \approx 2$ GHz/ns.

With this spectrum analysis system, the output voltage increases linearly with external current amplitude. Thus, the responsivity of system was constant, and for the system simulated here, the responsivity was $G \approx 750$ mV/mA. The responsivity was independent of scan rate.

The resolution bandwidth RBW and the minimum detectable signal depend on the scan rate. For this spectrum analysis system to detect an external signal, it must injection lock to the external signal. As the STNO is being dynamically tuned, it requires a finite time τ_{lock} to injection lock to the external signal, which is inversely proportional to the signal amplitude, as $\tau_{\text{lock}} \propto 1/I_{\text{ext}}$. This requires the current to be above the phase locking threshold I_{lock}, and thus to have a certain minimum power $P_{\text{mds}} \approx R_0 I_{\text{lock}}^2/2$. This defines the MDS. For the system simulated here, the minimum current required to phase lock was $I_{\text{lock}} = 1\ \mu$A, and thus a MDS of $P_{\text{mds}} = 2$ nW. For the system as simulated, scan rates below $\rho = 1$ MHz/ns, the minimum signal required is determined by the Johnson Nyquist noise. The MDS for $\rho = 1$ MHz/ns, was found by simulation to be $P_{\text{mds}} \approx 1$ pW.

The resolution bandwidth of this system is approximately equal to the phase locking bandwidth, RBW$= \Delta f_{\text{lock}}$. The STNO must injection lock to the external signal for a non-zero RBW, which introduced a dependence on scan rate, thus RBW $\to$ RBW(ρ). For the system simulated with $\rho \approx 20$ MHz/ns, RBW depended linearly on the external current amplitude at approximately 6 MHz/μA, as shown in Figure 4.6. The results in a RBW on the order of 100 MHz near the detection threshold. Note that for a signal where $I_{\text{ext}} > 1.66$ mA, the RBW may encompass the entire scanning bandwidth.

The maximum input power can depend on two characteristics. Firstly, both MTJs and spin valves will breakdown when traversed by a powerful current. Spin valves practically will breakdown at a much higher power due to their all metal composition. However, for external signals with larger powers, the RBW may increase to encompass the entire scanning bandwidth. While still functional for detecting a single external signal, this may limit the utility of the system. For the system as simulated, the entire scanning bandwidth was consumed when the external current was $I_{\text{ext}} > 1.66$ mA, which is a power of $P_{\text{max}} = 3.4$ mW. Thus with $P_{\text{mds}} = 2$ nW and $P_{\text{max}} = 3.4$ mW, the dynamic range is about 75 dB.

Lastly, the frequency accuracy is determined by how close the zero crossing in the saw-tooth shaped dc voltages. For the system as simulated, the frequency error was $\Delta f_{\text{error}} = 5.5$ kHz and thus the frequency accuracy was 99.99998%.

4.5 Conclusion

A novel type of ultrafast spectrum analyzer is proposed and investigated theoretically through numerical simulation. The analyzer is based on injection locking of an STNO driven by a ramped bias current. The spectrum analyzer faithfully reproduced the spectra of complex incident signals and can have an operational bandwidth of 10 GHz and frequency scanning rate exceeding 100 MHz/ns. The minimum detectable power of the analyzer decreases with the decrease of the scanning rate, and is about 1 pW at a scanning rate of 1 MHz/ns.

CHAPTER FIVE

SPECTRUM ANALYSIS WITH A STNO MIXER

This chapter proposes to use a STNO as a simple mixer and chirped signal generator. It will be shown, both theoretically and experimentally, that fast broadband spectrum analysis can be performed with a rapidly tuned STNO based on a magnetic tunnel junction (MTJ). This system will have a frequency resolution at the theoretical limit defined by the bandwidth theorem, while remaining sensitive to signals with power levels below the Johnson-Nyquist thermal noise floor.

The configuration of a STNO mixer spectrum analyzer is introduced by a block diagram in Figure 5.1, which is similar to that which was introduced in subsection 2.2.1 and subsection 2.2.2. In this diagram, a ramped bias dc current $I_{\mathrm{bias}}(t)$ drives the STNO (outlined by a dashed line) which generates a signal $r_{\mathrm{stno}}(I_{\mathrm{bias}},t)$ with frequency $f_{\mathrm{r}}(t)$ that increases linearly with time. The spectrum of the external signal $i_{\mathrm{ext}}(t)$ is then analyzed with a matched filter, as described in subsection 2.2.2. Overall, the method of operation of the proposed spectrum analyzer is similar to a traditional swept-tuned spectrum analyzer, with the exception that frequency tuning and mixing is performed entirely by a single STNO.

The method presented in this chapter differs from the previous chapter, which performed spectrum analysis using the injection locking properties of an STNO[9]. The previous chapter showed that a minimum time and energy was required for an STNO to injection lock to an external signal, thus precluding the use at faster scan rates for low power signals. In contrast, for an STNO treated as a tunable oscillating resistor, as in the present chapter, *no minimum threshold energy is required* for the signal detection, and,

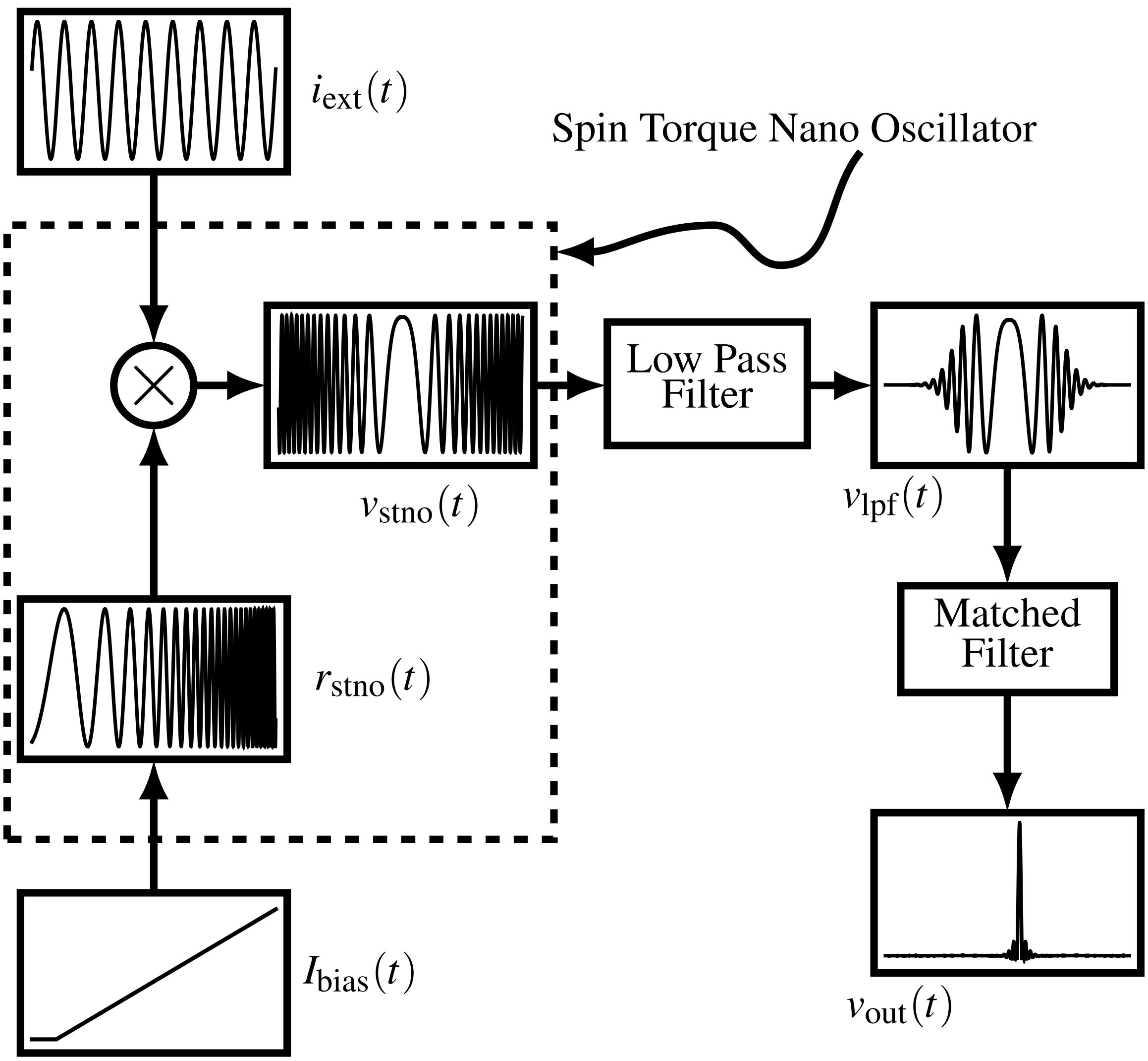

Figure 5.1: Block diagram of a STNO mixing spectrum analyzer. The MTJ based STNO tunneling magneto-resistance $r_{\text{stno}}(t)$, which is driven by ramped current $I_{\text{bias}}(t)$, is multiplied by external microwave current $i_{\text{ext}}(T)$ to produce STNO voltage $v_{\text{stno}}(t)$. After passing through a low pass filter and a matched filter, a spectrum $v_{\text{out}}(t)$ is produced.

thus, only the noise floor determines the minimum detectable signal regardless of the scan rate.

This relatively simple scheme has several advantages, including: *i*) wide scanning bandwidth, *ii*) high scanning speed, *iii*) high sensitivity to low power signals, *iv*) invariance to phase shifts, and *v*) resolution bandwidth at the theoretical limit. Each of these properties will be demonstrated by numerical simulation.

This chapter will begin by presenting theory and numerical simulation of a STNO mixer spectrum analysis. After this, experimental results will be presented. The results in this chapter are a combination of two publications. The theoretical results were from [8], and the experimental results are from [18]. The experiments were performed by Artem Litvinenko, and the research group of Ursula Ebels from the French Alternative Energies and Atomic Energy Commission (CEA) and SPINTEC in Grenoble, France. They used a STNO that was fabricated by Alex Jenkins and Ricardo Ferreira from International Iberian Nanotechnology Laboratory (INL). Additionally, these results were presented at [13].

5.1 Numerical simulation and theoretical analysis

In this section, we will report on the simulation of an STNO generating a chirp and acting as a signal mixer. The simulation, as in chapters 3 and 4, will model the STNO free layer with the LLGS in the macrospin approximation. All parameters for the simulation were chosen to have typical values, as were used in previous publications[9, 40]. They are detailed in Table 3.1. All simulations in this section were performed without noise, and with an external signal of power ≈ 0.05 pW ($I_{\text{ext}} = 10$ nA).

The first simulation results are shown in Figure 5.2. In this simulation, the bias current was held constant with $I_{\text{bias}}(t) = 3.0$ mA for the first 40 ns of simulation, allowing $r_{\text{stno}}(I_{\text{bias}}, t)$ to oscillate steadily at a frequency of $f_{\text{stno}}(I_{\text{bias}}, t) = 25.4$ GHz. The frequency of $r_{\text{stno}}(I_{\text{bias}}, t)$, as acquired by simulation, are shown by a gray dashed line in

Figure 5.2(a). After 40 ns, $I_{\text{bias}}(t)$ was increased with a slope of ≈ 1.2 mA/ns. This current increase caused the STNO oscillation frequency to increase at the constant scan rate of $\rho = 1$ GHz/ns. This is equivalent to Equation (2.5). The thick black line in Figure 5.2(a) shows the $T = 10$ ns interval where spectrum analysis was performed, and $f_{\text{stno}}(t)$ scans between 26 and 36 GHz.

The goal of the spectrum analysis is, of course, to determine the frequency of all the signals present in this 10 GHz frequency span. Note that the frequency scan in the interval of 10 GHz was performed in 10 ns, thus demonstrating a high scanning speed and a wide frequency bandwidth.

The results of these two simulations are shown in Figure 5.2(b) and Figure 5.2(c), with a thin gray line representing $v_{\text{lpf}}(t)$ with $f_{\text{c}} = 15$ GHz. It is important to note, that experimentally the phase difference ψ cannot be controlled, so this numerical simulation was performed with two representative phases, $\psi = 0$ and $\psi = 0.15\pi$. The line in both Figure 5.2(b) and Figure 5.2(c) shows that the frequency is at a minimum near $t_0 = 46$ ns. This low frequency voltage coincides in time with the moment when the frequencies of $r_{\text{stno}}(I_{\text{bias}}, t)$ and $i_{\text{ext}}(t)$ are the same. This is emphasized by the thick red and blue lines, which show $v_{\text{lpf}}(t)$ with low pass filter cutoff frequency $f_{\text{c}} = 2$ GHz. Both of these lines show increased amplitude when the frequencies of the two signals are the same, and, indeed, the red line in Figure 5.2(b) can be used to precisely determine the time when the two frequencies are equal. However, this is not possible when $\psi = 0.15\pi$, as the dual peaks seen in the blue line of Figure 5.2(c) could be produced instead by two external signals.

There are several spectrum analysis algorithms that could be used to eliminate the impact of ψ, as was discussed in section 2.2. Here, we will use a matched filter to limit the influence of ψ and vastly improve the SNR. Figure 5.2(d) shows $v_{\text{out}}(t)$ for signals with phases $\psi = 0$ and $\psi = 0.15\pi$. It is evident that both curves show a sharp peak at

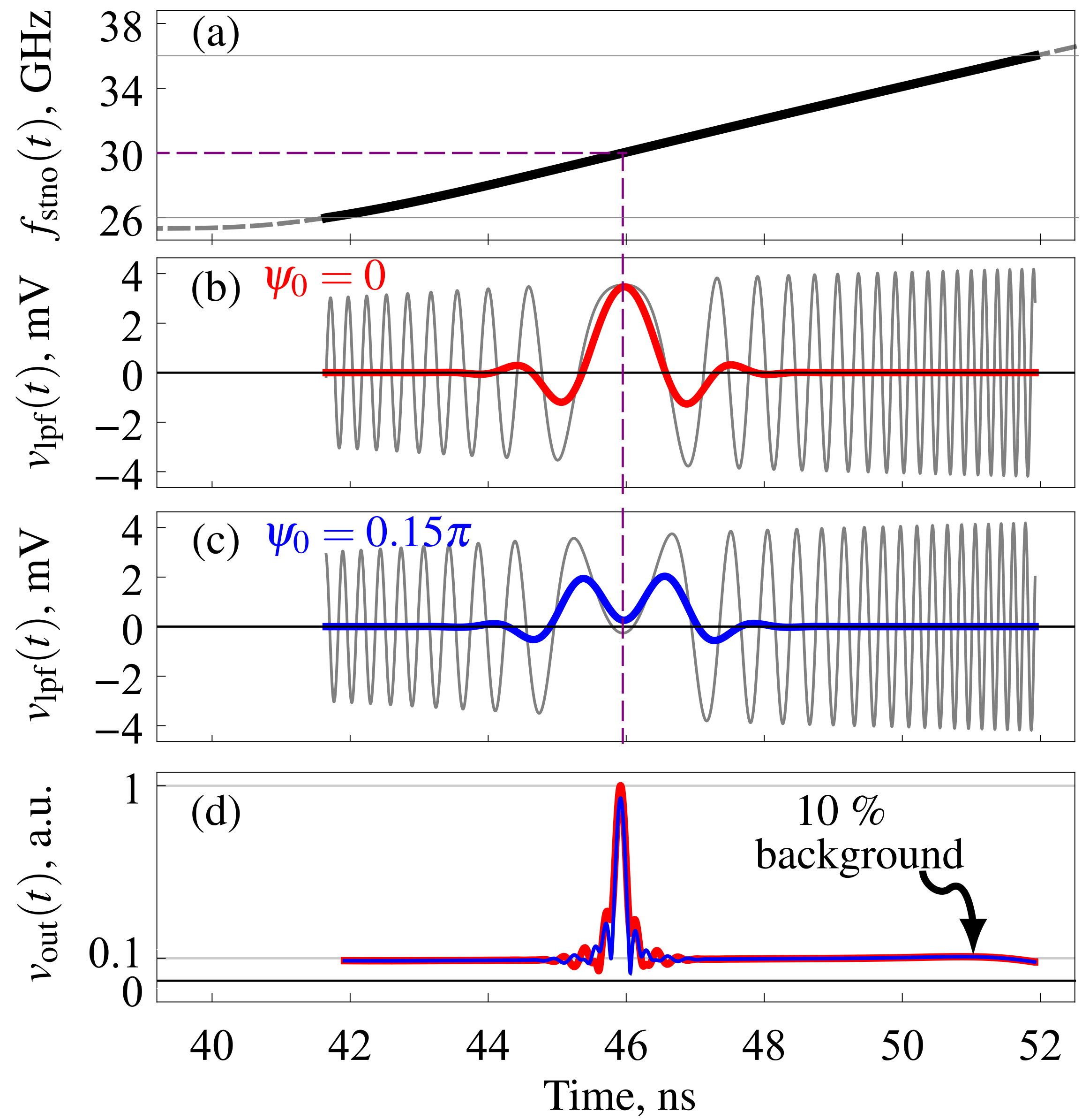

Figure 5.2: Numerical demonstration of STNO mixer spectrum analysis. (a) The frequency of STNO, $f_{\rm stno}(t)$, in response to $I_{\rm bias}(t)$. The gray dashed line shows the STNO frequency, which is constant at 25.4 GHz until 40 ns, then increases in response to a ramped DC current. The solid black line shows the STNO scanning from 26 to 36 GHz. (b) STNO output with $\psi = 0$. Grey line shows $v_{\rm lpf}$ with $f_c = 15$ GHz, and thick red line shows $v_{\rm lpf}$ with $f_c = 2$ GHz. (c) STNO output with $\psi = 0.15\pi$. (d) Matched output filter, $v_{\rm out}$, for two phases, with red for $\psi = 0$ and blue for $\psi = 0.15\pi$. Simulated with $f_{\rm c} = 4.5$ GHz and $f_{\rm m} = 32$ GHz.

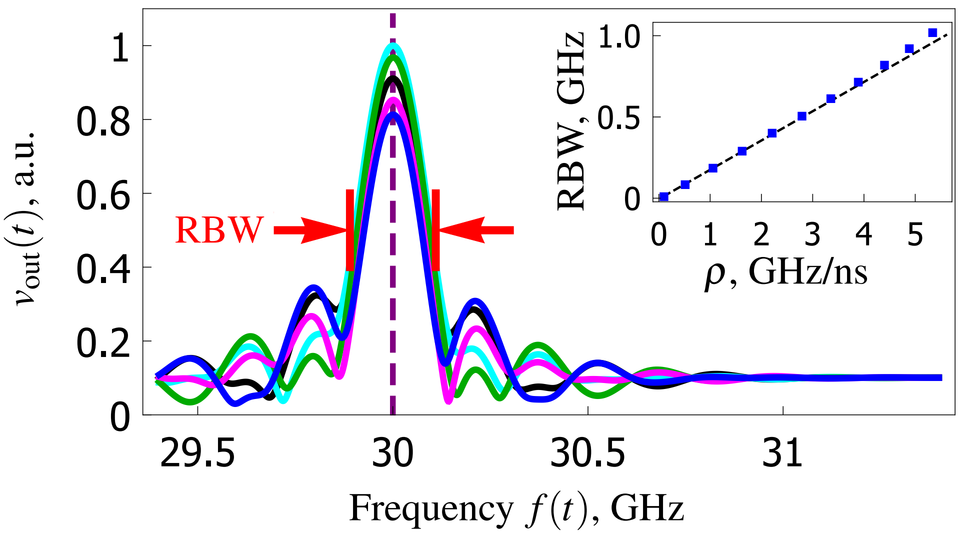

Figure 5.3: Phase invariance, external signal amplitude, and RBW for STNO mixer spectrum analyzer. Five STNO scans with $f_{\mathrm{ext}} = 30$ GHz, $\rho = 1$ GHz/ns and varied ψ. The peak, independent of ψ, occurs at 30 GHz, with RBW = 225 MHz. The peak amplitude has an uncertainty of about 8%. (inset) Comparison of RBW and ρ.

$f_{\mathrm{stno}}(t_0 \approx 46\ \mathrm{ns}) = 30$ GHz, and that both peaks are relatively independent of the phase difference ψ. Both curves also show a relatively flat background of about 10% the signal maximum, and a minor phase dependance in the neighborhood of the peak. The origin of these distortions is explained by Equation (2.18). The curves in Figure 5.2(d) represent the primary result of this chapter; they show an STNO is theoretically capable of detecting a 0.05 pW signal while scanning a 10 GHz interval at a rate of 1 GHz/ns, and that the detection is independent of any variation of the phase difference ψ.

To further demonstrate that $v_{\mathrm{out}}(t)$ is independent of ψ, the simulation above was repeated with 50 different phases, ranging from $\psi = 0$ to π with a 0.02π step. Five typical peaks are shown in Figure 5.3. The mean peak frequency for all 50 simulations was found to be 30.001 GHz. This represents a frequency accuracy of 99.9967%. This shows that regardless of the phase difference between the external signal and the STNO, the frequency can be determined with a high precision.

The RBW of this system, as simulated, is approximately equal to the 3 dB width of a peak, and is shown in Figure 5.3 is RBW $\approx$ 225 MHz. The resolution bandwidth theoretical limit was introduced in subsection 2.2.3 as $\mathrm{RBW}_0 = \rho/f_c$. The bandwidth of the low pass filter used to simulate Figure 5.2(d) and Figure 5.3 was $f_c = 4.5$ GHz, and the scan rate was $\rho = 1$ GHz/ns. Thus for this system, at this scan rate, $\mathrm{RBW}_0 = 222$ MHz, and $\mathrm{RBW}_0 \approx \mathrm{RBW}$. A comparison of the simulated and theoretical RBW for a variety of scan rates is presented in the inset of Figure 5.3, with blue squares denoting simulated RBW and the dashed black line indicating RBW_0. It is evident, that the RBW for different scan rates remains near the theoretical limit for scan rates as high as 5 GHz/ns.

The responsivity of this system depends strongly on the low pass filter and on the matched filter. Firstly, Equation (2.11) shows that the amplitude of the detection peaks depends directly on I_{ext}, the amplitude of the external signal. Additionally, there is a minor variation in peak amplitude that is dependent on ψ. For $\rho = 1$ GHz/ns, the uncertainty is about 8%. This uncertainty increases with scan rate, and decreases vastly for slow scan rates. Thus, by using an STNO as a mixer, there is a trade off between scan rate and responsivity. To detect external signals quickly, there is slight degradation in responsivity. This uncertainty can be reduced by further signal processing.

For the MDS, it should be noted that matched filters are able to extract signals from below the Johnson-Nyquist thermal noise flow. For this system as simulated, the Johnson-Nyquist thermal noise was $V_{\mathrm{JN}} \approx 200\mu$V. The gain of the system configured simulated for Figure 5.2(d) was found via simulation to be $\sim$56 dB. In contrast, using the same filters and a white noise input, the processing gain was $\sim$34 dB. It can be assumed that the processing gain was, conservatively, about 20 dB, meaning that signals can be extracted from 20 dB below the JN thermal noise floor. Thus, the MDS for this system is about 20μV, or about $P_{\text{mds}} = 40$ pW.

The next figure demonstrates the analysis of a signal having a more complicated spectrum. Figure 5.4 shows three simulations where an STNO-based spectrum analyzer operated on an external signal that had frequencies at every integer frequency from 28 GHz to 35 GHz, each with a distinct random phase ψ between 0 and 2π. The external currents used for all three simulations were identical. Figure 5.4(a) shows the response with $\rho = 1$ GHz/ns and $f_{\text{c}} = 4.5$ GHz. With these characteristics, all peaks are correctly determined despite a rising level of a background noise. Figure 5.4(b) was simulated with the same scan rate $\rho = 1$ GHz/ns and a higher cutoff frequency of $f_c = 6.4$ GHz. It is evident that the higher f_{c} value decreases RBW and the background noise level. This suggests, that as the digitization rates improve, the higher scan rates with lower RBW will be possible. The spectral quality is further improved in Figure 5.4(c), which uses a slower scan rate of $\rho = 100$ MHz$/$ns, and $f_{\text{c}} = 4.5$ GHz. It is evident, that at slower scan rates, as expected, the RBW improves, and the background noise is substantially reduced. The variation in amplitude with respect to frequency in these detected signals is expected, and is caused by the change in the angle of precession in $\mathbf{m}$, and could be easily normalized using standard methods of digital signal processing.

The above simulations were performed assuming that the STNO phase is constant in time. In a real device, STNO phase would fluctuate due to inherent STNO phase noise, which is one of the primary obstacles for STNO use in conventional applications. The proposed spectrum analyzer, however, should be resistant to STNO phase fluctuations due to the short data acquisition time $\tau \sim 10$ ns. The STNO phase noise should have only a minor effect on the performance of the spectrum analyzer if the STNO linewidth is smaller than $1/\tau \sim 100$ MHz, which has been experimentally achieved by several research groups[88, 89].

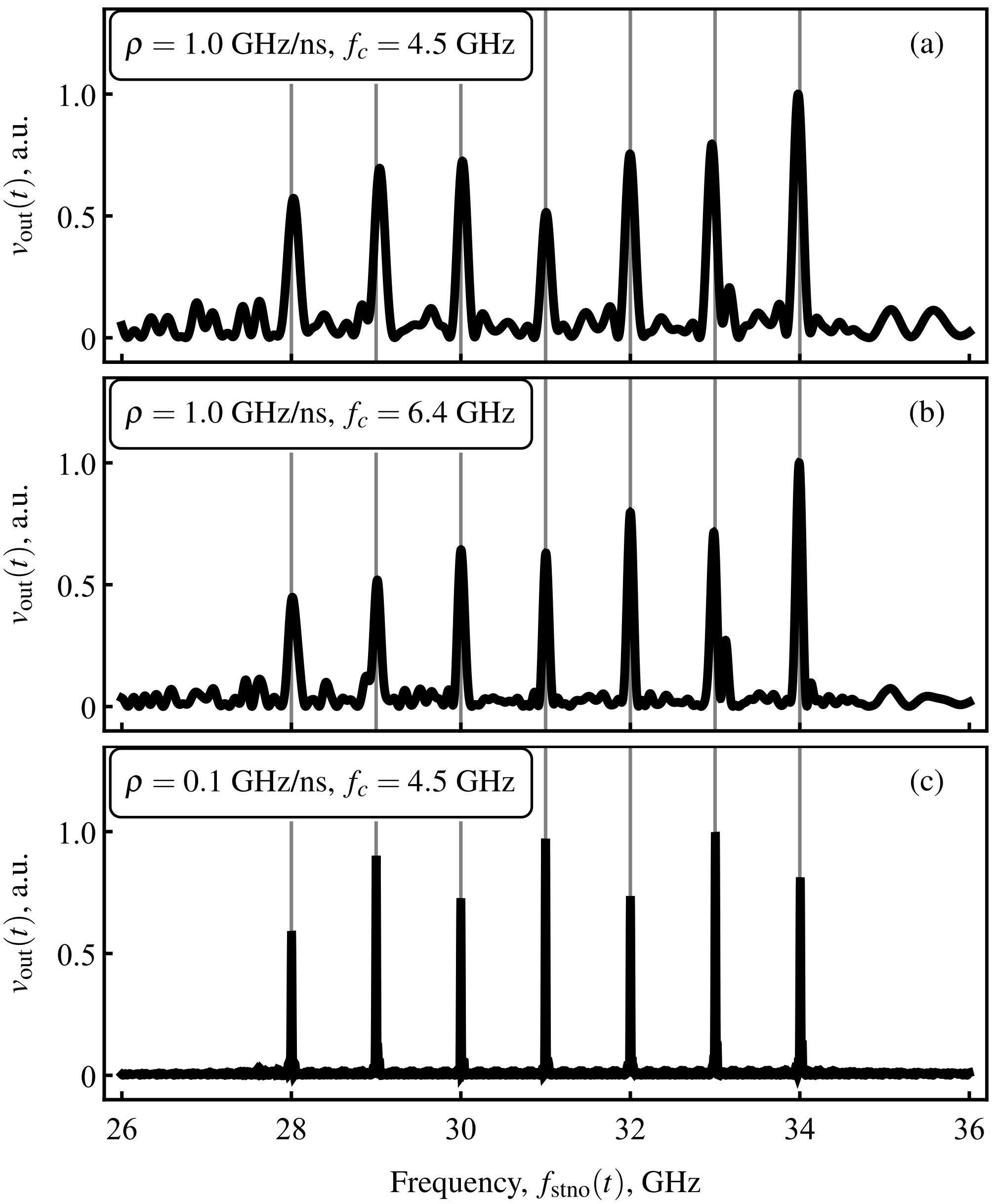

Figure 5.4: Example of STNO mixer spectrum analysis of an input signal with multiple frequencies. Spectra produced by identical 10 nA signal at every integer from 27 to 35 GHz and a random phase. Responses from the following scan parameters: (a) $\rho = 1$ GHz/ns and $f_c = 4.5$ GHz (b) $\rho = 1$ GHz/ns and $f_c = 6.4$ GHz (c) $\rho = 0.1$ GHz/ns and $f_c = 4.5$ GHz.

5.2 Experimental STNO spectrum analysis

It is demonstrated experimentally that an STNO sweep-tuned by a bias current can be used for ultra-fast spectrum analysis of frequency-manipulated microwave signals with complicated multi-tone spectra. The critical reduction in the time of spectrum analysis comes from the small intrinsic time constants of a nano-sized STNO.The demonstration is performed on a vortex-state STNO generating in a frequency range around 300 MHz, and using low-pass and matched filters for signal-processing. It is shown that a STNO-based spectrum analyzer can perform analysis of multi-tone signals, and signals with rapidly changing frequency components on a μs time scale. The proposed concept of spectrum analysis can be extended to STNOs generating in the 1-70 GHz frequency range important for radar and wireless communication applications.

5.2.1 Experimental system

The scheme of the experimental STNO-based device used to perform spectrum analysis in our experiments is shown in Figure 5.5. It consists of two blocks: the block (a) containing an STNO and used for generation of a sweep-tuned signal $v_{\text{ref}}(t)$, and the block (b) used for signal processing and eventual spectrum analysis on an external signal $v_{\text{ext}}(t)$.

The sweep-tuned reference signal $v_{\text{stno}}(t)$ is produced as follows. First, a constant dc voltage is applied to the STNO to generate an auto-oscillating signal at a constant frequency 300 MHz. Then, an additional voltage v_{sweep} having a “saw-tooth” shape with a period T is injected into the STNO via a coupler. The amplitude of the saw-tooth voltage is adjusted such that the frequency sweeps between 290 and 315 MHz, a span of $\Delta f_{\text{ch}} = 25$ MHz. After the application of a band pass filter and amplification, the signal, which is denoted $v_{\text{ref}}(t)$, has the form of a linear frequency chirp with a frequency $f_{\text{stno}}(t)$. The scan rate $\rho = \Delta f_{\text{ch}}/T$ is the parameter that is varied to characterize this system.

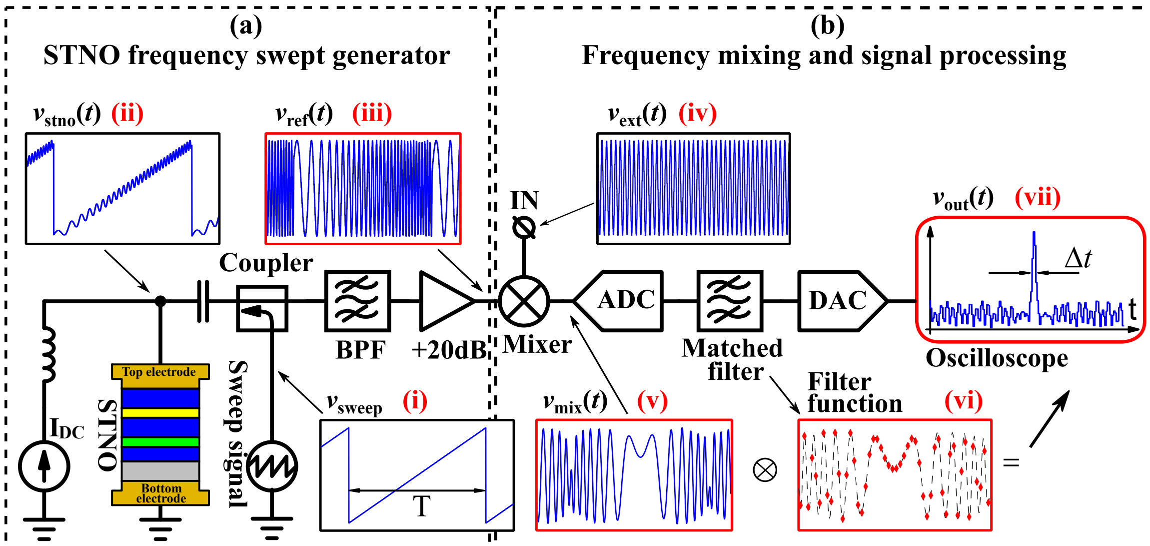

Figure 5.5: Schematic of the experimental STNO-based spectrum analyzer. Block (a) shows the generation of the swept tuned signal $v_{\mathrm{ref}}(t)$. Block (b) shows the signal processing scheme, which results in the spectrum analysis of $v_{\mathrm{ext}}(t)$. The insets show the voltage signals vs. time at different points of the device: (i) the sweep signal v_{sweep}, (ii) the raw output of the STNO $v_{\mathrm{stno}}(t)$, (iii) the reference signal $v_{\mathrm{ref}}(t)$ produced by the sweep-tuned STNO, (iv) the external signal $v_{\mathrm{ext}}(t)$, (v) the mixer output signal $v_{\mathrm{mix}}(t)$, (vi) the discretized signal obtained after the matched filter, (vii) the output pulsed signal $v_{\mathrm{out}}(t)$ containing the information about the spectrum of the external signal $v_{\mathrm{ext}}(t)$. The pulse in (vii) has a duration Δt.

The linear frequency chirp $v_{\text{ref}}(t)$ is then passed on to block (II) where it is mixed with an external signal $v_{\text{ext}}(t)$, which has a frequency f_{ext} that will be identified. The two signals are mixed using a commercially available mixer (AD831). The output of the mixer is denoted $v_{\text{mix}}(t) = v_{\text{stno}}(t)v_{\text{ext}}(t)$. This mixer has an output cutoff frequency of $f_{\text{c}} = 200$ MHz, and hence functions as a low-pass filter. It should be noted that in this experiment the sweeping frequency interval $\Delta f_{\text{ch}} = 25$ MHz is much smaller than the mixer bandwidth of $f_{\text{c}} = 200$ MHz, so that the best possible resolution bandwidth of this system is $\text{RBW}_0 = \rho/\Delta f_{\text{ch}}$.

The mixer output signal $v_{\text{mix}}(t)$ is then digitized with an 8-bit AD9280 ADC and passed through a matched filter to compress $v_{\text{mix}}(t)$ into a narrow peak whose temporal position corresponds to the frequency of the input signal f_{ext}. The matched filter output is then converted back to the analog domain with an 8-bit resolution AD9708 DAC and is visualized on a single shot oscilloscope. The matched filter was implemented with a Field Programmable Gate Array (FPGA) (Xilinx XC6SLX9)[18].

To demonstrate experimentally STNO-based spectrum analysis, a relatively low frequency ($\sim$300 MHz) vortex-state STNO was chosen as this type has a rather large output power. Results are presented for two different devices, although other devices demonstrated similar results. Figure 5.6 shows the frequency-voltage characteristics of a device under an out-of-plane field of ~ 3 kOe with a small in-plane tilt angle between 1° and 5°. This device that had a diameter of 370 nm, a parallel resistance of 40 Ω, and tunneling magnetoresistance ratio of 150%, and resistance area product of $4.5\,\Omega/\mu\text{m}^2$. As is shown in this figure, when the applied voltages is varied between 0.2 V and 0.5 V, the STNO generation frequency varies in a non-linear fashion between 280 and 315 MHz. It has a linewidth that was measured to be $\sim$0.25 MHz. This STNO was taken from a batch of STNOs that were sputter deposited then nanofabricated into nanopillars using a Singulus Rotaris machine and ion beam and optical etching techniques with the following

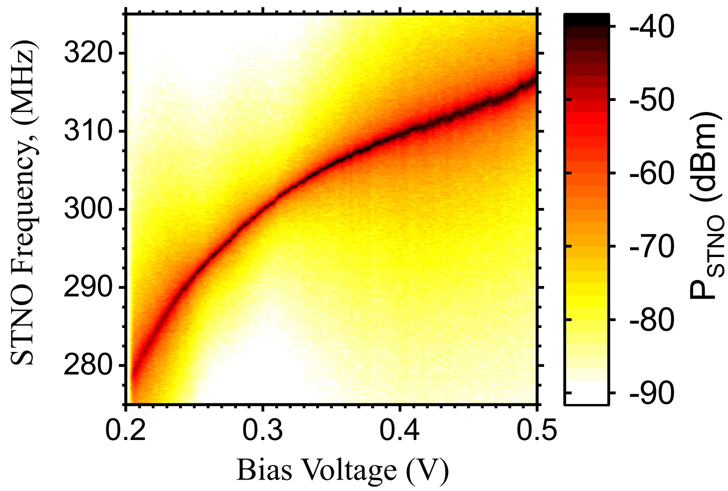

Figure 5.6: Frequency characteristic of the vortex STNO based on a magnetic tunnel junction. Free running frequency-voltage characteristic, where darker colors indicate higher power.

composition: substrate / IrMn(6) / CoFe30(2.6) / Ru(0.85) / CoFe40B20(1.8) / MgO / CoFe40B20(2.0) / Ta(0.2) / NiFe(7) / Ta (10) (thicknesses in nm).

In Figure 5.6, it is clear that the frequency generated by the STNO is a non-linear function of voltage. While this nonlinearity does not create serious difficulties in the determination of frequency of monochromatic external signals, it substantially complicates the frequency analysis of the signals with complicated multi-tone spectra. This difficulty can be eliminated by using a nonlinear (concave) profile of a “quasi-saw-tooth” voltage applied to the STNO. This makes it possible to obtain a purely linear dependence of the chirped frequency on time in the signal $v_{\mathrm{ref}}(t)$.

5.2.2 Experimental results

First, results are presented for the analysis of a monochromatic sinusoidal signal $v_{\mathrm{ext}}(t)$. This demonstrates that, by using an STNO-based spectrum analyzer, one can achieve frequency sweep rates of the order of MHz/ns with an RBW close to the

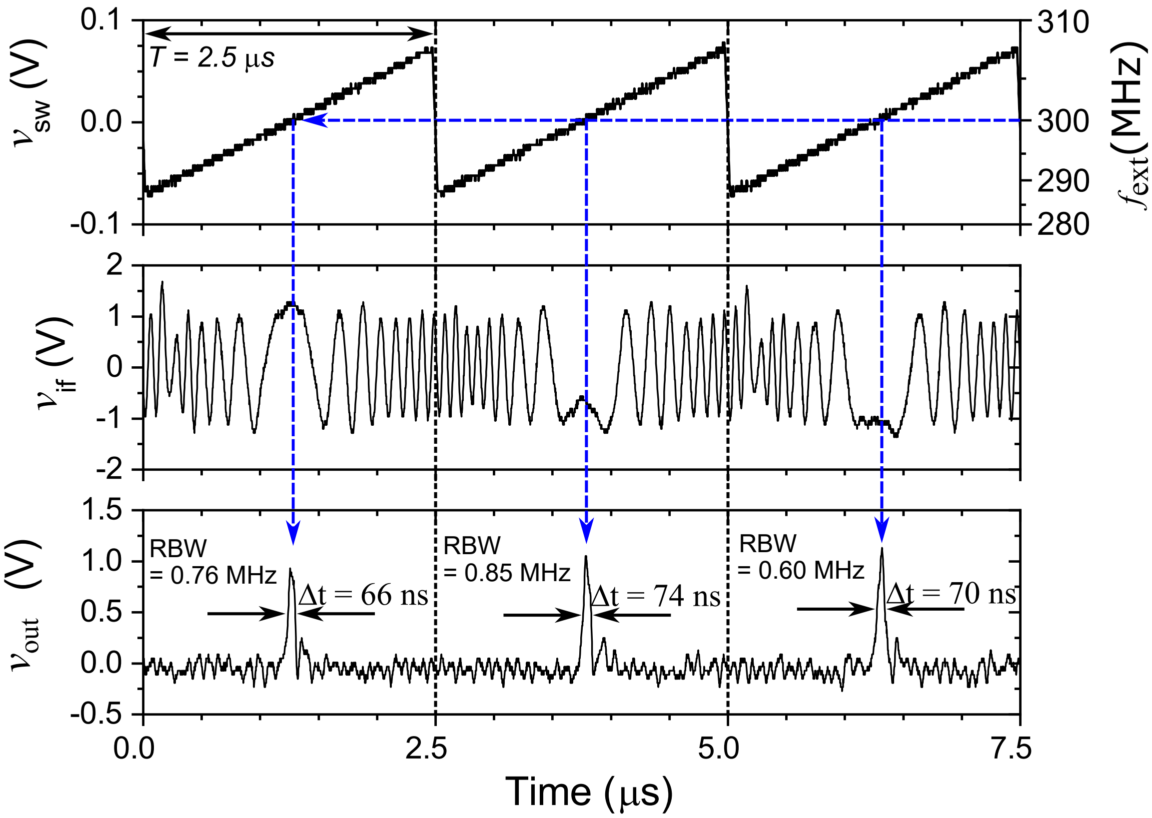

Figure 5.7: Experimental demonstration of single tone spectrum analysis. Top panel shows the $v_{\rm sweep}$ with a period of $T = 2.5\ \mu$s. This generated a frequency sweep from 285 to 305 MHz, a sweep rate of $\sim$8 kHz/ns. External signal frequency, shown on the right, was 300 MHz. Middle panel shows $v_{\rm mix}(t)$ after filtering and amplification. Bottom panel shows the output spectrum as a function of time.

theoretical limit for fast spectrum analysis. Then, it is demonstrated that an STNO-based spectrum analyzer is capable of performing the analysis of signals having complex frequency spectrum, such as two-tone signals, and signals with time-varying frequency components.

The experimental results demonstrating the analysis of a monochromatic (single-tone) sinusoidal signal used a commercial signal generator with a power of 1.0 mW and a frequency $f_{\rm ext} = 300$ MHz. Results are shown in Figure 5.7. The top panel of Figure 5.7 shows a sweeping "saw-tooth" voltage v_{sweep} with a period of 2.5 μs. The top panel also shows the instantaneous frequency of v_{stno}, varying from 285 to 305 MHz. Thus the scan rate is ~8 kHz/ns. The middle panel in Figure 5.7 shows $v_{\text{mix}}(t)$ after filtering and amplification. Note that it is a low frequency chirp waveform centered about time $t_\Delta \sim 1.5\mu$s. The bottom panel in Figure 5.7 shows the output $v_{\text{out}}(t)$ produces a peak at $t_\Delta \sim 1.5\mu$s. This maps to a frequency of 300 MHz, and thus the STNO spectrum analyzer has correctly identified the frequency of the input signal.

The RBW for scan rates of 2 kHz/ns, 16 kHz/ns, and 30 kHz/ns, aa obtained experimentally, as shown on the top Figure 5.8. The RBW for more scan rates, that vary from about 0.5 kHz/ns to 30 kHz/ns, are shown in the bottom of Figure 5.8. As the scan rate increase, the experimentally observed values also increase. The gray curve shows the theoretical best resolution bandwidth, RBW_0, as obtained in Equation (2.22). It is evident that the experimentally observed RBW is close to the theory RBW_0.

The results presented thus far have demonstrated that the basic properties of STNO-based spectrum analyzers when working with simple monochromatic external signals. Below, it will be demonstrated that STNO-based spectrum analyzers can work successfully with rather complex external signals having many different frequency components that can be varied in time. The first example is given in Figure 5.9(a) where spectrum analysis of an external signal that is a superposition of two single-tone signals. The signals are supplied from two commercial signal generators with frequencies $f_{\text{in}_1} = 300$ MHz, and $f_{\text{in}_2} = 305$ MHz. The top panel in Figure 5.9(a) shows the linear voltage sweep v_{sweep} with a black line, and dashed lines that indicate the positions where the sweeping STNO frequency equals the frequency components contained in the external signal. The bottom panel of Figure 5.9(a) shows the resultant voltage $v_{\text{out}}(t)$ with two distinct peaks, which occur at times corresponding to the frequency components f_{in_1}, and f_{in_2} from the input signal.

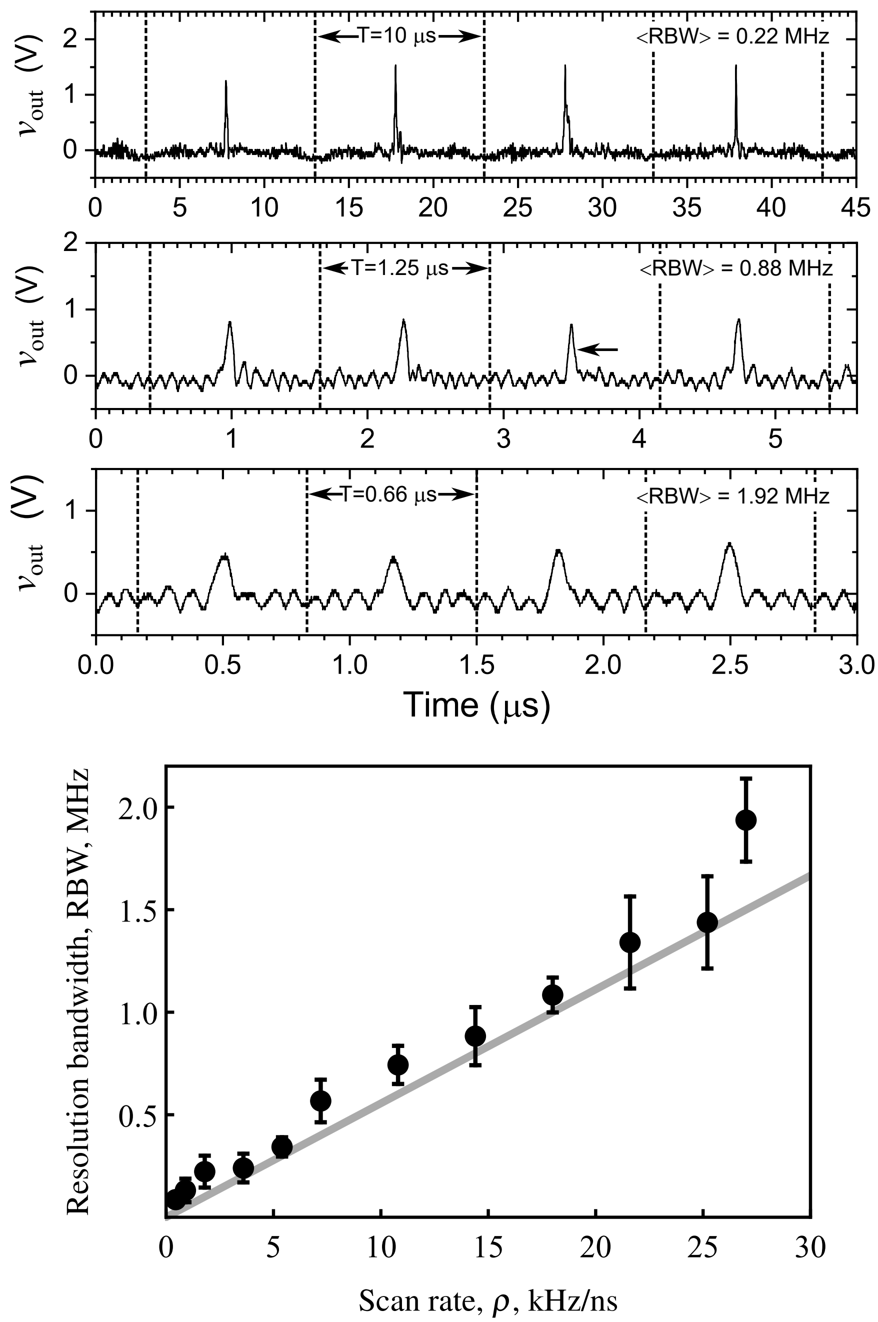

Figure 5.8: Experimental resolution bandwidth. The top graphs show <RBW>, the average RBW, for 3 scan rates, 2 kHz/ns, 16 kHz/ns, and 30 kHz/ns. Lower graphs shows experimental points in black with error bars, and gray curve shows theoretical best RBW_0.

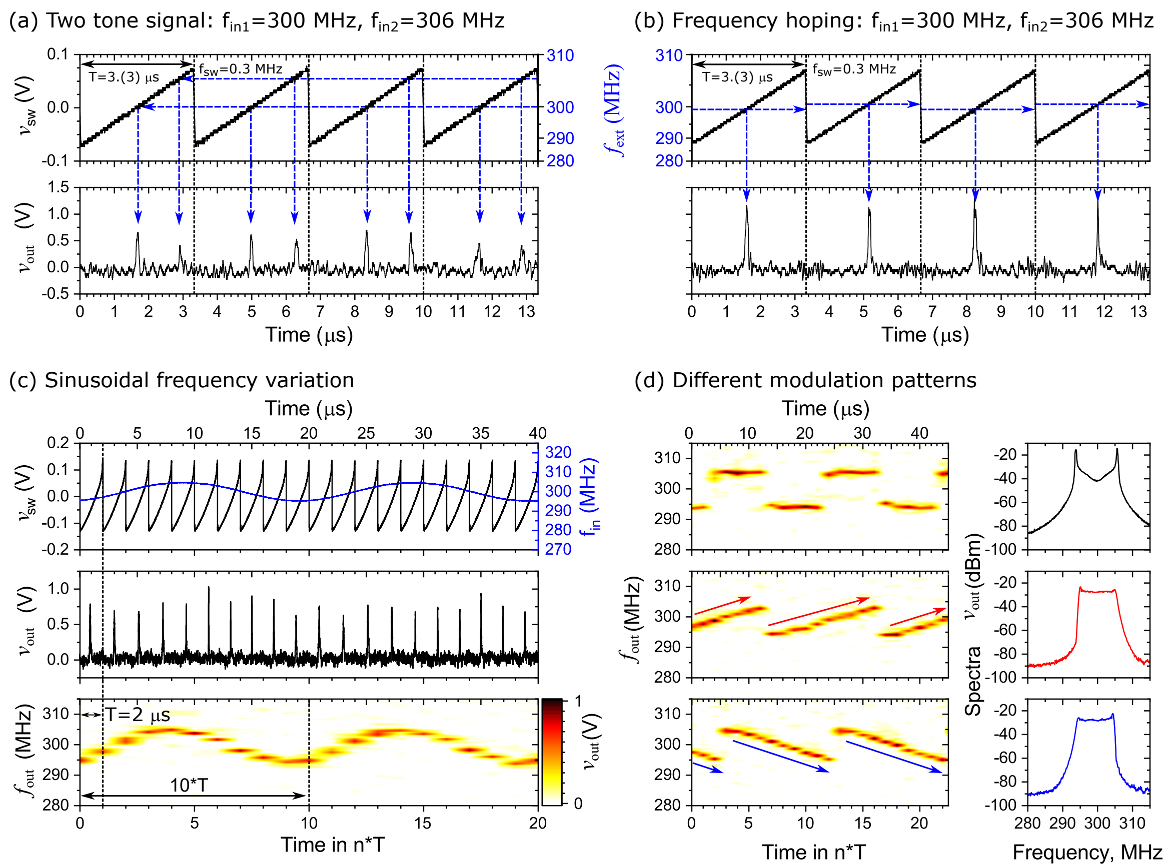

Figure 5.9: Experimental real time spectrum analysis of complex external input signals. (a) Analysis of a signal with two continuous input tones, $f_{\text{in}_1} = 300$ MHz and $f_{\text{in}_1} = 306$ MHz. Top panel shows the input frequencies and v_{sweep}, while bottom panel shows spectrum analysis results. (b) Analysis of a signal with two input tones that resemble a frequency hopping algorithm, $f_{\text{in}_1} = 300$ MHz and $f_{\text{in}_1} = 306$ MHz. Top panel shows the input frequencies changing with time and v_{sweep}, while bottom panel shows spectrum analysis results. (c) Top panel shows an input signal has a frequency that varies continuously with time while the STNO scans repeatedly with a rate of $\rho = 10$kHz/ns. Middle panel shows detection peaks, and bottom panel shows detected frequency changing with time. (d) Shows the detection of different modulation patterns. Top panel shows STNO output response to a signal modulating between two frequencies, middle and lower panel shows output response of chirp modulated signals.

Figure 5.9(b) shows the result of the frequency analysis of an external signal whose frequency hops between the values of $f_{\text{in}_1} = 300$ MHz and $f_{\text{in}_1} = 306$ MHz. This experiment demonstrates that the STNO-based spectrum analyzer can easily detect the changes of external frequency in time if these changes are happening on the time scale that is larger than the period T of the STNO frequency sweeping. This property will be important to efficiently analyze signals that employ frequency hopping protocols.

The ultimate demonstration of the potential of the STNO-based spectrum analyzer is given in Figure 5.9(c) and (d). This shows the analysis of complex external signals where the frequency that is continuously or discontinuously changing in time. Shown in the top panel by a blue line in Figure 5.9(c), the frequency of the external signal varies in time with in a sinusoidal fashion between 290 MHz and 310 MHz. The black line in the top panel Figure 5.9(c) shows v_{sweep} repeatedly driving the STNO to generate a chirped signal, with a period of 2 μs. The middle panel of Figure 5.9(c) shows the detected peak during each 2 μs period. This is replotted at a function of time in the lower panel of Figure 5.9(c). It is evident that, experimentally, this spectrum analyzer is capable of tracking continuous frequency changes with time.

Finally, the three panels of Figure 5.9(d) show a similar result of the analysis of an input signal where the frequency changes in time with discontinuities. The top panel shows the output response to a modulated signal, while the lower two panels shows the output response to inputs that were discontinuous linear chirps saw-tooth-like temporal variation that had either an increasing (top panel) or decreasing (bottom panel) frequency. It is clear, that for a spectrum analysis system based on an STNO, it is possible to easily distinguish between signals with increasing and decreasing frequencies. By contrast, the traditional power spectra of the same signals (shown in small frames to the right of the main panels) are very similar, and demonstrate only the same interval of frequency variation in both analyzed signals.

Thus, in this section it has been demonstrated experimentally that STNOs are capable of performing spectrum analysis. Indeed, it has shown that the high scanning rates of STNOs allow for high-speed spectrum analysis with a nano-scale device size.

5.3 Performance evaluation

This section will summarize the findings of this chapter by directly discussing the metrics that were introduced in section 2.1. As most of the metrics are interdependent, these metrics will be explained together. Metrics for numerical or experimental results will also be stated.

As was described at the end of chapter 4, the scanning bandwidth Δf_{ch} of this spectrum analyzer is essentially the same as the tunable bandwidth of the STNO. For the STNO as simulated here, this can be as wide as 25 GHz for systems that are tuned by a changing bias current. In practice, fabrication defects and inhomogeneities will lead to smaller scanning bandwidths, with the maximum experimentally observed tunable bandwidth approximately 10 GHz[2]. In our simulations, we assumed a scanning bandwidth of $\Delta f_{\mathrm{ch}} = 10$ GHz, although much wider bandwidths are likely possible. In the experimental demonstration that used a low frequency vortex oscillator (near 300 MHz), scanning bandwidth was $\Delta f_{\mathrm{ch}} \sim 20$ MHz.

As was described at the end of chapter 4, for the chirp to be linear, the period of the chirp T must be greater than the nonlinear transitory interval, as $T > t_{\mathrm{p}}$. There it was shown that the maximum scan rate is effectively $\rho > 2$ GHz/ns.

With this spectrum analysis system, the output voltage varied linearly with external current amplitude. Thus, the responsivity was independent of scan rate. The value of responsivity depends on the composition of the matched filter, which can be chosen arbitrarily during signal processing.

The RBW for this system was found to be near the theoretical limit prescribed by Equation (2.22). Specifically, we found both the theoretical and experimental system to be RBW $\approx \rho/\Delta f_{\text{ch}}$. This was shown in theoretically in Figure 5.3 and experimentally in Figure 5.8.

The maximum input power relies on the STNO to not injection lock to the external signal. Thus, the power of the external signal should remain below I_{lock} as was presented in Chapter 4. This means that practically, this system will have a larger maximum input for faster scan rates ρ. For a system scanning at a rate of $\rho = 1.0$ GHz/ns, this value was found on Figure 4.10(c) to be $P_{\text{max}} \sim 0.01$ mW.

The minimum detectable signal was found earlier in this chapter to be ~ 20 dB below the Johnson-Nyquist noise floor. This corresponds with an MDS of $P_{\text{mds}} \sim 40$ pW. With this MDS and maximum power, the theoretical dynamic range of an STNO spectrum analysis system based on an MTJ is ~ 100 dB.

Lastly, the frequency accuracy is determined by how close the detected frequency was to that of the actual frequency. For the system as simulated with $\rho \approx 1$ GHz/ns, the frequency accuracy was 99.9967%.

5.4 Conclusion

In summary, it has been demonstrated both theoretically and experimentally that an STNO can be used to perform fast spectrum analysis. It was demonstrated that the STNO can identify the frequency of multiple signals in superposition in the same signal, as well as analyze a frequency hopping protocol in real time. It was also shown that the resolution of this device, for fast scanning rates, operates near the theoretical limit.

CHAPTER SIX

THZ SPECTRUM ANALYSIS WITH AN ANTIFERROMATGNETIC TUNNEL JUNCTION

In this chapter, a method to perform spectrum analysis on low power signals between 0.1 and 10 THz is proposed. It proposes to use a nanoscale antiferromagnetic tunnel junction (ATJ), which was introduced in section 2.4, that produces an oscillating tunneling anisotropic magnetoresistance (TAMR) whose frequency of oscillations is dependent on the magnitude of bias spin current. Spectrum analysis can be performed by using an appropriately designed ATJ whose frequency is driven to increase linearly with time, a low pass filter, and a matched filter. This method of THz spectrum analysis, if realized in experiment, will allow miniaturized electronics to rapidly analyze low power signals with a simple algorithm. It was found by simulation and analytical theory that for an ATJ with a 0.09 μm^2 footprint, spectrum analysis can be performed over a 0.25 THz bandwidth in just 25 ns on signals that are at the Johnson-Nyquist thermal noise floor. This work was previously published in [10] and presented at [14].

To demonstrate the viability of performing spectrum analysis with an ATJ, two critical areas must be investigated. First, of the dynamic tuning of an ATJ will be investigated to ensure that it can be tuned linearly to allow application of the spectrum analysis algorithm. Second, a circuit model will be developed to describe the electrical behavior of an ATJ when interfacing with an external signal at THz frequencies. Once these two tasks have been performed, THz frequency spectrum analysis will be demonstrated.

6.1 ATJ dynamics

As covered in section 2.4, an ATJ has a TAMR that can be considered as a macroscopic oscillating resistance, which is denoted $R(t)$. An ATJ can be used for spectrum analysis because the oscillation frequency $f_{\mathrm{r}}(t)$ can be dynamically tuned in a simple manner; all that is required is a change in the magnitude of the bias current I_{drive}. In this section it will be demonstrated that the frequency of an ATJ can be dynamically tuned so that the frequency increases linearly with time. This section is analogous to section 4.1, in which the ability of an STNO to generate linear chirps was considered. A simple way to demonstrate that the ATJ is capable of being tuned with a constant scan rate ρ is to perform numerical simulations of the magnetization dynamics of the ATJ. Simulations were performed according to in the methods presented in section 3.2.

Results of the simulation for several linearly increasing bias currents are shown in Fig. 6.1. In this figure, the black dotted line shows the static relationship between I_{drive} and $f_{\mathrm{r}}(t)$. The red line shows the frequency output when the ATJ is tuned with a scan rate of $\rho_1 = 0.02$ THz/ps. It is evident that at this scan rate the ATJ tunes in a quasi-static manner, and that theoretically, an ATJ can be tuned linearly with time. This is also true for slower scan rates. At a faster scan rate of $\rho_2 = 0.5$ THz/ps, shown by a green line, there is a slight offset from quasi-static, and a slight ripple. This ripple arises due to the inertial dynamics of the AFM sublattices, and is related to the transient forced oscillations of the system. The presence of these ripples points to a physical limit for a maximum ρ where the ATJ ramps linearly with time. At even faster scan rates, $\rho_3 = 1.5$ THz/ps (blue) and $\rho_4 = 3.0$ THz/ps (magenta), the offset from linear dependence increases, as does the amplitude of the ripple. In this study, spectrum analysis will be performed at a substantially slower scan rate of $\rho = 10$ GHz/ns, in the quasi-static regime, where $f_{\mathrm{r}}(t)$ increases according to Equation (2.5).

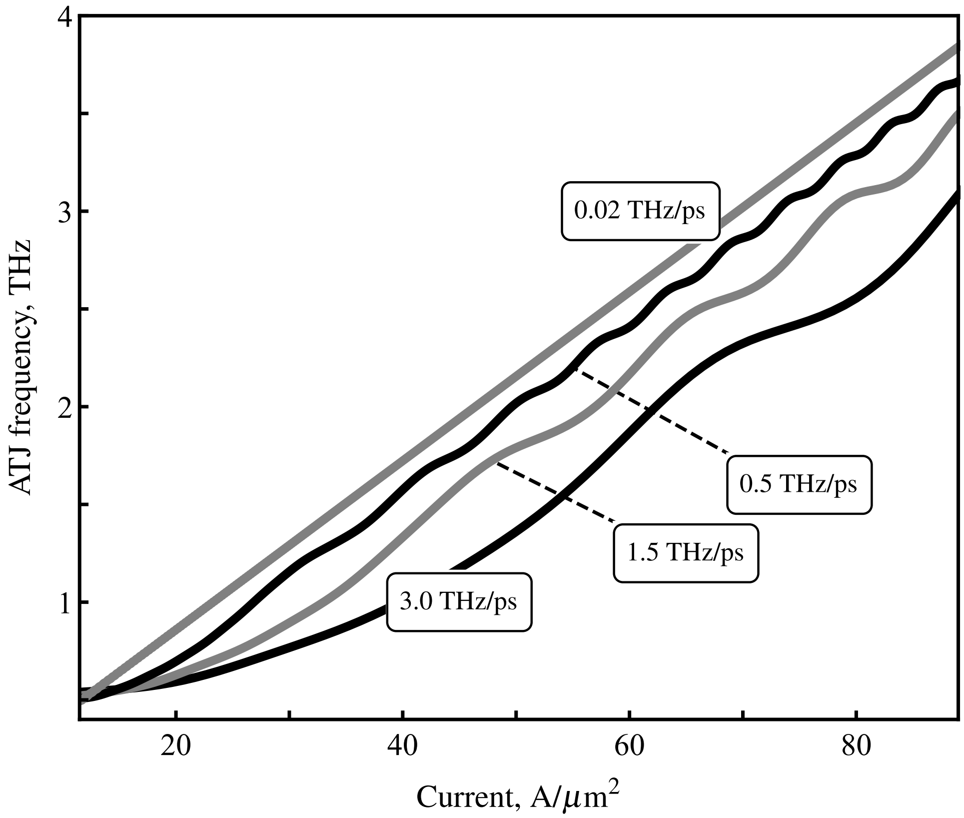

Figure 6.1: ATJ dynamic response to ramped current. For each ρ, ATJ was allows to run for 50 ps at 0.5 THz to reach normal operation. Then, the current was ramped to cause linear frequency increase at the following rates: $\rho_1 = 0.02$ THz/ps, $\rho_2 = 0.5$ THz/ps, $\rho_3 = 1.5$ THz/ps, and $\rho_4 = 3.0$ THz/ps.

It has thus been shown via numerical simulation that an ATJ is capable of being tuned in a dynamic manner at a rate that allows the frequency to increase linearly with time. This means that an ATJ can be used with any of the algorithms presented in section 2.2, thus allowing spectrum analysis to be performed in the THz gap.

6.2 Spectrum analysis algorithm

Spectrum analysis will be performed in a manner that is similar that used in chapter 5. A schematic of how THz spectrum analysis will be performed is shown in Figure 6.2. This section will briefly present the required notation for this chapter.

The ramped dc current $I_{\mathrm{drive}}(t)$ drives the ATJ TMAR $R(t)$ to oscillate according to Equation (2.30), with a THz frequency $f_{\mathrm{r}}(t)$ increases linearly with time, according to Equation (2.5). Spectrum analysis will be performed on an THz frequency current, given by

$$i_{\mathrm{R}}(t) = I_{\mathrm{R}} \cos(\omega_{\mathrm{ext}} t + \psi_{\mathrm{ext}})\,. \tag{6.1}$$

Here I_{R} is the amplitude of $i_{\mathrm{R}}(t)$.When $i_{\mathrm{R}}(t)$ passes through the ATJ, it is multiplied by $R(t)$ to produce a voltage $v_{\mathrm{atj}}(t) = i_{\mathrm{R}}(t)R(t)$. When a low pass filter with a cutoff frequency f_{c} is applied to $v_{\mathrm{atj}}(t)$, the output voltage of the filter is given by,

$$v_{\mathrm{lpf}}(t) = \tfrac{1}{2} I_{\mathrm{R}} \Delta R_{\mathrm{atj}} \cos(\theta(t, f_{\mathrm{ext}}) + \psi)\,. \tag{6.2}$$

The next step in spectrum analysis is to apply a matched filter to $v_{\mathrm{lpf}}(t)$, Details of the matched filter can be found in section 2.2.

Please note that although the signals being detected are in the THz frequency region, $v_{\mathrm{lpf}}(t)$ will have a frequency low enough allow the use of standard analog to digital converters, which allows $h_{\mathrm{match}}(t)$ to be applied in the digital domain, and will greatly simplify required signal processing.

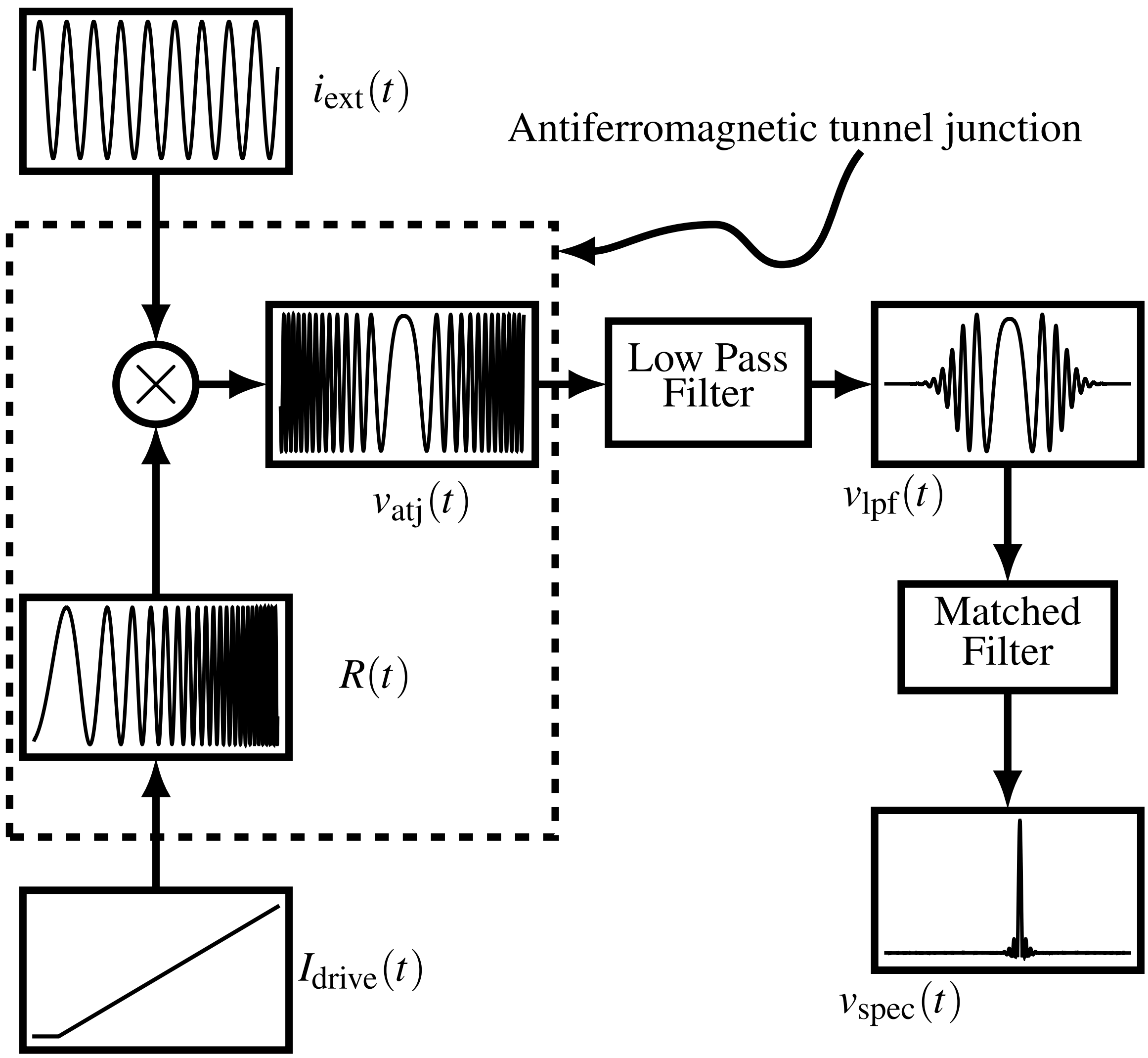

Figure 6.2: Block diagram of an ATJ spectrum analyzer. The ATJ tunneling anisotropic magnetoresistance $R(t)$, which is driven by ramped current $I_{\text{drive}}(t)$, is multiplied by external microwave current $i_{\text{ext}}(t)$ to produce voltage $v_{\text{atj}}(t)$. After passing through a low pass filter and a matched filter, a spectrum $v_{\text{out}}(t)$ is produced.

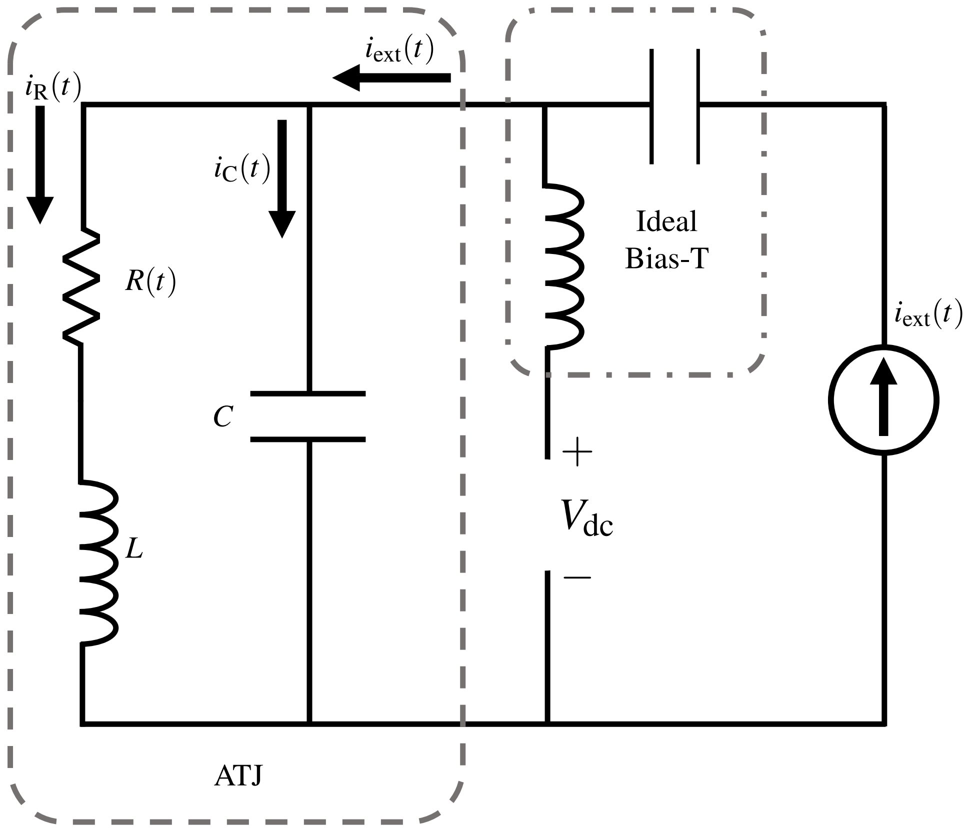

Figure 6.3: ATJ equivalent electric circuit. The region on the left enclosed by a large gray dashed rectangle is the equivalent circuit for the ATJ, with resistance $R(t)$, spurious inductance L, and spurious capacitance C. On the right is the source for the external signal to be analyzer $i_{\text{ext}}(t)$, on the top enclose by a dot-dashed rectangle is an ideal bias-T. At the center of the circuit is V_{dc}.

6.3 Electrical model of the ATJ

The previous sections described the spectrum analysis algorithm and the dynamics of the ATJ. This section will describe the impact that parasitic capacitance C and parasitic inductance L will have on $v_{\text{lpf}}(t)$. L and C must be considered in this system because at THz frequencies, matching losses cannot be eliminated by reducing fabricated circuit size. This section will present the equivalent circuit to the ATJ, characterize matching losses.

In this section, it is prudent to treat the ATJ as a detector of single frequencies; specifically, by setting $\rho = 0$, $f_0 = f_{\text{ext}}$, and $\phi = 0$. When operating with these parameters, the ATJ will oscillate with exactly the same frequency and phase as $i_{\text{R}}(t)$. With this condition, $v_{\text{lpf}}(t)$ from Equation (6.2) reduces to a dc voltage, which is stated here for clarity:

$$V_{\text{dc}} = \tfrac{1}{2} I_{\text{R}} \Delta R_{\text{atj}} \,. \tag{6.3}$$

The ATJ shown in Figure 2.14 can be modeled by the simplified equivalent electric circuit shown in Figure 6.3. This scheme consists of the three parts: (i) the equivalent circuit of an ATJ, which is bounded by a dashed gray line and characterized by the frequency-dependent impedance $Z \equiv Z(f_{\text{ext}})$; (ii) a current source with current $i_{\text{ext}}(t) = I_{\text{ext}} \cos(\omega_{\text{ext}} t)$ that represents the signal to be analyzed. This current has an amplitude I_{ext}, a frequency f_{ext}, a phase ψ_{ext}, and an impedance $Z_{\text{ext}} = R_{\text{ext}} + jX_{\text{ext}}$, and a power P_{ext}; and (iii) a bias tee, which is bounded by a dot-dashed gray line and provides coupling between the ATJ and an external circuit. Through circuit analysis, the matching loss for the external signal $i_{\text{ext}}(t)$ when interfacing with the ATJ can be analyzed[75]. For simplicity in this subsection the bias tee is considered to be an ideal coupling element, which perfectly separates low frequency and THz signals in the circuit and does not influence the device performance.

This electric scheme of the ATJ includes one circuit branch with the oscillating resistance $R(t)$ characterized by the equilibrium impedance R_{atj} and the inductance L of an ATJ having the impedance $Z_L = j\omega_{\text{ext}} L$. This is connected in parallel to the other branch with the junction capacitance C described by the impedance $Z_C = 1/j\omega_{\text{ext}} C$. The frequency dependent complex impedance of the ATJ, which is

$Z = (R_{\rm atj} + Z_L)Z_C/(R_{\rm atj} + Z_L + Z_C)$, can be written in the form:

$$Z = R + jX\,, \tag{6.4)a}$$

$$R = \mathrm{Re}\{Z\} = \frac{R_{\rm atj}}{q}\,, \tag{6.4)b}$$

$$X = \mathrm{Im}\{Z\} = \frac{\omega_{\rm ext} L(1-\xi) - R_{\rm atj}\beta}{q}\,. \tag{6.4)c}$$

Here two dimensionless parameters have been introduced: $\xi = \omega_{\rm ext}^2 LC$, which describes resonance properties of the ATJ, and $\beta = \omega_{\rm ext} R_{\rm atj} C$, which characterizes inertial properties of the ATJ, and the ansatz $q = (1-\xi)^2 + \beta^2$.

Then the complex amplitudes $\hat{i}_{\rm R}$, $\hat{i}_{\rm C}$ of ac currents $i_{\rm R}(t)$, $i_{\rm C}(t)$, respectively, in the circuit shown in Figure 6.3 are governed by Kirchhoff's laws:

$$\hat{I}_R + \hat{I}_C = I_{\rm ext}\,, \tag{6.5)a}$$

$$\hat{I}_R(R_{\rm atj} + j\omega_{\rm ext} L) = \hat{I}_C \frac{1}{j\omega_{\rm ext} C}\,. \tag{6.5)b}$$

The solution of this system of equations can be written in the form:

$$\hat{I}_R = I_{\rm ext} \frac{1}{1-\xi+j\beta}\,, \tag{6.6)a}$$

$$\hat{I}_C = I_{\rm ext} \frac{-\xi+j\beta}{1-\xi+j\beta}\,. \tag{6.6)b}$$

When the real part of Equation (6.6)a is substituted into Equation (6.3), $V_{\rm dc}$ can be rewritten as

$$V_{\rm dc} = \tfrac{1}{2}\left[\frac{1-\xi}{q} I_{\rm ext}\right] \Delta R_{\rm atj}\,. \tag{6.7}$$

The magnitude of input ac current $i_{\rm ext}(t)$ can be determined from the equation $P_{\rm ext}(1-|\Gamma|^2) = 0.5 I_{\rm ext}^2 R$, which describes the transfer of average input signal power $P_{\rm ext}$ from an external TF electrodynamic system to the ATJ, where $\Gamma = (Z - Z_{\rm ext})/(Z + Z_{\rm ext})$ is the complex reflection coefficient. The real part of the impedance $Z_{\rm ext}$ of an external circuit, $R_{\rm ext} = \mathrm{Re}\{Z_{\rm ext}\}$, usually can be considered as a constant value within a rather narrow frequency range, while the imaginary part of the impedance, $X_{\text{ext}} = \text{Im}\{Z_{\text{ext}}\}$, changes with the frequency f_{ext}, but can be controlled using impedance matching techniques [90]. For simplicity, it is assumed that $R_{\text{ext}} = \text{constant}$, $X_{\text{ext}} = 0$. In this case an expression for the output dc voltage V_{dc} can be written in the form:

$$V_{\text{dc}} = \frac{1-\xi}{q}\sqrt{\frac{2P_{\text{ext}}}{R}}\sqrt{\frac{RR_{\text{ext}}}{(R+R_{\text{ext}})^2+X^2}}\Delta R_{\text{atj}}\,. \tag{6.8}$$

V_{dc} strongly depends on the matching coefficient $(RR_{\text{ext}})/[(R+R_{\text{ext}})^2+4X^2]$ under the square root in Equation (6.8). Hence, the ATJ can have good performance only if the active junction impedance R and the active impedance R_{ext} of an external circuit are nearly equal ($R \approx R_{\text{ext}}$). Usually, the active impedance R_{ext} is considered to be a fixed parameter, defined by the properties of the external TF electrodynamic system. When there is ideal matching, $R = R_{\text{ext}}$, and the matching coefficient $(RR_{\text{ext}})/[(R+R_{\text{ext}})^2+X^2]$ is equal to $R_{\text{ext}}^2/[4R_{\text{ext}}^2+X^2]$, which gives an output dc voltage with Equation (6.4) for a perfectly matched detector:

$$V_{\text{dc}} = \frac{1-\xi}{\sqrt{q}}\sqrt{\frac{2P_{\text{ext}}}{R_{\text{atj}}}}\sqrt{\frac{R_{\text{ext}}^2}{4R_{\text{ext}}^2+X^2}}\Delta R_{\text{atj}}\,. \tag{6.9}$$

To reach the optimal condition $R \approx R_{\text{ext}}$, one can vary the cross-sectional area S of the junction and the thickness d of the MgO tunneling barrier, as will be presented in section 6.5.

6.4 Electrical parameters of the ATJ

The electrical model of the ATJ can be characterized by three intrinsic parameters: the junction equilibrium resistance R_{atj}, the inductance L and the capacitance C of the ATJ.

Using the approach introduced in [75], it was assumed that the equilibrium resistance R_{atj} depends on the thickness of the MgO barrier d, the junction cross-sectional area S, the ATJ effective resistance-area product $\text{RA}(0)$ (introduced for a "zero-thickness"

MgO barrier), and the intrinsic MgO tunneling barrier parameter κ [91, 92]. This can be written in the form:

$$R_{\text{atj}} \equiv R_{\text{atj}}(S,d) = \frac{\text{RA}(0)\exp(\kappa d)}{S}\,. \tag{6.10}$$

Note that the chosen dependence of the resistance-area product of an ATJ on the thickness d of the tunneling barrier, $\text{RA}(d) = \text{RA}(0)\exp(\kappa d)$, have the same form as that for a conventional ferromagnetic tunnel junction [91, 92].

The ac resistance variations ΔR_{atj} of an ATJ can be evaluated using the TAMR ratio η as

$$\Delta R_{\text{atj}} = \frac{\eta}{2+\eta} R_{\text{atj}}\,. \tag{6.11}$$

The TAMR ratio η can be calculated for given ΔR_{atj} as $\eta = 2\Delta R_{\text{atj}}/(R_{\text{atj}} - \Delta R_{\text{atj}})$.

The capacitance of an ATJ can be estimated as the capacitance of a square parallel-plate capacitor with a plate size $a = \sqrt{S}$ and the distance d between the plates: $C = \varepsilon\varepsilon_0 S/d$ ($\varepsilon = 9.8$ is the MgO relative permittivity [93], and ε_0 is the vacuum permittivity). The inductance of an ATJ can be evaluated as $L = \mu_0 d$, where μ_0 is the vacuum permeability.

Values for these parameters can be estimated using experimental parameters as presented in Ref [69]: equilibrium resistance $R_{\text{atj}} = 55.0$ kΩ, TAMR ratio $\eta = 1.3$. The value of the intrinsic MgO barrier parameter can be estimated as $\kappa \approx 5.8$ nm^{-1} if it is assumed that the dependence of the junction resistance R_{atj} on the tunneling barrier thickness d for an ATJ is similar to that for a ferromagnetic junction [91, 92]. Using these values, the effective resistance-area product is $\text{RA}(0) \approx 0.14\ \Omega\cdot\mu\text{m}^2$ and the magnitude of the ac resistance is $\Delta R_{\text{atj}} \approx 21.7$ kΩ. Finally, $\varepsilon = 9.8$ is a reasonable estimate for the relative permittivity of the MgO barrier [93].

For the ATJ presented in Ref [69], the junction cross-sectional area was $S = 5\ \mu\text{m}^2$, and the thickness of the MgO barrier was $d = 2.5$ nm. Using these values, one can estimate a junction capacitance of $C = \varepsilon\varepsilon_0 S/d = 170$ fF and an internal inductance of $L = \mu_0 d = 3.1$ fH for the ATJ in that experiment. As will be explained in the next section, S and d will be varied to adjust R, C, and L and thus optimize ATJ performance.

The value of the output voltage V_{max} cannot exceed the breakdown voltage $V_{\mathrm{b}} \simeq E_{\mathrm{b}} d$, where E_{b} is the breakdown electric field for the tunneling barrier. Note that $E_{\mathrm{b}} = 0.4 - 0.6$ V/nm for a MgO thin film [93].

6.5 Results and discussion for static regime

This section begins with a discussion about optimizing the ATJ for operation in the static regime, then briefly discuss the ATJ as a detector of single frequencies. The optimization of the ATJ design to allow V_{dc} to be greater than 1 mV. This will be achieved by changing parameters d and S to maximize the transfer of input signal power to the ATJ.

Using with ATJ parameters as in the previous experimental work [69] as presented in section 6.4, and an active impedance of the external circuit has a value of $R_{\mathrm{ext}} = 50\ \Omega$, which is typical for microwave and terahertz electronics, and the input signal power is $P_{\mathrm{ext}} = 1\ \mu$W, the maximum TF output will be $V_{\mathrm{dc}} \sim 10^{-4}$ mV at $f_{\mathrm{ext}} \sim 0.1$ THz. This small voltage is primarily due to the large values of the junction resistance R_{atj} and capacitance C, which causes poor impedance matching and reduction of ac power transferred to the junction.

The ATJ performance can be improved by choosing appropriate geometrical junction parameters and thus the ATJ equilibrium resistance $R_{\mathrm{atj}} \sim \exp(\kappa d)/S$, junction inductance $L \sim d$, and the junction capacitance $C \sim S/d$. In Figure 6.4, the relationship between V_{dc}, S, and d is examined in order to improve performance.

Figure 6.4(a) shows that in general, V_{dc} increases monotonically with the decrease of d, the MgO layer thickness. V_{dc} can, at certain frequencies, have a maximum value with respect to d. For example, when $f_{\mathrm{ext}} = 0.1$ THz, there is a maximum at $d \approx 0.8$ nm.

This occurs when the active junction impedance R becomes comparable to the external active impedance R_{ext}. For values of $d \lesssim 1$ nm, V_{dc} plateaus or decreases instead of increasing monotonically. This plateau or decrease is due to the increase of the impedance mismatch and junction capacitance. Taking this into account, in the following simulations we consider an ATJ having a MgO barrier thickness of $d_{\text{opt}} = 1.0$ nm, which is a common value for existing tunnel junctions and can be readily fabricated [91, 92, 93].

An additional improvement of the TF signal detector performance can be achieved by varying the junction cross sectional area S. This is considered in Figure 6.4(b). For simplicity, a square-shape junction with a single effective lateral junction size $a = \sqrt{S}$ has been assumed. As one can see, for different frequencies the value of V_{dc} is constant for lower values of lateral junction size a. At these low a values, the performance of the signal detector is hindered mainly due to the resistance mismatch effect. For higher values of a, the value of V_{dc} decreases. For high a values, the device efficiency is reduced mainly due to the influence of the large junction capacitance. At junction sizes where $R - R_{\text{ext}} \approx X$, as shown by the green line in the figure, the influence of junction capacitance and resistance mismatch have similar levels. While there is no optimal value for a, it is evident that lower values leads to improved behavior. Therefore, a junction size of $a_{\text{opt}} = 300$ nm has been chosen.

Figure 6.5 shows the output dc voltage V_{dc} calculated numerically from Equation (6.8) with new spacial dimensions of $d = d_{\text{opt}} = 1.0$ nm and $a_{\text{opt}} = 300$ nm. This graph demonstrates that with appropriate physical dimensions, the ATJ is capable of producing a strong dc voltage output with a reasonably sized input signal. This figure also demonstrates that V_{dc} in the frequency range $0.1 - 1.0$ THz from an AFM-based detector connected to a standard impedance load, can be comparable to, or may even exceed, the dc voltage extracted via an inverse spin Hall effect from the detector based on a bi-anisotropic NiO/Pt structure [71]. Also in contrast to the detector based on bi-anisotropic NiO/Pt spin

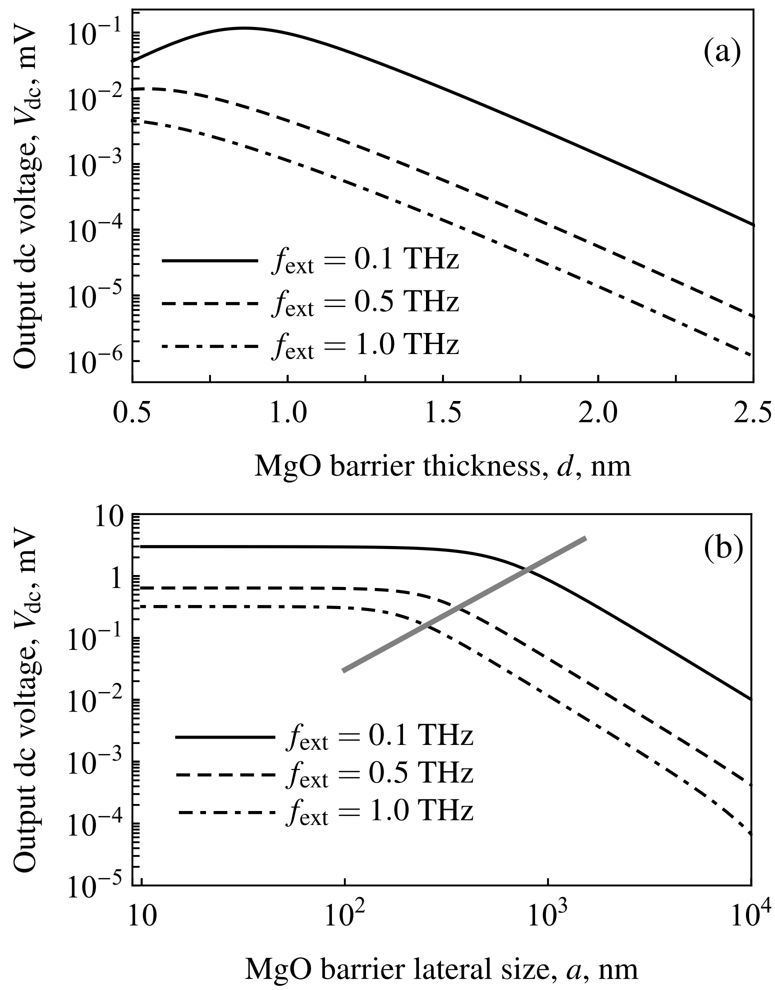

Figure 6.4: Dependence of the output dc voltage V_{dc} at input power of 1 μW on (a) MgO barrier thickness d and (b) lateral size of the ATJ square-cross-section $a = \sqrt{S}$. Calculations were performed using Equation (6.8) and Equation (6.4), Equation (6.10), Equation (6.11) for an ATJ with parameters similar to those observed in experiment (see Section 6.4 for details) operating at the frequencies $f_{ext} = 0.1$ THz (black solid line), $f_{ext} = 0.5$ THz (red dashed line), and $f_{ext} = 1.0$ THz (blue dashed dotted line). In (b), the optimal thickness of the MgO barrier $d_{opt} = 1.0$ nm was used. Green line shows curve that represents dependence of output dc voltage at deflection point for different frequencies.

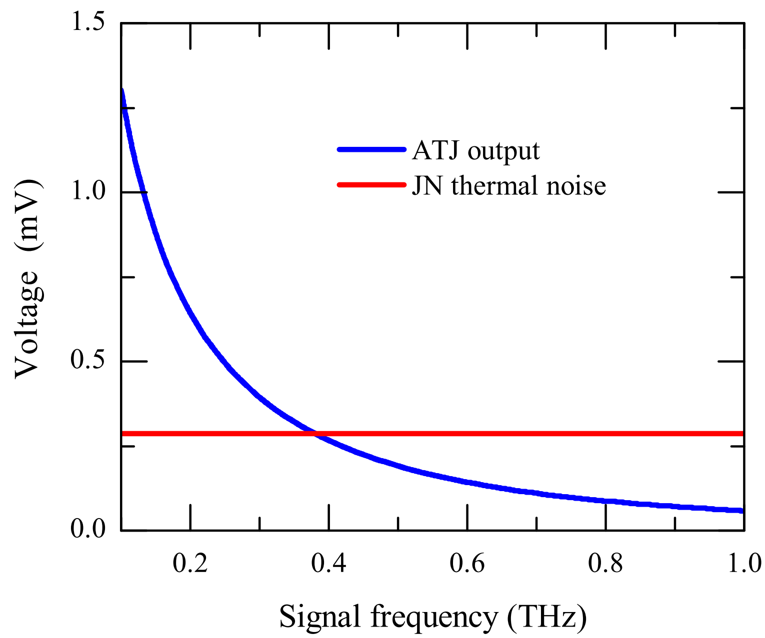

Figure 6.5: Frequency dependence of the output dc voltage V_{dc} (blue line) and the Johnson-Nyquist thermal noise floor rms voltage (red line) calculated from Equation (6.8) using typical ATJ parameters stated in section 6.4, and parameters $d = d_{\text{opt}} = 1.0$ nm and $a = 300$ nm at the temperature $T = 293$ K under input power of 1 μW.

Hall oscillator [71], the ATJ in this system does not require any special conditions for the AFM layer, therefore the experimental realization seems to be relatively straightforward.

With these new dimensions, the device parameters will be $C_{\text{opt}} = 7.81$ fF, and $L_{\text{opt}} = 1.26$ fH. It is noteworthy that for both the optimized parameters and the ATJ presented in Ref [69], that $\xi \ll 1$ for signal frequencies $f_{\text{ext}} \leq 2$ THz. This means that the nonlinear coefficient $(1-\xi)/\sqrt{q}$ in Equation (6.7) through Equation (6.9) can be approximated by

$$(1-\xi)/\sqrt{q} \approx 1/\sqrt{1+\beta^2} \approx 1/\sqrt{1+\omega_{\text{ext}}^2 R_{\text{atj}}^2 C^2}. \tag{6.12}$$

This is clearly visible in Figure 6.5.

Before concluding this section, please note that according to Equation (6.8) and Equation (6.11), the output dc voltage of the detector $V_{\mathrm{dc}} \sim \Delta R_{\mathrm{atj}} \sim \eta/(2+\eta)$ increases with the increase of the TAMR ratio η. Although here the TAMR ratio η is considered as a fixed parameter that is defined experimentally, in practice η can be tuned in several ways, for example by adding a bias dc current through the junction, adding a bias magnetic field, or by changing the operating temperature of the ATJ. However, the influence of the temperature on η and V_{dc} in an ATJ-based detector could be substantially nonlinear, similar to the behavior of conventional ferromagnetic tunnel junctions [94, 95].

It is notable that with this analysis, an ATJ operating at a single frequency can, in fact, function as a THz detector[72]. For a detector it is reasonable for $\rho = 0$ and $f_0 = f_{\mathrm{ext}}$, however, in a detection application generally the phase is unknown and thus $\phi \neq 0$. To prevent full attenuation of $v_{\mathrm{lpf}}(t)$ in cases where $\theta(f_{\mathrm{ext}}, t) + \phi \approx \frac{\pi}{2}$ in Equation (6.2), signal averaging could be used to remove the phase dependance. The general principles of operation ATF based TF detector is similar to conventional spintronic detectors [83, 96, 97] based on ferromagnetic materials. However, there are one important difference: an ATJ-based detector can detect signals with substantially larger frequencies ($f_{\mathrm{ext}} \sim 0.1 - 10$ THz) than ferromagnetic detectors.

Concluding this section, it has been shown that by changing of the thickness d and area S of the MgO layer, an ATJ can be designed to match an external signal and thus produce a strong dc voltage. Specifically, there is an optimal d to improve ATJ sensitivity, and decreasing S also improves sensitivity. It has also been shown that the nonlinear coefficient $(1-\xi)/\sqrt{q}$ causes the sensitivity to decrease with increasing frequency.

6.6 THz spectrum analysis with an ATJ

Spectrum analysis will be simulated in the bandwidth from 0.5 THz to 0.75 THz. This bandwidth, $\Delta f_{\mathrm{ch}} = 250$ GHz, will be scanned at a rate of $\rho = 10$ GHz/ns. At this

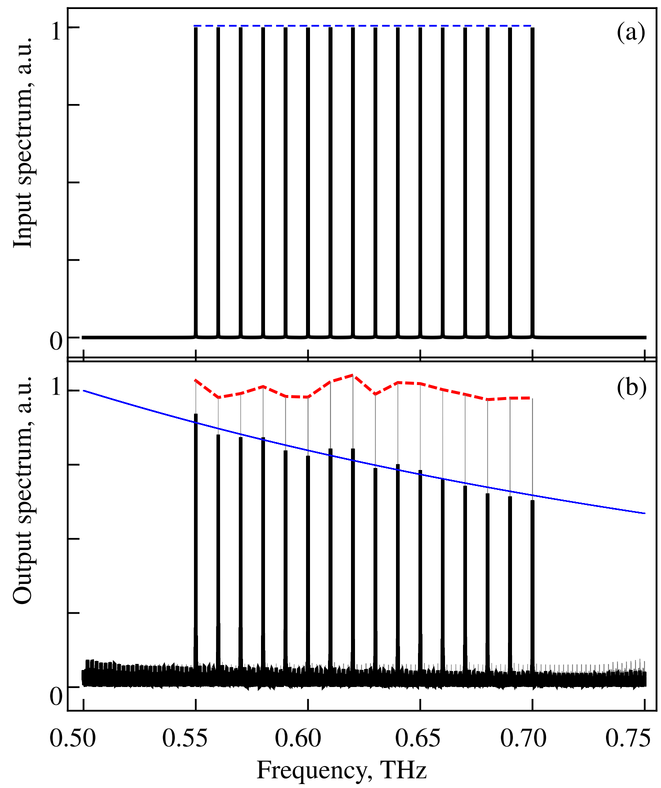

Figure 6.6: Simulation of spectrum analysis by an ATJ. (a) Input spectrum, shown by black lines, with a signal at every 10 GHz between 0.55 THz and 0.75 THz. Blue dashed line shows envelope of input spectrum. (b) Output spectrum for a scan from 0.5 to 0.75 THz, with a scan time of 25 ns. The scan rate was 250 GHz/25 ns $\approx$ 10 GHz/ns. Black curve shows U_{spec}, including parasitic impedance. Thin blue line represents (6.5). Red dashed line shows the envelope of $v_{\text{lpf}}(t)$ without parasitic impedance.

rate, the entire bandwidth can be scanned in $T = 25$ ns. The ATJ as simulated will have parameters identical to the simulation used to produce Figure 6.1, and the physical dimensions used to produce Figure 6.5. Additionally, the low pass filter was simulated with a cutoff frequency $f_c = 25$ GHz.

To demonstrate the viability of the system, the analysis of a signal with multiple frequencies will be simulated. The input current $i_{\text{ext}}(t)$ has a spectrum as shown in Figure 6.6(a), with signals every 10 GHz from 0.55 THz to 0.70 THz, each with a power of 1 μW. The envelope of input spectrum is given by the blue dashed line. It has been assumed that these signals were generated with a high-Q AFM generator, and have a low linewidth[75]. After following the algorithm presented in section 6.2, an output spectrum was produced via simulation is shown in Figure 6.6(b).

At this power level, for frequencies > 0.4 THz, the Johnson-Nyquist thermal noise floor rms voltage V_{JN} is larger than the ATJ output voltage $v_{\text{lpf}}(t)$. Specifically, with the simulation parameters, $V_{\text{JN}} = \sqrt{4k_B T R_0 f_c} = 0.09$ mV, where k_B is the Boltzmann constant and the temperature is $T = 293$ K. A magenta curve in Figure 6.5 shows V_{JN} in comparison to $v_{\text{lpf}}(t)$. Despite, the fact the thermal noise is larger than the input signal, the matched filter can produce an effective output. This improvement of the SNR is a result of the matched filter, which can make the effective minimum detectable signal (MDS) $\sim$20 dB below V_{JN}.

The black curve in Figure 6.6b shows the output spectrum $v_{\text{out}}(t)$, including the effects of parasitic impedance. It is evident that the output curve has a spike that corresponds with every input frequency. While in general the amplitude of the spikes is linear with $I_{\text{ext}}\Delta R_{\text{atj}}$, the amplitude of the $v_{\text{out}}(t)$ has an offset that depends on both frequency and phase mismatch. $v_{\text{out}}(t)$ follows the thin blue line, which decreases with frequency according to Equation (6.12), as expected. There is also a minor phase dependent variation in the amplitude of the output spectrum, as was shown in Figure 5.3.

The red dashed curve shows the envelope of $v_{\text{out}}(t)$, while ignoring the effects of parasitic impedance. This amplitude variation is expected, and can be removed by signal averaging or other means. The relative error of these amplitude variations is about 2%. The bottom portion of the black curve shows interference that is the result of incoherent mixing from the matched filter. The amplitude of this curve scales with signal power, and can limit dynamic range. Please note that both types of amplitude variations can be easily normalized, as the signal processing occurs at low frequency according to Equation (6.2) and thus can occur in the digital domain.

Concerning frequency accuracy, by using this algorithm, this simulated system was able to determine the frequency of the input spectrum with high precision and high accuracy. Specifically, the peak of each spike in Figure 6.6(b) is within 5 MHz of the input frequency, and thus has a frequency accuracy $> 99.9999\%$.

The lower end of the dynamic range is determined by the Johnson Nyquist thermal noise floor rms voltage V_{JN}, which was mentioned above. The upper end of the dynamic range for the simulated parameters is determined by the breakdown voltage V_{b} as described in section 6.4. With the dielectric MgO layer as simulated, $V_{\text{b}} \approx 0.5$ V. With this value, the total dynamic range for the ATJ is ≈ 90 dB. The dynamic range can be improved in several ways. One method is to employ a smaller cutoff frequency f_{c}, which will impact RBW. Alternatively, the thickness d of the dielectric layer can be adjusted to affect the desired change in dynamic range. Care must be taken to ensure that $v_{\text{lpf}}(t)$ remains larger than the MDS for the entirety of the scanning bandwidth Δf_{ch}. The dynamic range is independent of the scan rate ρ.

The RBW of the simulated spectrum analysis matches well with the theoretical best RBW_0. Specifically, the average full width half maximum of the individual spikes inFigure 6.6b. was $\sim$200 MHz, which is near the theoretical limit for RBW.

For the simulated parameters, the maximum ramp rate is $\rho_{\max} \approx 0.1$ THz/ps, several orders of magnitude faster than simulated here. The RBW is of course dependent on ρ according to Equation (2.22), and the frequency sensitivity is relatively unchanged with increasing ramp rate, while for phase dependent variation in the peak amplitude, the error in responsivity increases with increasing RBW.

6.7 Conclusion

In conclusion, the author has presented in this chapter the theory that a Pt/AFM/MgO/Pt ATJ can generate an oscillating TAMR with at THz frequency. It was demonstrated with simulation that these THz frequency TAMR oscillations can be dynamically tuned to increase linearly with time as at rates as fast as 0.1 THz/ps. A circuit model was presented that allowed the optimization of the ATJ output voltage by adjusting the thickness and area of the MgO layer, thus allowing impedance matching between an ATJ and an external THz signal to be improved. Then, a basic THz signal detector, and a THz spectrum analyzer was presented. The spectrum analyzer, as simulated with optimized parameters, scanned between 0.5 THz and 0.75 THz in 25 ns, with a dynamic range > 40 dB, a resolution bandwidth of 200 MHz, and determined the frequency of an extender signal with a relative error less than $10^{-4}\%$.

APPENDIX A

MATHEMATICS OF PULSE COMPRESSION

In Equation (2.16), the output spectrum generated from a matched filter spectrum analysis algorithm was presented as

$$v_{\text{out}}(t) = |v_{\text{lpf}}(t) * h_{\text{match}}(t)|^2 . \tag{A.1}$$

The goal in this appendix is to explicitly determine $v_{\text{out}}(t)$. $v_{\text{lpf}}(t)$ here is given by:

$$v_{\text{lpf}}(t) = \begin{cases} 2\cos\left(\phi(\omega_{\text{ext}}, t) + \psi\right) & -\frac{T}{2} < t < \frac{T}{2}, \\ 0 & \text{otherwise.} \end{cases} \tag{A.2}$$

and the matched filter is given by

$$h_{\text{match}}(t) = e^{-j\phi(\omega_{\text{m}}, t)} . \tag{A.3}$$

When Equation A.2 and Equation A.3 are substituted into Equation A.1, the convolution becomes

$$v_{\text{lpf}}(t) * h_{\text{match}}(t) = \frac{1}{T} \int_{-\frac{T}{2}}^{\frac{T}{2}} 2\cos\left(\phi(\omega_{\text{ext}}, \tau) + \psi\right) e^{-j\phi(\omega_{\text{m}}, t-\tau)}\, d\tau ,$$

where τ is a constant of integration. By Euler's formula, $2\cos x = e^{jx} + e^{-jx}$, this can be split into two integrals,

$$v_{\text{lpf}}(t) * h_{\text{match}}(t) = v_1(t) + v_2(t) , \tag{A.4}$$

where,

$$v_1(t) = \frac{e^{j\psi}}{T} \int_{-\frac{T}{2}}^{\frac{T}{2}} e^{j\left(\phi(\omega_{\text{ext}}, \tau) - \phi(\omega_{\text{m}}, t-\tau)\right)}\, d\tau , \tag{A.5}$$

$$v_2(t) = \frac{e^{-j\psi}}{T} \int_{-\frac{T}{2}}^{\frac{T}{2}} e^{-j\left(\phi(\omega_{\text{ext}}, \tau) + \phi(\omega_{\text{m}}, t-\tau)\right)}\, d\tau . \tag{A.6}$$

In order to find an explicit function for Equation A.4, the integrals Equation A.5 and Equation A.6 must be evaluated.

Substituting $\phi(\omega_{\text{ext}}, \tau)$ and $\phi(\omega_{\text{m}}, t-\tau)$ into Equation A.5 and simplifying yields,

$$v_1(t) = C_1 \frac{1}{T} \int_{-\frac{T}{2}}^{\frac{T}{2}} e^{j2\pi\rho(t+\zeta)\tau} \, d\tau, \tag{A.7}$$

where $\zeta = (2\omega_0 - \omega_{\text{ext}} - \omega_{\text{m}})/2\pi\rho$ and $C_1 = e^{j\left[\psi - \pi\rho t^2 - (\omega_0 - \omega_{\text{m}})t\right]}$. Integrating Equation A.7 results in a fairly simply function:

$$v_1(t) = C_1 \operatorname{sinc}\Big(\pi\Delta f_{\text{ch}}(t+\zeta)\Big), \tag{A.8}$$

where a $\operatorname{sinc}(x)$ is defined as $\sin(x)/x$.

Substituting $\phi(\omega_{\text{ext}}, \tau)$ and $\phi(\omega_{\text{m}}, t-\tau)$ into Equation A.6 and simplifying yields,

$$v_2(t) = C_2 \int_{-\frac{T}{2}}^{\frac{T}{2}} e^{-j2\pi\rho\tau^2 + j2\pi\rho(t-\chi)\tau} \, d\tau, \tag{A.9}$$

where $C_2 = (1/T)e^{-j\left[\psi + \pi\rho t^2 + (\omega_0 - \omega_{\text{m}})t\right]}$ and $\chi = (\omega_{\text{m}} - \omega_{\text{ext}})/2\pi\rho$. From [98], this reduces to

$$v_2(t) = C_2 C_3 \left[\operatorname{erfi}\Big(\sqrt{-j2\pi\rho}\,(t - \chi + \tfrac{T}{2})\Big) - \operatorname{erfi}\Big(\sqrt{-j2\pi\rho}\,(t - \chi - \tfrac{T}{2})\Big)\right], \tag{A.10}$$

where $C_3 = \frac{\sqrt{j}}{2\sqrt{2\rho}} e^{j2\pi\rho(t-\chi)^2}$. This is a fairly cumbersome equation. Fortunately, for $t < |T/2|$, can be approximated by:

$$v_2(t) \approx 2C_2 C_3 e^{-j\frac{\pi}{4}}. \tag{A.11}$$

The validity of this approximation is demonstrated graphically in Figure A.1, with Equation A.11 shown by a thick gray line, and the exact function with a thin black line. With the exception of some minor variations in the exact function, the approximation matches the exact function quite well.

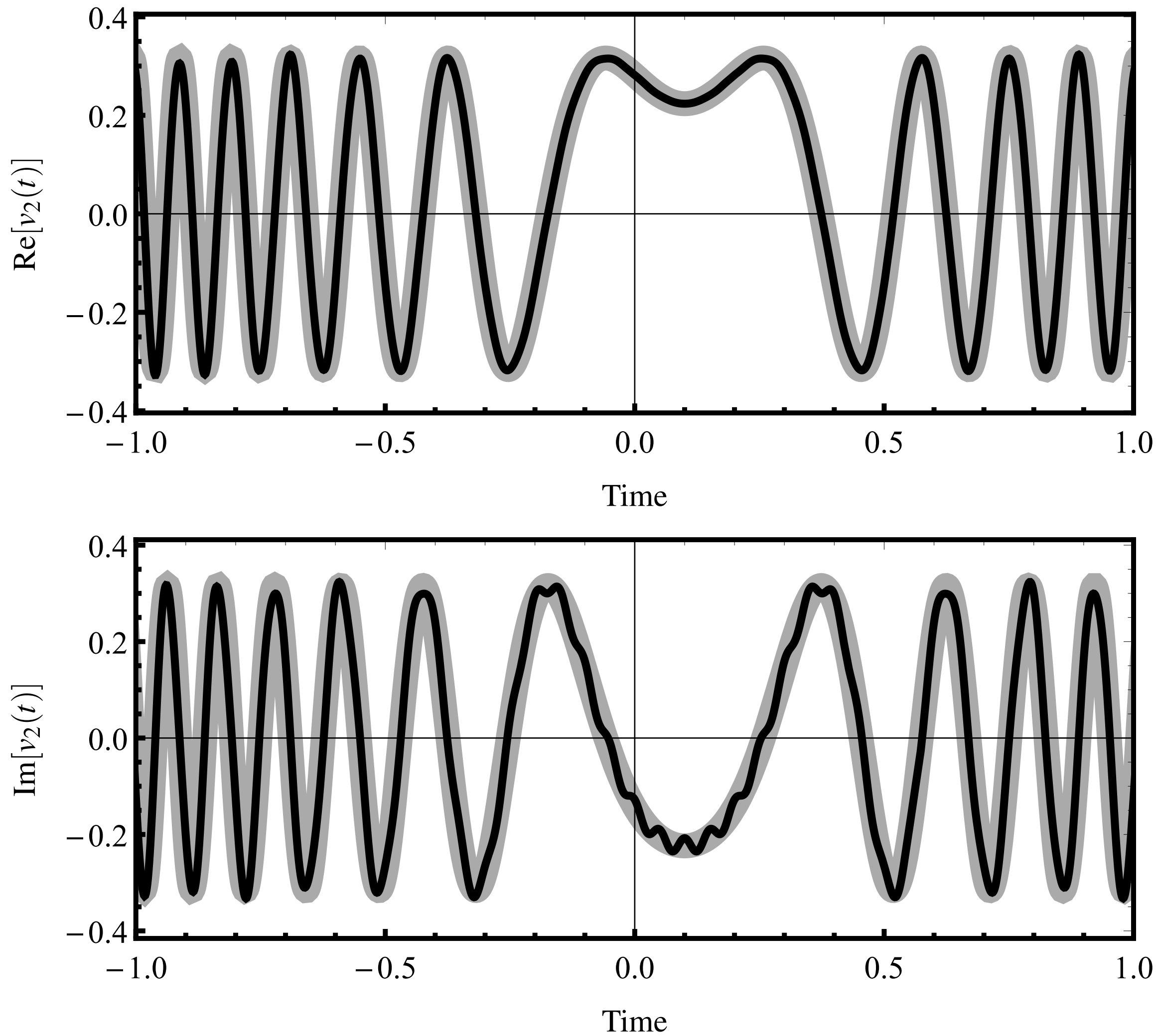

Figure A.1: Validity of the approximation $v_2(t) \approx 2C_2C_3e^{-j\frac{\pi}{4}}$. Both graphs show the approximation with a solid gray line, and the exact function with a black line. Top graph shows the real part of $v_2(t)$, and the bottom graph shows the imaginary part of $v_2(t)$.

Substituting Equation A.8 and Equation A.11 into Equation A.4 and Equation A.1 gives an equation for $v_{\text{out}}(t)$:

$$v_{\text{out}}(t) = \operatorname{sinc}^2\Big(\pi\Delta f_{\text{ch}}(t+\zeta)\Big) + \varepsilon(\psi)\frac{1}{\sqrt{2\Delta f_{\text{ch}}T}}\operatorname{sinc}\Big(\pi\Delta f_{\text{ch}}(t+\zeta)\Big) + \frac{1}{2\Delta f_{\text{ch}}T}\,,$$

where $\varepsilon(\psi) = \cos\Big(2\pi\rho(t-\chi)^2 - 2\psi - \frac{\pi}{4}\Big)$.

If ω_{m} is chosen such that $\omega_{\text{m}} = \omega_0$, then $\zeta = -t_\Delta$ and $\chi = t_\Delta$. With t_Δ and some rearrangement, these two equations can be re-written as:

$$v_{\text{out}}(t) = \operatorname{sinc}^2\Big(\pi\Delta f_{\text{ch}}(t-t_\Delta)\Big) + \varepsilon(\psi)\frac{\sqrt{\rho}}{\sqrt{2}\Delta f_{\text{ch}}}\operatorname{sinc}\Big(\pi\Delta f_{\text{ch}}(t-t_\Delta)\Big) + \frac{\rho}{2\Delta f_{\text{ch}}^2}\,, \quad \text{A.12}$$

$$\varepsilon(\psi) = \cos\Big(2\pi\rho(t+t_\Delta)^2 - 2\psi - \frac{\pi}{4}\Big)\,. \quad \text{A.13}$$

REFERENCES

[1] A. Slavin and V. Tiberkevich, "Nonlinear auto-oscillator theory of microwave generation by spin-polarized current," *IEEE Transactions on Magnetics*, vol. 45, pp. 1875–1918, Apr 2009.

[2] F. B. Mancoff, N. D. Rizzo, B. N. Engel, and S. Tehrani, "Area dependence of high-frequency spin-transfer resonance in giant magnetoresistance contacts up to 300nm diameter," *Applied Physics Letters*, vol. 88, p. 112507, Mar 2006.

[3] W. Rippard, M. Pufall, S. Kaka, S. Russek, and T. Silva, "Direct-current induced dynamics in Co90Fe10/Ni80Fe20 point contacts," *Physical Review Letters*, vol. 92, Jan 2004.

[4] S. Bonetti, P. Muduli, F. Mancoff, and J. Åkerman, "Spin torque oscillator frequency versus magnetic field angle: The prospect of operation beyond 65 GHz," *Applied Physics Letters*, vol. 94, p. 102507, Mar 2009.

[5] S. Louis, V. S. Tyberkevych, and A. Slavin, "Spin torque oscillator frequency response to dc bias current ramp," *Abstracts of the 13th Joint Magnetism and Magnetic Materials - INTERMAG Conference*, San Diego, 2016. AT-07.

[6] I. Newton, *Opticks: Or, a treatise of the reflections, refractions, inflections and colours of light. The fourth edition, corrected.* Printed for William Innys at the West End of St. Pauls, 1730.

[7] T. Bangert and E. Izquierdo, "A unifying colour model for natural visual systems." unpublished, 2016.

[8] S. Louis, O. Sulymenko, V. Tiberkevich, J. Li, D. Aloi, O. Prokopenko, I. Krivorotov, E. Bankowski, T. Meitzler, and A. Slavin, "Ultra-fast wide band spectrum analyzer based on a rapidly tuned spin-torque nano-oscillator," *Applied Physics Letters*, vol. 113, p. 112401, Sep 2018.

[9] S. Louis, V. Tyberkevych, J. Li, I. Lisenkov, R. Khymyn, E. Bankowski, T. Meitzler, I. Krivorotov, and A. Slavin, "Low power microwave signal detection with a spin-torque nano-oscillator in the active self-oscillating regime," *IEEE Transactions on Magnetics*, vol. 53, pp. 1–4, Nov 2017.

[10] P. Artemchuk, O. Sulymenko, S. Louis, J. Li, R. Khymyn, E. Bankowski, T. Meitzler, V. Tyberkevych, A. Slavin, and O. Prokopenko, "Terahertz frequency spectrum analysis with a nanoscale antiferromagnetic tunnel junction," *Journal of Applied Physics*, vol. 127, no. 6, p. 063905, 2020.

[11] S. Louis, I. Lisenkov, V. Tyberkevych, J. Li, R. Khymyn, E. Bankoski, T. Meitzler, I. Krivorotov, and A. Slavin, “Ultrafast spectrum analyzer based on the injection locking of a spin-torque nano-oscillator,” *Abstracts of the 61st Annual Conference on Magnetism and Magnetic Materials (MMM)*, New Orleans, 2016. HC-08.

[12] S. Louis, V. Tyberkevych, J. Li, E. Bankoski, T. Meitzler, I. Krivorotov, and A. Slavin, “Low power microwave signal detection with a spin-torque nano-oscillator in the active self-oscillating regime,” *Abstracts of the IEEE Magnetics Conference 2017 (INTERMAG 2017)*, Dublin, 2017. BC-05.

[13] S. Louis, V. Tyberkevych, J. Li, E. Bankoski, T. Meitzler, I. Krivorotov, and A. Slavin, “Fast spectrum analysis using a mixer based on a spin torque nano oscillator,” *Abstracts of the 62nd Annual Conference on Magnetism and Magnetic Materials (MMM)*, Pittsburg, 2017. CI-04.

[14] S. Louis, P. Artemchuk, O. Sulymenko, V. Tyberkevych, J. Li, O. Prokopenko, and A. Slavin, “THz spectrum analysis using an antiferromagnetic tunnel junction as a signal mixer,” in *APS Meeting Abstracts*, 2019.

[15] P. Artemchuk, S. Louis, O. Prokopenko, V. Tiberkevich, and A. Slavin, “Signal to noise ratio and maximum detected frequency of terahertz-frequency spectrum analyzer based on an antiferromagnetic tunnel junction.,” *Abstracts of the 64nd Annual Conference on Magnetism and Magnetic Materials (MMM)*, Las Vegas, 2019. AB-08.

[16] A. Litvinenko, P. Sethi, V. Iurchuk, S. Louis, C. Murapaka, P. Cros, V. Bortolotti, V. Tibervevich, A. Slavin, A. Jenkins, R. Ferreira, B. Dieny, and U. Ebels, “Spintronics based rf systems for wireless communication and signal processing.,” *Abstracts of the 64nd Annual Conference on Magnetism and Magnetic Materials (MMM)*, Las Vegas, 2019. AC-01.

[17] A. Litvinenko, V. Iurchuk, P. Sethi, S. Louis, V. Tibervevich, A. Jenkins, R. Ferreira, B. Dieny, A. Slavin, and U. Ebels, “Ultra-fast spectrum analysis using spin-torque nano-oscillator.,” *Abstracts of 6th Magnonics conference*, Carovigno, Italy, 2019. P23.

[18] A. Litvinenko, V. Iurchuk, P. Sethi, S. Louis, V. Tibervevich, J. Li, A. Jenkins, R. Ferreira, B. Dieny, A. Slavin, and U. Ebels, “Experimental demonstration of a rapid sweep-tuned spectrum analyzer with temporal resolution based on a spin-torque nano-oscillator,” *arXiv preprint arXiv:2004.03508*, 2020.

[19] R. Knutson, “FCC’s TV airwaves auction drew $19.8 billion, led by tmobile,” *Wallstreet Journal*, Apr 2017.

[20] I. F. Akyildiz, W. Y. Lee, M. C. Vuran, and S. Mohanty, “Next generation / dynamic spectrum access/cognitive radio wireless networks: A survey,” *Computer Networks*, vol. 50, pp. 2127–2159, Sep 2006.

[21] J. C. Haartsen, “Bluetooth radio system,” in *Wiley Encyclopedia of Telecommunications* (J. G. Proakis, ed.), vol. 1, pp. 307–317, John Wiley & Sons, 2003.

[22] R. T. Yazicigil, P. Nadeau, D. Richman, C. Juvekar, K. Vaidya, and A. P. Chandrakasan, “Ultra-fast bit-level frequency-hopping transmitter for securing low-power wireless devices,” in *2018 IEEE Radio Frequency Integrated Circuits Symposium*, pp. 176–179, IEEE, Jun 2018.

[23] A. G. Bole, A. Wall, and A. Norris, *Radar and ARPA manual: radar, AIS and target tracking for marine radar users, 3rd edition*. Butterworth-Heinemann, 2014.

[24] M. Skolnik, “Radar,” in *Reference Data for Engineers, 9th edition* (M. Van Valkenburg and W. Middleton, eds.), pp. 36–1 to 36–14, Newnes, 2001.

[25] C. Rauscher, V. Janssen, and R. Minihold, *Fundamentals of spectrum analysis, 9th edition*. Rohde & Schwarz, 2016.

[26] M. N. Sadiku and C. K. Alexander, *Fundamentals of electric circuits*. McGraw-Hill Higher Education, 2007.

[27] J. E. Chin and C. E. Cook, “The mathematics of pulse compression - a problem in systems analysis,” *Sperry Engineering Review*, vol. 12, pp. 11–16, Oct 1959.

[28] C. Cook, “Pulse compression-key to more efficient radar transmission,” *Proceedings of the IRE*, vol. 48, pp. 310–316, Mar 1960.

[29] M. Jack, P. Grant, and J. Collins, “The theory, design, and applications of surface acoustic wave fourier-transform processors,” *Proceedings of the IEEE*, vol. 68, no. 4, pp. 450–468, 1980.

[30] M. S. Rahman, *An investigation into spectral analysis using a chirp signal matched filter*. PhD thesis, University of Manchester, 1992.

[31] M. S. Rahman, “Design procedure of a modified chirp-matched filter spectrum analyzer,” *IETE Journal of Research*, vol. 44, pp. 13–26, Jan 1998.

[32] B. Szafraniec and D. Baney, “Method and system for optical spectrum analysis with matched filter detection,” U.S. Patent 6 486 958, Nov 2002.

[33] D. Gabor, “Theory of communication. Part 1: The analysis of information,” *Journal of the Institution of Electrical Engineers - Part III: Radio and Communication Engineering*, vol. 93, pp. 429–441, Nov 1946.

[34] J. Pain and P. Rankin, *Introduction to vibrations and waves*. John Wiley & Sons, 2015.

[35] J. V. Kim, *Spin-Torque Oscillators*, vol. 63, pp. 217–294. Elsevier, 2012.

[36] T. Chen, R. K. Dumas, A. Eklund, P. K. Muduli, A. Houshang, A. A. Awad, P. Durrenfeld, B. G. Malm, A. Rusu, and J. Akerman, "Spin-torque and spin-hall nano-oscillators," *Proceedings of the IEEE*, vol. 104, pp. 1919–1945, Oct 2016.

[37] R. K. Dumas, S. R. Sani, S. M. Mohseni, E. Iacocca, Y. Pogoryelov, P. K. Muduli, S. Chung, P. Dürrenfeld, and J. Åkerman, "Recent advances in nanocontact spin-torque oscillators," *IEEE Transactions on Magnetics*, vol. 50, pp. 1–7, June 2014.

[38] J. Slonczewski, "Current-driven excitation of magnetic multilayers," *Journal of Magnetism and Magnetic Materials*, vol. 159, pp. L1–L7, Jun 1996.

[39] L. Berger, "Emission of spin waves by a magnetic multilayer traversed by a current," *Physical Review B*, vol. 54, pp. 9353–9358, Oct 1996.

[40] Y. Zhou, V. Tiberkevich, G. Consolo, E. Iacocca, B. Azzerboni, A. Slavin, and J. Åkerman, "Oscillatory transient regime in the forced dynamics of a nonlinear auto oscillator," *Physical Review B*, vol. 82, Jul 2010.

[41] M. Zahedinejad, A. A. Awad, S. Muralidhar, R. Khymyn, H. Fulara, H. Mazraati, M. Dvornik, and J. Åkerman, "Two-dimensional mutual synchronization in spin hall nano-oscillator arrays," *arXiv:1812.09630*, Dec 2018.

[42] Z. Duan, A. Smith, L. Yang, B. Youngblood, J. Lindner, V. E. Demidov, S. O. Demokritov, and I. N. Krivorotov, "Nanowire spin torque oscillator driven by spin orbit torques," *Nature Communications*, vol. 5, Dec 2014.

[43] S. Tsunegi, K. Mizunuma, K. Suzuki, H. Imamura, S. Tamaru, M. Yoshimura, M. Sato, Y. Kono, H. Wado, A. Fukushima, and et al., "Spin torque diode effect of the magnetic tunnel junction with MnGa free layer," *Applied Physics Letters*, vol. 112, p. 262408, Jun 2018.

[44] A. Dussaux, B. Georges, J. Grollier, V. Cros, A. Khvalkovskiy, A. Fukushima, M. Konoto, H. Kubota, K. Yakushiji, S. Yuasa, and et al., "Large microwave generation from current-driven magnetic vortex oscillators in magnetic tunnel junctions," *Nature Communications*, vol. 1, Dec 2010.

[45] P. K. Muduli, Y. Pogoryelov, Y. Zhou, F. Mancoff, and J. Åkerman, "Spin torque oscillators and rf currents—modulation, locking, and ringing," *Integrated Ferroelectrics*, vol. 125, pp. 147–154, Jan 2011.

[46] M. Quinsat, F. Garcia-Sanchez, A. S. Jenkins, V. S. Tiberkevich, A. N. Slavin, L. D. Buda-Prejbeanu, A. Zeltser, J. A. Katine, B. Dieny, M. Cyrille, and et al., "Modulation bandwidth of spin torque oscillators under current modulation," *Applied Physics Letters*, vol. 105, p. 152401, Oct 2014.

[47] M. Manfrini, T. Devolder, J.-V. Kim, P. Crozat, N. Zerounian, C. Chappert, W. Van Roy, L. Lagae, G. Hrkac, and T. Schrefl, "Agility of vortex-based nanocontact spin torque oscillators," *Applied Physics Letters*, vol. 95, p. 192507, Nov 2009.

[48] C. Lin, S. Kang, Y. Wang, K. Lee, X. Zhu, W. Chen, X. Li, W. Hsu, Y. Kao, M. Liu, and et al., "45nm low power CMOS logic compatible embedded STT MRAM utilizing a reverse-connection 1T/1MTJ cell," in *2009 IEEE International Electron Devices Meeting (IEDM)*, pp. 1–4, IEEE, Dec 2009.

[49] Everspin Technologies Inc., "Everspin Embedded MRAM." `https://www.everspin.com/everspin-embedded-mram`. Accessed: 2019-07-21.

[50] M. Zahedinejad, H. Mazraati, H. Fulara, J. Yue, S. Jiang, A. A. Awad, and J. Åkerman, "CMOS compatible W/CoFeB/MgO spin hall nano-oscillators with wide frequency tunability," *Applied Physics Letters*, vol. 112, p. 132404, Mar 2018.

[51] F. Ren, A. Jander, P. Dhagat, and C. Nordman, "Radiation tolerance of magnetic tunnel junctions with MgO tunnel barriers," *IEEE Transactions on Nuclear Science*, vol. 59, pp. 3034–3038, Dec 2012.

[52] Z. Zeng, G. Finocchio, B. Zhang, P. K. Amiri, J. A. Katine, I. N. Krivorotov, Y. Huai, J. Langer, B. Azzerboni, K. L. Wang, and et al., "Ultralow-current-density and bias-field-free spin-transfer nano-oscillator," *Scientific Reports*, vol. 3, Dec 2013.

[53] S. Ikeda, K. Miura, H. Yamamoto, K. Mizunuma, H. D. Gan, M. Endo, S. Kanai, J. Hayakawa, F. Matsukura, and H. Ohno, "A perpendicular-anisotropy CoFeB-MgO magnetic tunnel junction," *Nature Materials*, vol. 9, pp. 721–724, Sep 2010.

[54] A. Pikovsky, M. Rosenblum, and J. Kurths, *Synchronization: a universal concept in nonlinear sciences*. Cambridge University Press, 2003.

[55] W. Rippard, M. Pufall, and A. Kos, "Time required to injection-lock spin torque nanoscale oscillators," *Applied Physics Letters*, vol. 103, p. 182403, Oct 2013.

[56] C. Sirtori, "Bridge for the terahertz gap," *Nature*, vol. 417, pp. 132–133, May 2002.

[57] R. Kleiner, "Filling the terahertz gap," *Science*, vol. 318, pp. 1254–1255, Nov 2007.

[58] M. Tonouchi, "Cutting-edge terahertz technology," *Nature Photonics*, vol. 1, pp. 97–105, Feb 2007.

[59] S. S. Dhillon, M. S. Vitiello, E. H. Linfield, A. G. Davies, M. C. Hoffmann, J. Booske, C. Paoloni, M. Gensch, P. Weightman, G. P. Williams, and et al., “The 2017 terahertz science and technology roadmap,” *Journal of Physics D: Applied Physics*, vol. 50, p. 043001, Feb 2017.

[60] A. Kirilyuk, A. V. Kimel, and T. Rasing, “Ultrafast optical manipulation of magnetic order,” *Reviews of Modern Physics*, vol. 82, pp. 2731–2784, Sep 2010.

[61] T. Kampfrath, A. Sell, G. Klatt, A. Pashkin, S. Mährlein, T. Dekorsy, M. Wolf, M. Fiebig, A. Leitenstorfer, and R. Huber, “Coherent terahertz control of antiferromagnetic spin waves,” *Nature Photonics*, vol. 5, pp. 31–34, Jan 2011.

[62] B. A. Ivanov, “Spin dynamics of antiferromagnets under action of femtosecond laser pulses (review article),” *Low Temperature Physics*, vol. 40, pp. 91–105, Feb 2014.

[63] T. Jungwirth, X. Marti, P. Wadley, and J. Wunderlich, “Antiferromagnetic spintronics,” *Nature Nanotechnology*, vol. 11, pp. 231–241, Mar 2016.

[64] V. Baltz, A. Manchon, M. Tsoi, T. Moriyama, T. Ono, and Y. Tserkovnyak, “Antiferromagnetic spintronics,” *Reviews of Modern Physics*, vol. 90, Feb 2018.

[65] H. V. Gomonay and V. M. Loktev, “Spin transfer and current-induced switching in antiferromagnets,” *Physical Review B*, vol. 81, Apr 2010.

[66] E. V. Gomonay and V. M. Loktev, “Spintronics of antiferromagnetic systems (review article),” *Low Temperature Physics*, vol. 40, pp. 17–35, Jan 2014.

[67] R. Cheng, D. Xiao, and A. Brataas, “Terahertz antiferromagnetic spin hall nano-oscillator,” *Physical Review Letters*, vol. 116, May 2016.

[68] J. Sinova, S. O. Valenzuela, J. Wunderlich, C. Back, and T. Jungwirth, “Spin hall effects,” *Reviews of Modern Physics*, vol. 87, pp. 1213–1260, Oct 2015.

[69] B. G. Park, J. Wunderlich, X. Martí, V. Holý, Y. Kurosaki, M. Yamada, H. Yamamoto, A. Nishide, J. Hayakawa, H. Takahashi, and et al., “A spin-valve-like magnetoresistance of an antiferromagnet-based tunnel junction,” *Nature Materials*, vol. 10, pp. 347–351, May 2011.

[70] P. Wadley, B. Howells, J. Železný, C. Andrews, V. Hills, R. P. Campion, V. Novák, K. Olejník, F. Maccherozzi, S. S. Dhesi, and et al., “Electrical switching of an antiferromagnet,” *Science*, vol. 351, pp. 587–590, Feb 2016.

[71] R. Khymyn, V. Tiberkevich, and A. Slavin, “Antiferromagnetic spin current rectifier,” *AIP Advances*, vol. 7, p. 055931, May 2017.

[72] P. Artemchuk, O. Sulymenko, O. Prokopenko, V. S. Tyberkevych, and A. Slavin, "Detector of terahertz-frequency signals based on an antiferromagnetic tunnel junction," *Abstracts of the 14th Joint Magnetism and Magnetic Materials - INTERMAG Conference*, Washington D.C., 2019. FC-02.

[73] O. Sulymenko, O. Prokopenko, V. Tiberkevich, A. Slavin, B. Ivanov, and R. Khymyn, "Terahertz-frequency spin hall auto-oscillator based on a canted antiferromagnet," *Physical Review Applied*, vol. 8, Dec 2017.

[74] R. Khymyn, I. Lisenkov, V. Tiberkevich, B. A. Ivanov, and A. Slavin, "Antiferromagnetic THz-frequency josephson-like oscillator driven by spin current," *Scientific Reports*, vol. 7, May 2017.

[75] O. R. Sulymenko, O. V. Prokopenko, V. S. Tyberkevych, and A. N. Slavin, "Terahertz-frequency signal source based on an antiferromagnetic tunnel junction," *IEEE Magnetics Letters*, vol. 9, pp. 1–5, 2018.

[76] R. Khymyn, I. Lisenkov, J. Voorheis, O. Sulymenko, O. Prokopenko, V. Tiberkevich, J. Akerman, and A. Slavin, "Ultra-fast artificial neuron: generation of picosecond-duration spikes in a current-driven antiferromagnetic auto-oscillator," *Scientific Reports*, vol. 8, Dec 2018.

[77] O. Sulymenko, O. Prokopenko, I. Lisenkov, J. Åkerman, V. Tyberkevych, A. N. Slavin, and R. Khymyn, "Ultra-fast logic devices using artificial "neurons" based on antiferromagnetic pulse generators," *Journal of Applied Physics*, vol. 124, p. 152115, Oct 2018.

[78] D. Kriegner, K. Výborný, K. Olejník, H. Reichlová, V. Novák, X. Marti, J. Gazquez, V. Saidl, P. Němec, V. V. Volobuev, and et al., "Multiple-stable anisotropic magnetoresistance memory in antiferromagnetic MnTe," *Nature Communications*, vol. 7, Sep 2016.

[79] Wolfram Research Inc., "Mathematica." Champaign, IL, 2019.

[80] H. Wang, C. Du, Y. Pu, R. Adur, P. Hammel, and F. Yang, "Scaling of spin hall angle in 3d, 4d, and 5d metals from $Y_3Fe_5O_{12}$ /metal spin pumping," *Physical Review Letters*, vol. 112, May 2014.

[81] R. Cheng, J. Xiao, Q. Niu, and A. Brataas, "Spin pumping and spin-transfer torques in antiferromagnets," *Physical Review Letters*, vol. 113, Jul 2014.

[82] J. Proakis, *Digital signal processing*. Upper Saddle River, N.J: Pearson Prentice Hall, 2007.

[83] A. Tulapurkar, Y. Suzuki, A. Fukushima, H. Kubota, H. Maehara, K. Tsunekawa, D. Djayaprawira, N. Watanabe, and S. Yuasa, "Spin-torque diode effect in magnetic tunnel junctions," *Nature*, vol. 438, no. 7066, pp. 339–342, 2005.

[84] W. Rippard, M. Pufall, and A. Kos, “Time required to injection-lock spin torque nanoscale oscillators,” *Applied Physics Letters*, vol. 103, no. 18, p. 182403, 2013.

[85] Y. Zhou, J. Persson, and J. Åkerman, “Intrinsic phase shift between a spin torque oscillator and an alternating current,” *Journal of Applied Physics*, vol. 101, no. 9, p. 09A510, 2007.

[86] Y. Zhou, J. Persson, S. Bonetti, and J. Åkerman, “Tunable intrinsic phase of a spin torque oscillator,” *Applied Physics Letters*, vol. 92, no. 9, p. 092505, 2008.

[87] V. Demidov, H. Ulrichs, S. Gurevich, S. Demokritov, V. Tiberkevich, A. Slavin, A. Zholud, and S. Urazhdin, “Synchronization of spin hall nano-oscillators to external microwave signals,” *Nature Communications*, vol. 5, 2014.

[88] T. Devolder, L. Bianchini, J. Kim, P. Crozat, C. Chappert, S. Cornelissen, M. Op de Beeck, and L. Lagae, “Auto-oscillation and narrow spectral lines in spin-torque oscillators based on MgO magnetic tunnel junctions,” *Journal of Applied Physics*, vol. 106, no. 10, p. 103921, 2009.

[89] P. Villard, U. Ebels, D. Houssameddine, J. Katine, D. Mauri, B. Delaet, P. Vincent, M. Cyrille, B. Viala, J. Michel, *et al.*, “A GHz spintronic-based RF oscillator,” *IEEE Journal of solid-state circuits*, vol. 45, no. 1, pp. 214–223, 2010.

[90] D. M. Pozar, *Microwave engineering*. J. Wiley, 3rd ed ed., 2005.

[91] J. Hayakawa, S. Ikeda, F. Matsukura, H. Takahashi, and H. Ohno, “Dependence of giant tunnel magnetoresistance of sputtered CoFeB/MgO/CoFeB magnetic tunnel junctions on MgO barrier thickness and annealing temperature,” *Japanese Journal of Applied Physics*, vol. 44, pp. L587–L589, Apr 2005.

[92] S. Yuasa and D. D. Djayaprawira, “Giant tunnel magnetoresistance in magnetic tunnel junctions with a crystalline MgO(0 0 1) barrier,” *Journal of Physics D: Applied Physics*, vol. 40, pp. R337–R354, Nov 2007.

[93] A. M. E. Raj, M. Jayachandran, and C. Sanjeeviraja, “Fabrication techniques and material properties of dielectric MgO thin films - a status review,” *CIRP Journal of Manufacturing Science and Technology*, vol. 2, pp. 92–113, Jan 2010.

[94] C. H. Shang, J. Nowak, R. Jansen, and J. S. Moodera, “Temperature dependence of magnetoresistance and surface magnetization in ferromagnetic tunnel junctions,” *Physical Review B*, vol. 58, pp. R2917–R2920, Aug 1998.

[95] O. V. Prokopenko, E. Bankowski, T. Meitzler, V. S. Tiberkevich, and A. N. Slavin, “Influence of temperature on the performance of a spin-torque microwave detector,” *IEEE Transactions on Magnetics*, vol. 48, pp. 3807–3810, Nov 2012.

[96] O. V. Prokopenko, I. N. Krivorotov, T. J. Meitzler, E. Bankowski, V. S. Tiberkevich, and A. N. Slavin, *Spin-Torque Microwave Detectors*, vol. 125, pp. 143–161. Springer Berlin Heidelberg, 2013.

[97] O. V. Prokopenko and A. N. Slavin, "Microwave detectors based on the spin-torque diode effect," *Low Temperature Physics*, vol. 41, pp. 353–360, May 2015.

[98] A. Jeffrey and D. Zwillinger, *Table of integrals, series, and products, 7th ed.* Elsevier, 2007. Equation 2.325.13.